Ancient TL

www.ancienttl.org · ISSN: 2693-0935

Issue 39(2) - December 2021
https://doi.org/10.26034/la.atl.v39.i2

ISSN 2693-0935

Ancient TL

A periodical devoted to Luminescence and ESR dating

Department of Physics, East Carolina University, 1000 East 5th Street, Greenville, NC 27858, USA
http://ancienttl.org

December 2021, Volume 39 No.2

Ancient TL

Started by the late David Zimmerman in 1977

Ancient TL

Constraining heterogeneity in the absorbed dose of 50 keV X-ray irradiated samples for EPR dating: simulation and experimental approaches

Lily Bossin[1,2*] and Georgina King[1]

[1] Institute of Earth Surface Dynamics, University of Lausanne, Switzerland
[2] Current address: Department of Radiation Safety and Security, Paul Scherrer Institute, Villigen, Switzerland

*Corresponding Author: lily.bossin@psi.ch

Received: December 18, 2020; in final form: November 19, 2021

Abstract

X-band Electron Paramagnetic Resonance (EPR) of quartz requires the irradiation of samples with volumes of ca 3 mm^3, which can be conveniently achieved using commercially available instruments such as the 50 keV X-ray Dose manufactured by Freiberg Instruments. However, X-rays at such low energies can result in highly heterogeneous absorbed doses. In this contribution we use Monte-Carlo particle transport simulations (MCNP6) to characterise the heterogeneity of the radiation field in a 3 mm inner-diameter EPR sample tube irradiated using a 50 kV X-ray generator. From these simulations, we demonstrate that the use of an aluminium filter (200 µm) is redundant when irradiating samples in glass tubes (500 µm wall thickness). Simulations of grain-by-grain absorbed doses across the tubes indicate a maximum of 20 % axial heterogeneity for grains at the tube centre, even when the sample is rotated throughout irradiation. Single-grain luminescence dosimetry measurements were used to experimentally validate the heterogeneity predicted, confirming the modelling results. EPR dosimetry calibration of the X-ray source yielded a dose rate of 0.206 ± 0.005 Gy·s^{-1}.

Keywords: EPR, X-ray source, Calibration, Monte-Carlo simulations

1. Introduction

Continuous-Wave Electron Paramagnetic Resonance (CW-EPR) X-band measurements of granular quartz require the irradiation of significant masses of material (ca 60 mg). X-ray sources can be used for this purpose. X-ray sources are relatively inexpensive and raise fewer safety concerns compared with radionuclide sources. It is thus practical to have them within an individual EPR laboratory. In contrast, gamma sources are generally restricted to specialised institutions requiring samples to be transported for irradiation and precluding single-aliquot investigations (e.g. Tsukamoto et al. 2015). X-ray sources have already been used to reconstruct the geological dose of natural minerals using luminescence techniques (Andersen et al. 2003; Thomsen et al. 2006; Kook et al. 2011; Richter et al. 2016) and more recently have been proposed for the irradiation of samples for EPR dating of natural quartz (Oppermann & Tsukamoto, 2015). Studies have also highlighted the advantages of using X-ray sources for luminescence dating; earlier work from Andersen et al. (2003) has shown that the Varian VF-50J X-ray tube (V_{max} = 50 keV) could be used for luminescence dating of quartz with satisfactory linearity between dose rate and current, meaning that dose rate adjustment could easily be achieved by varying the current. The authors also found that the X-ray tube exhibited good stability over time, yielding little variation in dose-rate throughout irradiation or with usage time, and yielded good dose recovery results. This was later confirmed by Thomsen et al. (2006) and Richter et al. (2016).

However, two major challenges affect the routine use of low energy (< 100 keV) X-ray sources for trapped-charge dosimetry: 1) variability in absorbed dose between minerals of the same type, but with different origins for identical irradiation time, operating voltage and current (Thomsen et al., 2006), 2) dependency of the absorbed dose-rate on the sam-

ple's thickness, due to strong absorption and 3) heterogeneity in absorbed dose for bulky samples such as those used in EPR dating. The first challenge was identified for natural quartz and was attributed to micro-dosimetric effects. Although quartz is one of the purest minerals on earth, a number of defects and impurities occur in natural quartz minerals (Götze & Lewis, 1994). The concentration and nature of these defects is highly variable between different quartz samples, which is reflected in the variability of their respective EPR and luminescence responses (Beerten & Stesmans 2007; Duller et al. 2000). Thomsen et al. (2006) showed that X-ray dose-rate heterogeneity for grains of quartz deposited on stainless steel discs could be reduced by using a 200 µm aluminium filter to harden the X-ray spectrum (shifting the mean emission from ~ 10 keV to ~ 15 keV; Richter et al. 2016). Richter et al. (2016) showed that hardening the beam led to an increase in the penetration depth, thus ensuring a homogeneous irradiation of the grains, although consequently the total dose-rate was reduced.

This study addresses the second challenge, that the dose to bulky samples can be highly heterogeneous. Previous work has shown that irradiation using a 50 keV Varian VF-50J X-ray tube can be used to irradiate samples within their measurement tube, thus paving the way towards single-aliquot regenerative dose protocols for EPR dating (Tsukamoto et al., 2015). Oppermann & Tsukamoto (2015) measured a radial heterogeneity of 3.1 % for samples 1.5 cm high using GaF chromic films. By comparing the dose assessed using GaF chromic films with and without a sample tube, they also predicted an axial reduction in dose to quartz of 35 % at the centre of 3 mm diameter tubes. Oppermann & Tsukamoto (2015) finally reported a reproducibility within 20 % for their setup, using X-ray irradiated alanine dosimeters.

To complement these studies and to calibrate the X-ray source recently installed at the University of Lausanne we employed radiation-transport simulations (MCNP6) to calculate the absorbed dose to grains of quartz irradiated in EPR sample tubes using a Varian VF-50J X-ray source (Tungsten target, operated at 50 keV). Radiation-transport codes such as MCNP or GEANT have already been used to characterise the artificial-laboratory-induced dose delivered to samples in instruments designed for trapped charge dating. This is because a simulation approach allows dose deposition to be investigated at a scale not achievable by experimental means. This includes, for example, the dose-depth profiles in sliced samples (Bailiff, 2018) or the evaluation of the backscatter component of samples of various shapes irradiated in a luminescence reader (Autzen et al. 2017).

In the first part of this paper, a simulation-based approach is used to determine the deposition energy spectrum for different filtering conditions to evaluate whether the spectrum needs to be filtered with, for example, an aluminium filter. Dose attenuation through the tube is then simulated at a single-grain level, a level of precision not achievable using experimental procedures. These simulations serve as the basis for the X-ray generator calibration, allowing more accurate error estimation and a better understanding of how dose is distributed within a sample tube. In the second part of this paper, optically stimulated luminescence (OSL) single-grain measurements of quartz grains irradiated with the X-ray source are used to experimentally assess absorbed dose heterogeneity and to either falsify or verify the MCNP results. Finally, EPR dosimetry of granular quartz is used to calibrate the source for quartz grains in the grain size fraction 180 – 212 µm.

2. Materials and Methods

2.1. Description of the X-ray source and irradiation geometry

The X-ray apparatus "X-ray dose" manufactured by Freiberg Instruments (Figure 1) comprises a Varian VF-50J X-ray source (tungsten target, Beryllium window 76 µm) coupled to a Spellman power supply operating at a maximum voltage V_{max} = 50 keV, and maximum current I_{max} = 1 mA. A rotating sample tube holder is incorporated to provide better homogeneity during sample irradiation. The sample tube is placed 40 mm from the end of the X-ray tube during irradiation and the beam is collimated to provide a restricted irradiation window. A 9 mm thick brass shutter (maximum shutter time 300 ms) controls the beginning and end of the irradiation and allows irradiation to start only when the tube has warmed up and reached the desired voltage and current. Documentation on the instrumentation is available from the manufacturer ("X-ray dose manual", available on demand from Freiberg Instruments). The samples are irradiated in glass sample tubes (Wilmad Suprasil) of 3 mm external diameter and 2 mm internal diameter (glass thickness: 500 µm).

2.2. Radiation-transport simulations

A simplified model of the irradiation geometry was built in MCNP6.2 (Goorley et al., 2012), comprising a plan parallel source with an emission energy spectrum taken from Richter et al. (2016). This spectrum mimics the emission spectrum for the unfiltered X-ray source operating at a voltage of 50 keV. The beam was not collimated in these simulations, as the exact geometry of the collimator was not known.

The grains of quartz were modelled as 200 µm diameter SiO_2 spheres of density g = 2.63 g·cm^{-3}. The glass tube (SiO_2, density g = 2.2 g·cm^{-3}) was filled with these grains using an MCNP repeated structure following a cubic lattice and placed 40 mm from the plan parallel source (Figure 2). The geometry was simulated in air.

The Monte Carlo N-Particle Transport version 6 (MCNP6, Goorley et al. 2012; Pelowitz 2013) code developed by Los Alamos National Laboratory was used to simulate the transport and interactions of particles using repeated random processes. The behaviour of each particle is simulated and recorded in specific volumes (cells). Results are reported using "tallies" that count the number of specified events (e.g., track length, collision, surface crossing) in a given cell. MCNP can calculate the absorbed dose in a cell using the energy deposition tally (F6 tally) or the pulse height

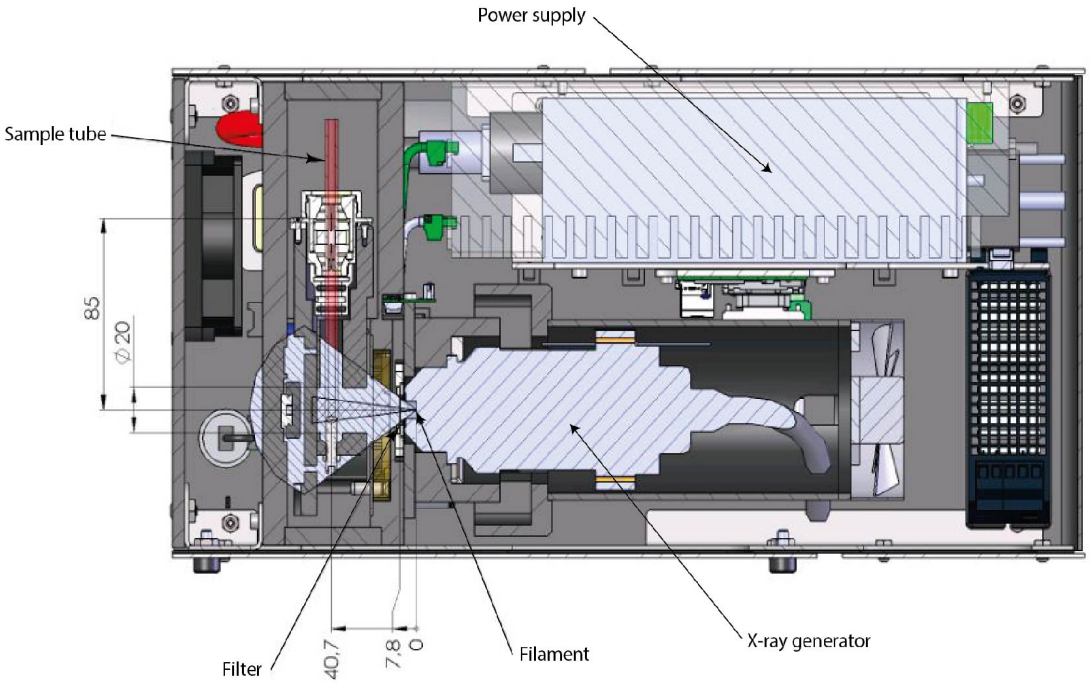

a)

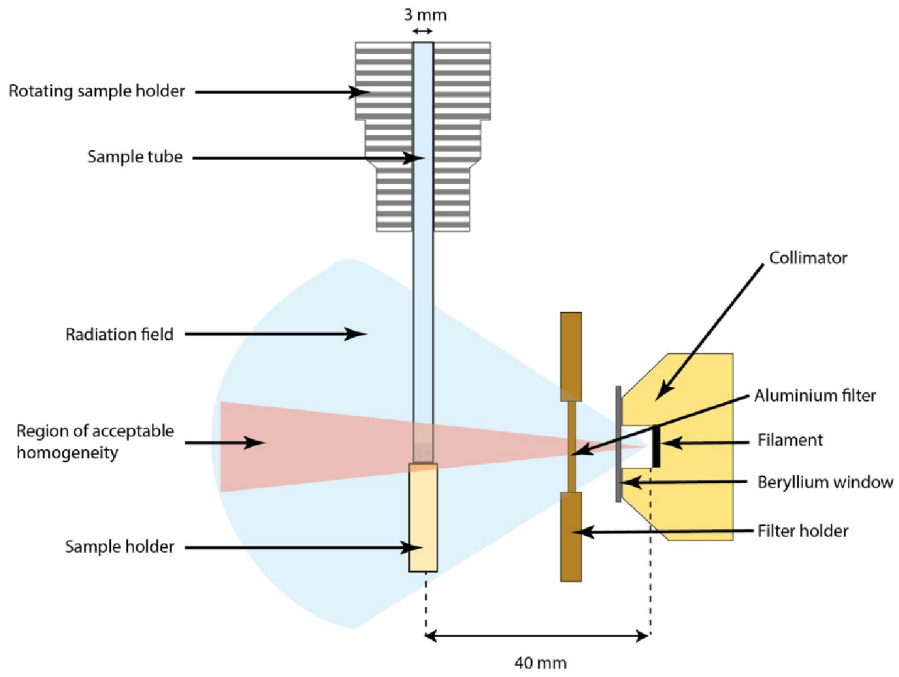

b)

Figure 1. Schematic representation of the "X-ray dose"; a) figure taken from the Freiberg Instrument manual representing the entire apparatus and b) figure of the sample tube positioning during irradiation. Redrawn from the Freiberg Instrument manual (figure not to scale). The region of acceptable homogeneity is arbitrarily defined as the region within which the radial variation in absorbed dose is less than 5 %.

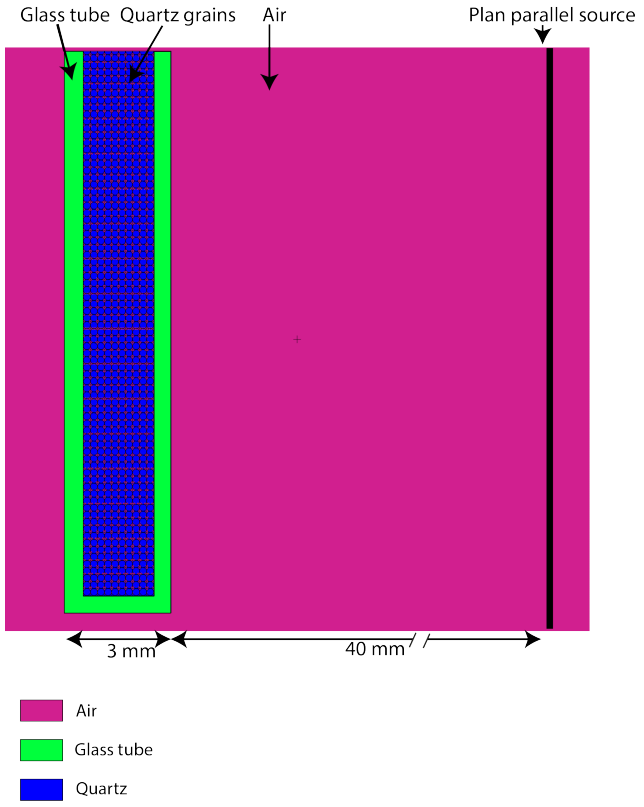

Figure 2. Geometry employed to model the irradiation of samples of granular quartz inside a glass sample tube with the Freiberg Instruments X-ray generator "X-ray dose". The geometry was plotted using the MCNP plotter and later modified.

in a cell times the energy deposited (*F8 tally). The code was run until all 10 MCNP statistical checks converged - evaluating the mean error, the variance, the variation of the figure of merit and the slope of the probability density function. The errors indicated are MCNP statistical errors only and thus do not include the systematic errors inherent to the simulation of an experimental setup. Where necessary, the errors were propagated using a Monte-Carlo procedure implemented in the software Matlab.

Sample name	**Origin**
KRG113	Granitic bedrock, Japanese Alps
NUS18	Sandy limestone, Al Wafa site (28°00′58.4″N, 10°47′52.3″E), Lybia
RisøCalQz0Gy	Quartz sand, Rømø, Denmark (Hansen et al., 2015)

Table 1. List of samples selected to calibrate the X-ray source with their origin

2.3. Luminescence dosimetry

Three quartz samples of different origins (listed in Table 1) were selected to experimentally quantify the absorbed dose heterogeneity of an individual EPR aliquot irradiated with the X-ray source. The samples were prepared using standard methods to extract the granular quartz fraction in the range 180 – 212 µm. The samples were subjected to a thermal treatment (400 °C, 4 min) to zero the signal and then irradiated for 100 s in EPR glass samples tubes (3 mm outside diameter, 2 mm inside diameter) using the X-ray source operating at a voltage of 50 keV and a current of 1 mA. No filters were used when irradiating the samples, as Section 3 will show that the use of filters was not necessary in our setup.

The resulting absorbed dose in the grains of quartz was measured using optically simulated luminescence (OSL) methods. The measurements were performed using a Risø model 20 reader (DTU Nutech, Denmark) that incorporated a ^{90}Sr/^{90}Y β radiation source. The luminescence emission was detected through a UV pass colour glass filter (U-340) using an Electron Tube 9235Q PMT (160 – 630 nm). The β source of the luminescence reader was calibrated using quartz irradiated with a ^{137}Cs γ source at DTU Nutech, whose dose-rate to grains of quartz is calibrated and characterised (Hansen et al., 2015) and was evaluated to deliver 0.091 ± 0.007 Gy·s^{-1} to grains mounted on single-grain aluminium discs, at the date of measurement. The β dose-rate was corrected for the heterogeneity of the source across the single-grain measurement discs. The absorbed dose to grains of quartz was determined by applying a single aliquot regenerative dose procedure (SAR; Murray & Wintle 2000) using a 10 s Nd:YVO_4 solid-state diode-pumped laser light stimulation (532 nm; with a power at the sample position of 10 mW·cm^{-2} as stated by the manufacturer at the time of purchase; Bøtter-Jensen et al. 2000), a 260 °C preheat (10 s hold time) and holding the samples at 125 °C during the OSL measurement. Unless otherwise specified, the rejection criteria applied included a maximum X-ray dose and test dose (18 Gy) error of 10 % and a recycling ratio < 0.1. β dose-recovery tests carried out on 12 further aliquots of the same samples, following thermal annealing and administration of a β dose of 11.8 ± 0.9 Gy, indicated that this protocol was suitable to recover doses within 3%. These experiments also served to constrain the sample-specific intrinsic OSL absorbed dose heterogeneity, which is discussed further in Section 4.1.

2.4. EPR dosimetry

MCNP simulations could be used to calculate dose-rates, however we would have needed to make a number of approximations to achieve this, e.g. as the energy spectrum of the X-ray source is unavailable, we would have had to approximate it. Instead, we calculate the dose rate by determining the X-ray irradiation time required to yield the equivalent EPR signal as a known gamma dose.

Aliquots of the KRG113 samples were irradiated with a known dose at the Ecole Polytechnique Fédérale de Lau-

sanne (EPFL) using a ^{60}Co source (LOTUS) and measured following a single-aliquot regenerative protocol similar to that of Tsukamoto et al. (2015), where the regenerative points were obtained by irradiating the samples with the X-ray source. The heterogeneity in delivered dose during the gamma irradiation was evaluated using MCNP to be < 1 %. To avoid spurious signal induced by radicals formed by irradiation of the glass measurement tube, the tube was inverted between the X-ray irradiations and the EPR measurements, so that the part of the tube exposed to radiation was outside of the measurement chamber of the spectrometer. The γ-irradiated samples were irradiated in a glass vial before being decanted into measurement tubes. EPR measurements were performed using a Magnettech MS5000X X-band EPR spectrometer operating at low temperature (100 K) using liquid nitrogen. The acquisition was carried out using a microwave power of 5 mW, a modulation amplitude of 0.1 mT and a modulation frequency of 100 kHz. The Al and Ti centres were measured together in a single spectrum with a sweep amplitude of 31 mT, between 325 and 356 mT, for a total sweep time of 100 s, and averaged across three acquisitions. Each spectrum was repeated on three different days and averaged after rotating the sample tube by 120°, to average any anisotropic effects. Each aliquot was zeroed by administering a thermal treatment (400 °C, 4 min), as this treatment has been shown to cause negligible sensitivity changes (Tsukamoto et al. 2015; Toyoda et al. 2009). The samples were preheated at 160 °C for 4 min prior to measurement. Thermal treatments were carried out in a high precision heating unit designed for EPR sample tubes (Freiberg instruments). The Al signal was measured as the peak-to-peak amplitude from the top of the first peak (g = 2.0185) and the bottom of the 16th peak (g = 1.9928; Toyoda & Falguères 2003). The Ti signal was measured as the peak to baseline amplitude around g = 1.913, following the suggestion of Duval & Guilarte (2015; option D). Dose recovery tests for the regenerative protocol on this sample indicated an excellent dose recovery ratio, both for the Al and the Ti centres (3.3 % and 7.2 % respectively). The dose-rate of the X-ray source was calculated by evaluating the irradiation time needed by the X-ray source to reach a signal equivalent to that of the known γ dose.

3. Results

3.1. Deposition spectrum and effect of the glass tube relative to an aluminium filter

Previous work has shown that the use of a filter (typically aluminium, 200 µm) is necessary when irradiating samples directly exposed to the x-ray beam (i.e., not within a container) with a Varian VF-50J X-ray tube. This is to harden the spectrum by suppressing the low energy emission (< ~ 15 keV) that would otherwise lead to dose rate heterogeneity between quartz samples for trapped-charge dosimetry (Thomsen et al., 2006).

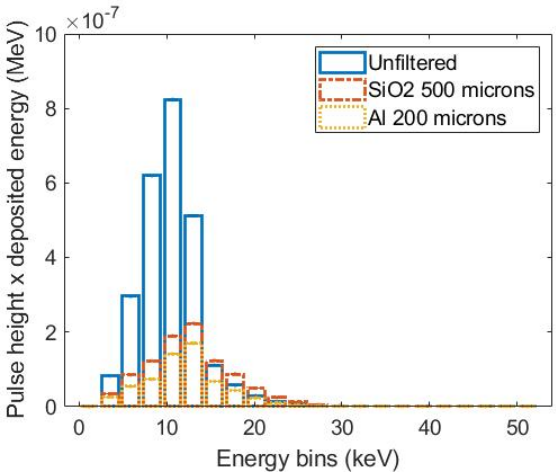

Figure 3. Energy spectrum of absorbed dose in an air cell 40 mm from the source. The spectrum was calculated for an unfiltered source (blue continuous line), a 200 µm aluminium filter (yellow dotted line), and a 500 µm glass wall (orange dashed line). The MCNP statistical errors are < 1% and cannot be discerned by eye.

The spectrum of the deposited energy was calculated at the sample position (40 mm from the source) in an air cell (1 x 1 x 0.3 cm^3) using the *F8 tally in three configurations: 1) unfiltered source, 2) 200 µm aluminium filter placed between the source and the detector and 3) 500 µm of glass between the source and the detector that replicates the wall of the sample tube. In agreement with previous studies (Fig. 2 of Richter et al. 2016), the results of these simulations indicate a strong reduction of absorbed dose between the unfiltered and filtered source at energies below ~ 15 keV (Figure 3), resulting in a general hardening of the spectrum which is similar where the source is filtered using either 500 µm of glass or 200 µm of aluminium. Furthermore, the dose rate is predicted to decrease by 63 % and 76 % for a source filtered using either 500 µm of glass or 200 µm of aluminium, respectively, compared with an unfiltered source.

These results are consistent with the GaF chromic film measurements carried out by Oppermann & Tsukamoto (2015), who estimated that absorption caused by a glass tube is ca 60 % of the unfiltered energy. The predicted reduction in dose rate is also comparable with the calculations of Andersen et al. (2003), who predicted a 50 % reduction in dose for 500 µm of SiO_2 (half-layer value), for ~ 17 keV photons, that they calculated roughly correspond to the mean energy of a 50 keV source.

As our simulation shows that the effect of the glass wall is similar to that of the aluminium filter, in terms of spectrum hardening, the use of an aluminium filter is not necessary when irradiating quartz samples for EPR analysis. All further simulations presented in this study thus exclude the Al filter. Removal of the Al filter from the "X-ray Dose" system has the considerable benefit of avoiding an unnecessarily loss in dose-rate of 56 % which would be caused by excessive spectrum filtering through the combination of the Al filter and the glass sample tube wall.

3.2. Radiation field homogeneity

Minimum sample masses of between 30 mg up to 200 mg are required for EPR analysis. Sample tube rotation has recently been introduced in the Freiberg Instrument X-ray dose system to improve radial dose homogeneity of the X-ray beam, due to absorption. We evaluated its effectiveness by simulating dose absorption in both rotating and non-rotating tubes. To avoid heterogeneity in the absorbed dose of the material, narrow sample tubes are used which result in sample heights of between 1 cm and 3 cm. Consequently, in addition to determining the radial dependence of the absorbed dose rate, it is also essential to constrain the axial dose rate dependence (Figure 4).

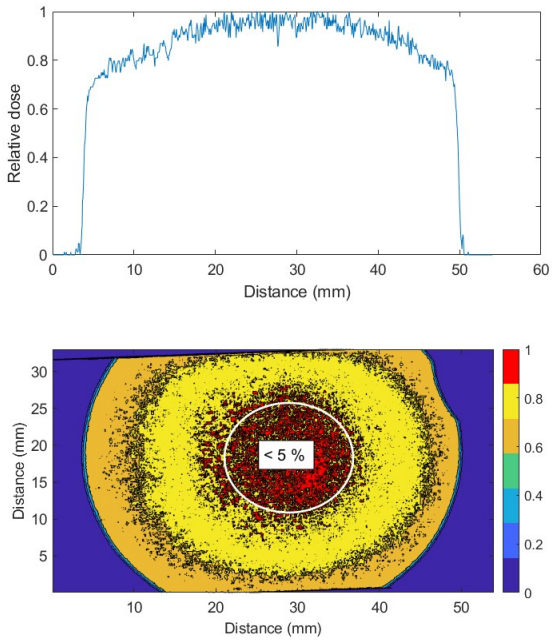

Figure 4. Mesh tallies representing a) the photon flux across a non-rotating 3 mm sample tube filled with 200 µm diameter quartz grains. The photon flux is visualised using the MCNP6 Mesh tally 1 for photons only. b) Absorbed dose across a non-rotating 3mm sample tube filled with 200 µm diameter quartz grains. The absorbed dose in each mesh cell was calculated using the MCNP mesh tally 3, equivalent to the F6 tally.The values indicated are MCNP normalised values per particle.

3.2.1 Radial dependence

Variation of deposition spectrum: The deposition of energy changes across the tube in the radial direction, as the beam is attenuated. Therefore, the deposited energy spectrum also changes across the tube as the lowest energies are progressively absorbed. In this section, we explore axial changes in the deposited energy; drastic changes in the energy deposited would require correction. As shown in Figure 5, whilst the peak in the energy spectrum for a 200 µm diameter grain located closest to the glass wall (i.e. at a median distance of 100 µm) is around ~20 keV, it is shifted to ~28 keV for a grain of the same diameter farthest from the source (900 µm). Grains farthest from the source are also exposed to an energy spectrum with a less pronounced energy peak. The mean deposited energy is, however, relatively similar between grains: ~24.8 keV for the grain closest to the source and ~26.2 keV for the grain farthest from the source.

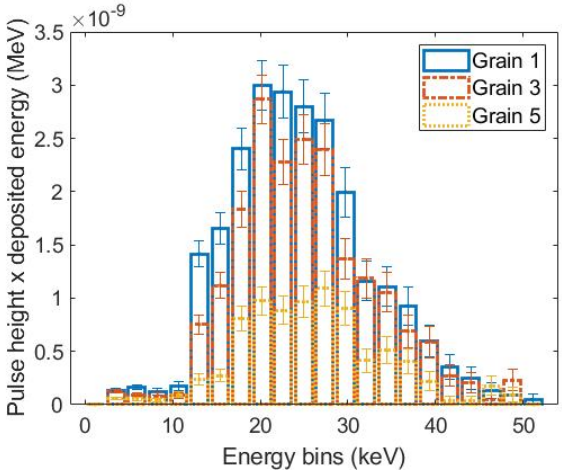

Figure 5. Variation in absorbed dose in each grain along the beam axis for a rotating sample tube. The absorbed dose in each grain was normalised by the absorbed dose in the grain closest to the glass wall (and the source). The profile was calculated for two different grain sizes: 250 µm diameter (orange dashed line) and 100 µm diameter (blue dotted line). The errors shown are the MCNP statistical errors only.

Across-tube dose attenuation: Mesh tallies were used to offer a visual representation of the distribution of absorbed dose across the tube for a non-rotating sample. Figure 6a shows the photon flux, calculated using Mesh tallies of type 1 (flux), equivalent to the F4 tally in MCNP. As expected, there is a strong dose gradient across the geometry. The spatial distribution of the absorbed dose for a non-rotating sample was evaluated using the MCNP mesh tally 3, equivalent to the F6 tally, and a visual representation is shown in Figure 6b. The distribution in absorbed dose is highly heterogeneous across the sample tube, with a reduction in absorbed dose of 70 %; this result emphasises the importance of rotating the sample during irradiation.

The variation in absorbed dose across the tube for a rotating sample was evaluated by averaging the absorbed dose in a grain with its opposite grain on the axis along the beam. The resulting profile was then normalised to the first grain closest to the source to better evaluate the proportion of absorption across the tube (Figure 7). For these calculations, the F6 tally was employed as it was found that the *F8 tally could not yield a statistically satisfactory answer, presumably due to the small size of the detector grains. Figure 7

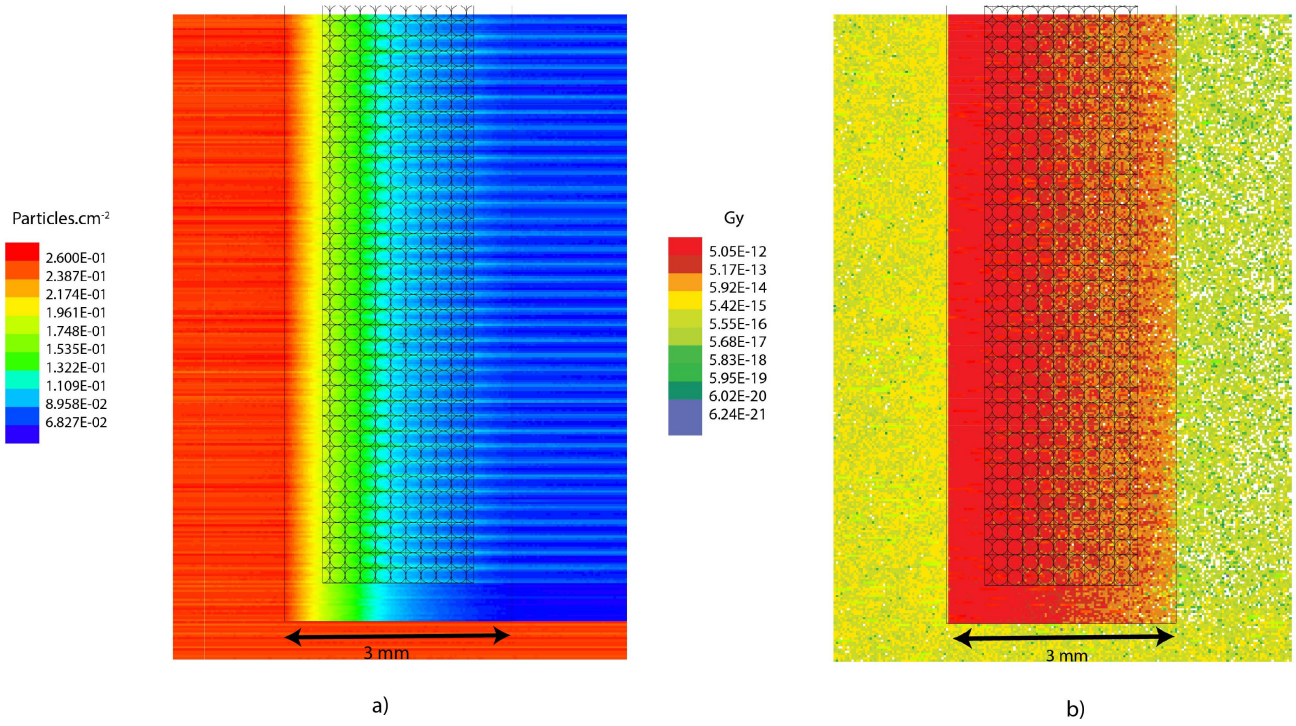

Figure 6. Axial heterogeneity in dose as evaluated by irradiating GaF radiochromic film and processing the image using the red component. The data points were normalised by the maximum measured dose, at the centre of the beam. Top graph: profile along the x-axis at the centre position. The top figure is for illustrative purposes only. Small displacements of the film can occur, and cause the offset of the maximum value from the centre. Bottom graph: full map of the 2D spatial heterogeneity. The white circle indicates the region within which the reduction in dose is less than 5 %. To achieve a more homogeneous irradiation, the sample has to be positioned within the "<5 %" circle. This is done using a positioning screw placed underneath the sample tube.

shows the profile in absorbed dose across the tube for two grain size fractions (100 and 250 µm). Although there seems to be a slight reduction in absorbed dose for different grain sizes in the range 100 – 250 µm, with a reduction of 30 and 26 % at the centre of the tube respectively, this variation can be considered as negligible, within uncertainties. Thus, on average for grains between 100 – 250 µm diameter, a 28 % decrease at the centre of the tube, compared with grains located by the glass wall is observed. This equates to a mean absorbed dose in the sample of ca 83 % of the given dose.

3.2.2 Axial dependence

The axial variation in dose was measured using GaF radiochromic film. Although the films were not calibrated for an absolute assessment of the dose, they provide an estimate of the relative variation in dose across the beam. The image was processed using Matlab. These measurements indicate that the threshold of satisfactory dose homogeneity, arbitrarily chosen to be < 5 % variation, was obtained over a sample height of 2.4 cm (Figure 4). This was thus set as the maximum height of samples for irradiation, with the lowest extent of the sample tube position fixed at the bottom of the < 5 % inhomogeneity zone. These values are slightly better than those reported by Oppermann & Tsukamoto (2015), who found relative dose variations of ca. 5.6 % within a height of 2 cm in their setup.

4. Model validation and calibration

EPR measurements were used to calibrate the X-ray source for grains of quartz in the fraction 180 – 225 µm, and luminescence measurements were used to experimentally assess the X-ray source radiation field radial divergence. Sample heights did not exceed 2.4 cm to ensure axial X-ray source heterogeneity in the absorbed dose was limited to < 5% (see Section 3.2.2). Luminescence measurements were performed by irradiating grains of quartz with the X-ray source for 100 s and measuring the resulting absorbed dose using a single-grain SAR protocol tailored for quartz (see Section 2.3 for experimental details). EPR dosimetry measurements were conducted by irradiating previously zeroed quartz samples with a known γ dose (350 $\pm$ 12 Gy to quartz; ^{60}Co LOTUS source, EPFL, Lausanne, Switzerland) and evaluating the X-ray equivalent γ dose using a SAR protocol, employing the X-ray source for the regenerative data points.

Sample name	Measured over-dispersion X-ray irradiated sample (%)	Measured over-dispersion β irradiated dose-recovery tests (%)	Accepted grains β-irradiated (%)	Accepted grains X-ray irradiated (%)	β dose recovery ratio
RisøCalQz$_{0Gy}$	31.1	7.6	79.7	30.6	1.01 ± 0.009
NUS18	32.9	8.0	90.1	21.5	1.03 ± 0.009

Table 2. Over-dispersion obtained from two quartz samples (RisøCalQz0Gy, NUS18). For the X-ray irradiated data, the samples were irradiated for 100 s in an EPR sample tube using the X-ray source operating at 50 kV, 1mA. For the β irradiated data, the samples were irradiated with 11.8 ± 0.9 Gy in a Risø TL-DA-20 instrument. For both the X-ray and β irradiated data, the subsequent doses were determined using an OSL single-grain SAR measurement procedure.1200 grains were measured for single-grain measurements.

4.1. Evaluating the heterogeneity: an experimental approach

The MCNP calculations predict heterogeneity in absorbed dose between grains irradiated within a tube; this heterogeneity should be visible as extrinsic over-dispersion in single-grain luminescence measurements. Samples RisøCalQz0Gy and NUS18 were used for single-grain measurements, sample KRG113 unfortunately has luminescence properties unsuitable for dose assessment, mainly due to a poor luminescence signal-to-noise ratio, as is typical for bedrock quartz. In contrast, the EPR properties of KRG113 were suitable for dose assessment and this sample is used for EPR calibration of the X-ray source in the next section.

Aliquots of 2 cm in height of samples NUS18 and RisøCalQz$_{0Gy}$ were irradiated in the X-ray source setup (100 s, 50 keV, 1 mA); the aliquot size was chosen to minimise the radial heterogeneity. The OSL measurements were done specifically to obtain a measurement of the dose heterogeneity, rather than absolute doses, and were done using a single-grain SAR protocol. The over-dispersion in the X-ray irradiated samples was compared with the over-dispersion of the β dose recovery test, performed on different aliquots (Table 2, Section 2.3) and is shown in Figure 8. The over-dispersion obtained from the β dose-recovery test is intrinsic to our TL/OSL reader, the sample and single-grain measurements (i.e., to the method; loss or gain of counts from the PMT, beta source heterogeneity, reproducibility of single-grain measurements due laser positioning, see Thomsen et al. 2005). In contrast, the over-dispersion measured for grains irradiated in the X-ray source setup is a combination of extrinsic over-dispersion from heterogeneity of the X-ray radiation field and the intrinsic single-grain measurement over-dispersion. As is illustrated in Figure 8, a far greater dispersion is observed for the X-ray irradiated samples.

4.2. EPR calibration

Three aliquots of ^{60}Co irradiated KRG113 were measured using EPR measurement techniques and the dose evaluated using a SAR protocol, such as described in Section 2.4 The regenerated dose response curve was found to be linear in the dose range considered (< 515 Gy) and thus was fitted with a linear function onto which the γ-induced signal was interpolated.

The EPR calibration gave dose-rate values in close agreement between the Al and Ti centres of 0.206 ± 0.008 Gy·s^{-1} and 0.206 ± 0.009 Gy·s^{-1} respectively. The uncertainty indicated here is simply the standard error derived from the three aliquots measured. However, as highlighted by the modelling results, this error does not describe the full dose-rate heterogeneity, which will be discussed in the following section.

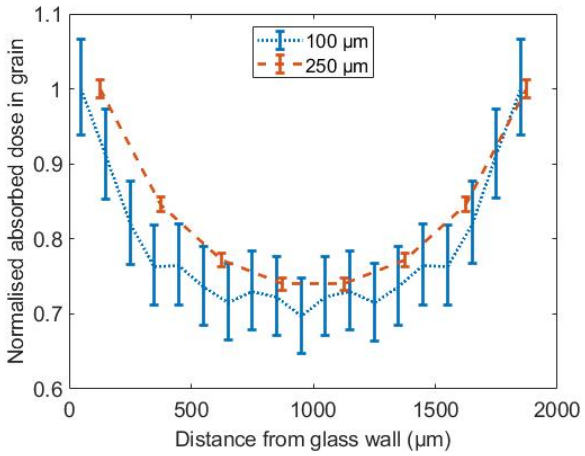

Figure 7. Deposited energy spectrum for 200 µm diameter quartz grains centred 100 µm from the glass wall (grain 1), 500 µm (grain 3) and 900 µm (grain 5) for a non-rotating sample tube. The errors shown are the MCNP statistical errors only.

5. Discussion

The energy spectrum calculated here predicts a peak X-ray dose deposition in air at photon energies between 10 and 12 keV for an unfiltered X-ray source and between 12 and 14 keV for an X-ray source filtered by either 200 µm thick aluminium or 500 µm thick glass. In our study, we have stimulated the energy deposition spectrum in air, at the location of the sample, whereas previous studies such as Thomsen et al. (2006) have stimulated the energy emitted by the source. It is expected that the energy spectrum presented in this study yields a lower emission peak. Therefore, our peak absorption value is consistent with the peak emission of ~ 20

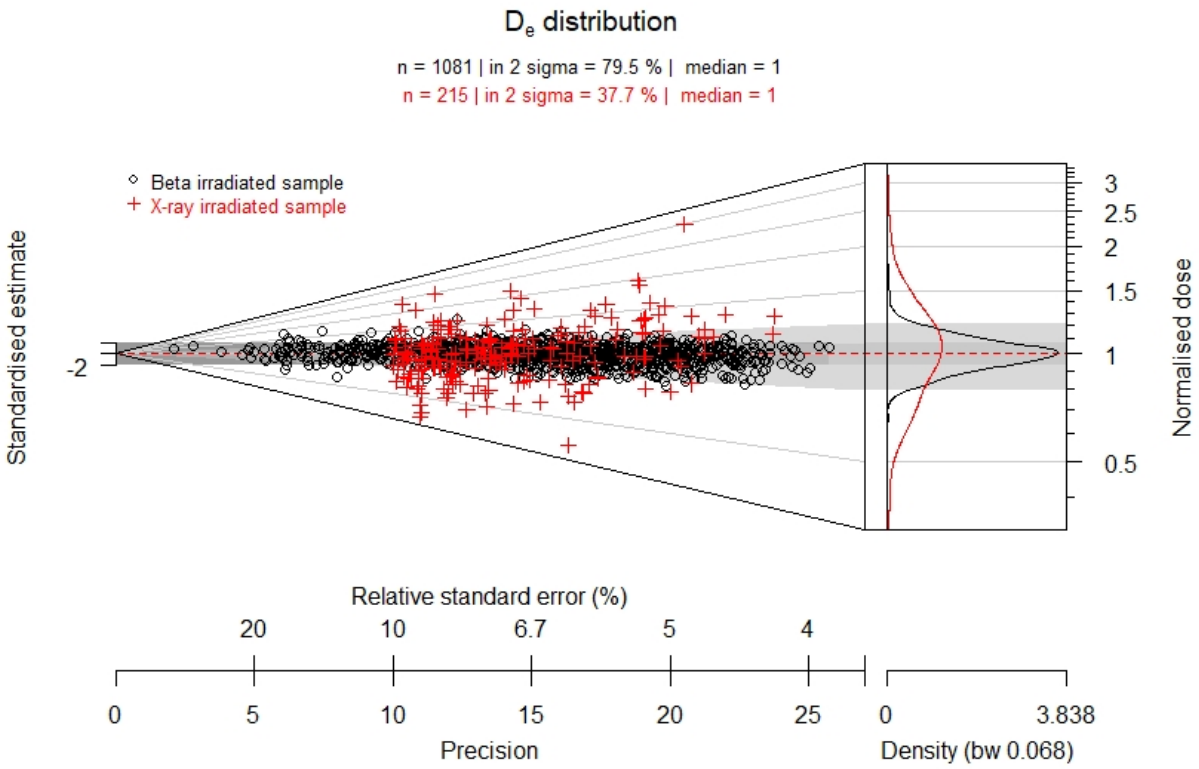

Figure 8. Abanico plot of measured equivalent doses for NUS18 samples irradiated using the X-ray source (black crosses) and using the Risø TL-DA-20 luminescence reader built-in β source (open red circles, as part of the dose-recovery test). The doses were normalised to the median dose of each dataset to allow easier visualisation of the spread in distribution.

keV reported by Thomsen et al. (2006). Furthermore, it is also close to the peak absorption value of ~ 15 keV proposed by Richter et al. (2016), where the X-ray emission and absorption spectra were calculated using Kramer's rule. Andersen et al. (2003) used Kramer's law for a thick target to calculate the mean emission energy for an unfiltered source and obtained a mean energy of ~ 17-19 keV. However, both our approach and Andersen's approach make a number of assumptions (e.g., thickness of the target, classical approximation in Andersen's case; exact emission spectrum of the source in our case). Furthermore, the precision of the predicted energy maximum is limited in our calculations by the size of the simulation bin width (2.38 keV). Simulations using smaller energy bins did not, however, yield satisfactory statistical checks for the maximum number of particles run (2.1×10^9).

The simulation results presented here validate the prediction of Richter et al. (2016), that the glass wall of the sample tube has the same effect as a 200 µm aluminium filter and therefore that the latter is not necessary when irradiating quartz samples in a glass tube. This finding is important as removing the Al filter results in an increase in the effective dose rate of 35 %, significantly accelerating sample throughput within the laboratory. This is especially significant for EPR measurements that are often applied to mid-early Pleistocene samples with absorbed doses far beyond the saturation limits of most luminescence dating methods (Rink et al., 2007).

Simulations of the axial and radial absorbed dose heterogeneity revealed considerable spatial variations. GaF film measurements showed that EPR samples irradiated in the Freiberg Instruments X-ray dose system that exceed 2.4 cm in height will have dose rate heterogeneity of > 5 % (Figure 4), whilst quartz grains measured in 3 mm diameter tubes experience a radial dose heterogeneity of ca. 28%, as predicted by MCNP, due to the attenuation of low energy X-rays throughout the sample's tube.

Although there is considerable over-dispersion in absorbed doses for samples irradiated in this setup, as assessed using luminescence single-grain measurements, the dose distribution should, in principle, be reproducible from one irradiation to another. This is confirmed by the small standard error in dose-rate between the three gamma-irradiated aliquots (< 3 %), measured using EPR to calibrate the X-ray source, where samples were repeatedly irradiated with the X-ray source to regenerate the dose points of a SAR protocol.

However, this uncertainty does not address potential variability in the strength and dose response of EPR signals between grains (Beerten et al., 2003). Indeed, if EPR signals are largely variable between grains, the EPR signal registered following irradiation of a sample would not be representative of the dose distribution across the sample tube – but rather

would be biased towards the grains exhibiting a stronger signal. However, as the grain by grain heterogeneity in EPR response is unquantified and may vary between samples, and as a large number of grains are irradiated and measured each time (tens to hundreds of mg), we have not accounted for this potential heterogeneity in our error estimates.

Nevertheless, a recommendation that can be derived from the apparent inherent dose distribution would be to avoid creating subsets of the sample following irradiation in this setup, at the risk of having an unknown dispersion in dose in the grains of the resulting samples. We note that using a hardening filter would increase the mean energy of the beam, and thus reduce the heterogeneity, whilst reducing the overall dose rate. Finally, the tube diameter is crucial, as a larger diameter would mean stronger attenuation across the tube, hence a higher radial heterogeneity.

Much recent trapped charge dosimetry research has focussed on feldspar minerals. Preliminary modelling results show that feldspar samples irradiated in the exact same setup, and without a hardening filter, as described here will show a higher absorption than quartz (76 % vs 65 % absorption across a non-rotating sample tube respectively). Thus, radial heterogeneity will be greater, yielding a lower effective dose-rate. Therefore, all the considerations summarised in this article, as well as the dose-rate measured here should not be translated to the irradiation of feldspar samples.

6. Conclusion

Using a combination of MCNP simulations, GaF film and single-grain luminescence measurements, we have shown that the irradiation of EPR samples in 3 mm diameter glass tubes using a filtered 50 keV X-ray source is inherently heterogeneous, even for samples that rotate throughout irradiation. The absorbed dose measured using EPR following irradiation is thus an average of the dose across the sample tube, assuming uniform grain response. Our simulations indicate that the use of an aluminium filter (200 µm) is redundant with the use of glass sample tubes (500 µm wall thickness), as the two materials yield similar X-ray spectrum hardening. Therefore, we refrained from using an aluminium filter in the experimental part of our study.

The dose-rate of our X-ray source to grains of quartz in the fraction 180 – 212 µm was measured using EPR dosimetry to be 0.206 ± 0.005 Gy·s^{-1}, averaging the dose-rate values for the Al and Ti centres together. It is, however, an average dose of the distribution in dose across the tube, that would be bound to change for tubes of smaller/larger diameter. The MCNP results indicate that this dose-rate is also valid for grains in the finer fraction (100 – 250 µm). The calculated dose-rate assumes a homogeneous – or at least reproducible – response between grains within an aliquot; i.e. that grain response is evenly distributed spatially, resulting in effective dose averaging. The small standard error between the three aliquots measured seems to indicate that this is the case, at least for this sample.

Acknowledgements

The authors wish to thank Shigeru Sueoka (Japan Atomic Energy Agency) and Takahiro Tagami (Kyoto University) for facilitating the field trip during which the sample KRG113 was collected and Simon Armitage (Royal Holloway) for providing the sample NUS18. Daniel Richter is acknowledged by the authors for providing the emission spectrum. The authors would also like to thank Pavel Frajtag, Laurent Braun, Daniel Godat and the EPFL LOTUS group for providing access to the ^{60}Co source, setting up the irradiation geometry and the calibration of the source.

This research was supported by funding from the European Research Commission (ERC) under the European Union's Horizon 2020 research and innovation programme, grant number 851614. The authors are also greatly thankful to Melanie Bartz for her suggestions and proofreading on the manuscript, and Federico Geser for his help with Monte-Carlo simulations.

References

Andersen, C. E., Bøtter-Jensen, L., and Murray, A. S. *A mini X-ray generator as an alternative to a 90Sr/90Y beta source in luminescence dating*. Radiation Measurements, 37(4-5): 557–561, 2003.

Autzen, M., Guérin., Murray, A. S., Thomsen, K. J., Buylaert, J. P., and Jain, M. *The effect of backscattering on the beta dose absorbed by individual quartz grains*. Radiation Measurements, 106: 491–497, 2017.

Bailiff, I. K. *An examination of beta dose attenuation effects in coarse grains located in sliced samples*. Radiation Measurements, 120: 188–194, 2018.

Beerten, K. and Stesmans, A. *ESR dating of sedimentary quartz: possibilities and limitations of the single-grain approach*. Quaternary Geochronology, 2(1-4): 373–380, 2007.

Beerten, K., Pierreux, D., and Stesmans, A. *Towards single grain ESR dating of sedimentary quartz: first results*. Quaternary science reviews, 22(10-13): 1329–1334, 2003.

Bøtter-Jensen, L., Bulur, E., Duller, G. A. T., and Murray, A. S. *Advances in luminescence instrument systems*. Radiation Measurements, 32(5-6): 523–528, 2000.

Duller, G. A. T., Bøtter-Jensen, L., and Murray, A. S. *Optical dating of single sand-sized grains of quartz: sources of variability*. Radiation Measurements, 32(5-6): 453–457, 2000.

Duval, M. and Guilarte, V. *ESR dosimetry of optically bleached quartz grains extracted from Plio-Quaternary sediment: Evaluating some key aspects of the ESR signals associated to the Ti-centers*. Radiation Measurements, 78: 28–41, 2015.

Goorley, T., James, M., Booth, T., Brown, F., Bull, J., Cox, L. J., Durkee, J., Elson, J., Fensin, M., Forster, R., Hendricks, J., Hughes, H., Johns, R., Kiedrowski, B., Martz, R., Mashnik, S., McKinney, G., Pelowitz, D., Prael, R., Sweezy, J., Waters, L.,

Wilcox, T., and Zukaitis, T. *Initial MCNP6 release overview*. Nuclear Technology, 180(3): 298–315, 2012.

Götze, J. and Lewis, R. *Distribution of REE and trace elements in size and mineral fractions of high-purity quartz sands*. Chemical Geology, 114(1-2): 43–57, 1994.

Hansen, V., Murray, A., Buylaert, J. P., Yeo, E. Y., and Thomsen, K. *A new irradiated quartz for beta source calibration*. Radiation Measurements, 81: 123–127, 2015.

Kook, M. H., Murray, A. S., Lapp, T., Denby, P. H., Ankjærgaard, C., Thomsen, K., Jain, M., Choi, J.-I., and Kim, G. *A portable luminescence dating instrument*. Nuclear Instruments and Methods in Physics Research Section B: Beam Interactions with Materials and Atoms, 269(12): 1370–1378, 2011.

Murray, A. S. and Wintle, A. G. *Luminescence dating of quartz using an improved single-aliquot regenerative-dose protocol*. Radiation Measurements, 32(1): 57–73, 2000.

Oppermann, F. and Tsukamoto, S. *A portable system of X-ray irradiation and heating for electron spin resonance (ESR) dating*. Ancient TL, 33: 11–15, 2015.

Pelowitz, D. B. *MCNP6 user's manual version 1.0*. LANL Report: LA-CP-, pp. 13–00634, 2013.

Richter, D., Mittelstraß, D., Kreutzer, S., Pintaske, R., Dornich, K., and Fuchs, M. *A new fully integrated X-ray irradiator system for dosimetric research*. Applied Radiation and Isotopes, 112: 122–130, 2016.

Rink, W. J., Bartoll, J., Schwarcz, H. P., Shane, P., and Bar-Yosef, O. *Testing the reliability of ESR dating of optically exposed buried quartz sediments*. Radiation Measurements, 42(10): 1618–1626, 2007.

Thomsen, K. J., Murray, A. S., and Bøtter-Jensen, L. *Sources of variability in OSL dose measurements using single grains of quartz*. Radiation Measurements, 39(1): 47–61, 2005.

Thomsen, K. J., Bøtter-Jensen, L., Denby, P. M., and Murray, A. S. *Luminescence response to irradiation using mini X-ray generators*. Nuclear Instruments and Methods in Physics Research Section B: Beam Interactions with Materials and Atoms, 252(2): 267–275, 2006.

Toyoda, S. and Falguères, C. *The method to represent the ESR signal intensity of the aluminium hole center in quartz for the purpose of dating*. Advances in ESR applications, 20: 7–10, 2003.

Toyoda, S., Miura, H., and Tissoux, H. *Signal regeneration in ESR dating of tephra with quartz*. Radiation Measurements, 44(5-6): 483–487, 2009.

Tsukamoto, S., Toyoda, S., Tani, A., and Oppermann, F. *Single aliquot regenerative dose method for ESR dating using X-ray irradiation and preheat*. Radiation Measurements, 81: 9–15, 2015.

Reviewers

Daniel Richter and Dirk Mittelstraß

Ancient TL

Comparing two efficiency calibration methods used in gamma spectrometry

Barbara Mauz[1*], Alexander Hubmer[2], Chiara Bahl[1], Herbert Lettner[2], Andreas Lang[1]

[1] Department of Geography and Geology, University of Salzburg, 5020 Salzburg, Austria
[2] Biological Physics, Chemistry and Physics of Materials, University of Salzburg, 5020 Salzburg, Austria

*Corresponding Author: barbara.mauz@plus.ac.at

Received: September 27, 2021; in final form: December 7, 2021

Abstract

The recent inter-laboratory comparison study revealed considerable differences between laboratories for activity concentrations of U, Th and K. One reason for these differences could be materials and methods employed for calibrating the detector's efficiency. To address this, we determined the activity concentrations of unknown samples originating from variable geochemical environments using two different efficiency calibration methods: one is based on the direct comparison with the non-certified Volkegem internal standard and the other one uses a certified multi-nuclide reference solution and correction factors for full-energy efficiency, emission probability, true coincidence summing and for sample density. The comparison is based on the hypothesis that consistency between the two methods raises the probability that the activity concentrations determined are accurate. We show here that agreement between the two methods is obtained when the Volkegem activity reference values of ^{40}K and ^{238}U-series are raised by 9%. For the ^{232}Th-series agreement is obtained for the two photon peaks at 338 keV and 911 keV when deploying the published activity reference value. We conclude that the efficiency calibration method should not account for more than 10% variability and cannot be the sole reason for the alarming differences revealed by the inter-laboratory comparison study.

Keywords: detector efficiency, calibration, internal standard, reference material

1. Introduction

Low-level gamma spectrometry is often used to determine the environmental radioactivity of samples. In fact, in the recent inter-laboratory comparison study (Murray et al., 2015) most laboratories determined the dose rate on the basis of γ-spectrometry. Yet, discrepancies appeared in the comparative dataset especially for the ^{232}Th data, whereas the ^{40}K data showed reasonable agreement. While it is good to see reasonable agreement for ^{40}K activity concentrations which constitutes the largest proportion of the total dose rate, the overall discrepancy suggests that some dose rates determined by γ-spectrometry are significantly inaccurate.

A number of parameters govern the quality of the γ-spectrometric data (e.g., measurement geometry, selection of photon peaks, etc), most of which are specific to the detector and the measurement procedure. The one parameter affecting all laboratories is the reference material and the associated efficiency calibration method and this may play an important role in dose-rate inaccuracies (e.g., Murray et al. 2018). Here we address this hypothesis through an empirical study that looks at the significance of the efficiency calibration method for obtaining accurate activity data for ^{40}K, ^{238}U and ^{232}Th of unknown samples. The comparison is based on 81 samples arbitrarily selected from our laboratory's sample pool. Because the activities of these samples are not known independently, the study looks at the consistency of activity data derived from the two calibration methods. If the comparison shows systematic deviation from unity, one or the other method is likely inaccurate. If deviations are random, parameters other than the calibration method must be tested. We show that inaccuracy is not very likely for all photon peaks relevant for dose-rate estimation and for both methods tested. It is suggested that other laboratory parameters cause the discrepancies shown in the inter-laboratory comparison study (Murray et al., 2015).

	Resolution FWHM (keV)				Diameter (mm)	Length (mm)	Efficiency (%) at 1332 keV
Energy (keV)	**60**	**122**	**662**	**1332**			
	0.92	0.98	1.39	1.85	61.8	77.8	54

Table 1. Properties of the coaxial (n) Ge detector (serial no 46-TN32165A) used in this study (ORTEC Quality Assurance Data Sheet, 2006). FWHM = full width half maximum of energy peak.

2. Methods and Materials

2.1. Detector and measurement details

The detector used in this study is a coaxial n-type high purity Germanium (Ge) detector (for details see Table 1) which sits in a castle composed of low-activity lead (10 cm), cadmium tin (1 mm), copper (2 mm) and perplex (6 mm). Dry and occasionally crushed samples were filled in cylinder-type sample holders which were subsequently sealed and stored for 4 – 6 weeks. The sample holder was filled with sample material up to a height of 12 mm and the remaining space in the holder was filled with 8 mm polythene. The latter replaces air in the holder and ensures a flat surface of the sample. This geometry was used for measuring the Volkegem internal standard and for measuring the background (empty sample holder). Each sample, weighing 60 – 80 g, was measured for around 80 hours.

Nuclide	**Photon energy (keV)**	**Activity concentration (Bq kg^{-1} *10^{6})**	**Photon emission rate (s^{-1}*kg^{-1})**
^{133}Ba	81	2.99	1.10
^{57}Co	122	3.00	2.57
^{139}Cer	166	2.99	2.39
^{133}Ba	356	2.99	1.85
^{85}Sr	514	15.00	14.8
^{137}Cs	662	6.11	5.20
^{54}Mn	835	5.93	5.93
^{88}Y	898	14.9	14.0
^{65}Zn	1116	14.8	7.44
^{88}Y	1836	14.9	14.8

Table 2. The multi-nuclide solution QCYB41 (batch#16/1) in terms of photon energy, activity concentration, and yield certified in January 2016 (Eckert and Ziegler, 2016); $m = 2.014 \pm 0.001$g; ρ~1.008 g cm^{-3}. The measurement uncertainty is 2% for all nuclides.

2.2. The efficiency calibration methods

Two materials were used for efficiency calibration: Volkegem loess (De Corte et al., 2007) and the multi-nuclide reference solution QCYB41 (Eckert & Ziegler (Deutsche Akkreditierungsstelle) 2016). The Volkegem sample, originating from a loess deposit in Belgium, has been analysed in several laboratories using different analytical techniques (e.g, ICP-MS, NAA). The QCYK multi-nuclide material is a 0.5 M HCl reference solution with a mass of ~2 g and a density of ~1 g cm^{-3}. It is doped with 20 µm/ml per nuclide (Table 2).

The calibration method associated with the Volkegem sample, henceforth denoted as cal#1, is a direct comparison with the standard material using the equation

$$A_{sample} = \frac{[N/mT]_{sample}}{[N/mT]_{reference}} \times A_{reference}$$

where A is activity concentration (Bq kg^{-1}), N is the net number of counts, T is the count time and m is the mass of the sample. For $A_{reference}$ the values were taken from De Corte et al. (2007) and from the ICP-MS analysis (Geoff Duller, pers. com., June 2017). For values see Table 3.

The method associated with the multi-nuclide reference solution, henceforth denoted as cal#2, uses the equation

$$A = \frac{N}{mTP_{\gamma}\eta}$$

where P_{γ} is the gamma emission probability and η is a practical efficiency that takes account of the energy resolution, the density of the sample, the full-energy efficiency of the detector at that energy, and where necessary, true coincidence summing. In our lab η was approximated through (i) determining the full-energy peak efficiency, (ii) adopting coincidence summing factors from Debertin & Schoetzig (1990) for the energy peaks at 352 keV and 609 keV and, (iii) correcting the low-energy peaks for density. The approximation is based on participating regularly in IAEA-directed interlaboratory comparison studies which allow adjusting the values and, hence, optimise the parameter η.

2.3. Comparing the efficiency calibration methods

The photon peaks with the following energies (keV) were used for the comparison: (i) 46, 63, 352, 609 keV representing ^{226}Ra and ^{238}U, (ii) 238, 338, 911 keV representing ^{232}Th and (iii) 1460 keV from ^{40}K. With the exception of ^{40}K all radioisotopes emitting these energies have short half-lives and are therefore in radioactive equilibrium, that is, they all represent the corresponding parent nuclide with the same activity. Suitable for dose-rate estimation are peaks with the

Laboratory	Analytical technique	n	^{238}U	^{235}U	U	^{226}Ra	^{232}Th	^{40}K	Reference
Ghent	multiple	5	34.5 ± 1.5	1.59 ± 0.09	36.1 ± 1.7	34.1 ± 2.3	42.2 ± 2.5	497 ± 45	De Corte et al. (2007)
Liverpool	γ-spec; IAEA-375	1	38.8 ± 2.1	-	-	-	44.4 ± 0.7	571 ± 13	Abdualhadi et al. (2018)
Aberystwyth	ICP-MS	6	37.8 ± 0.5	-		-	44.3 ± 1.5	543 ± 6	Pers. com., Geoff Duller, June 2017
Dresden	Trans-mission	1	43 ± 5	-	-	42.2 ± 2.8	-	535 ± 56	Degering (2017)
Risø	γ-spec; BL-5, OKA-2 and K_2SO_4	1	37.8 ± 0.7	-	-	42.8 ± 0.2	44.2 ± 0.5	570 ± 5	Murray et al. (2018)
Salzburg	γ-spec; QCYB41	1	38.4 ± 0.7	-	-		40.4 ± 1.5	556 ± 20	This study

Table 3. The Volkegem loess: activity concentrations (Bq kg^{-1}) determined in different laboratories using different analytical techniques; *n*=number of subsamples analysed.

energies 352, 609, 238, 338, 911 and 1460 keV, because they are the least affected by disturbances in the gamma spectrum such as Compton scattering, peak interference or true coincidence summing (see Gilmore 2008 for details). In addition, it is good practice to use several photon peaks for determining the parent activity because some disturbances depend on the sample's average atomic number (Z), chemical composition and density (e.g., Abdualhadi et al. 2018).

Three ways were used for comparing the two methods: (i) for the group of photon peaks representing ^{232}Th or ^{238}U the cal#1 to cal#2 ratio of activity data of each sample was used; (ii) for comparing the activity data obtained from individual photon peaks a plot of cal#1 versus cal#2 was used; (iii) to assess the performance of cal#1 and cal#2, the standard deviation of activities derived from photon peaks representing the corresponding parent nuclide was used.

2.4. Samples

The samples were arbitrarily selected from the pool of existing samples in our laboratory. They originate from central Africa, east and central north America, north and south Europe, central Asia, Mongolia and Arabia and represent, hence, variable geochemical environments and depositional settings. Some samples are inhomogeneous with regard to grain size (composed of clay, silt and sand), others are more or less homogeneous and the sampled environments suggest minor post-depositional disturbances. Exception to this are samples #5 and #81 which are from a carbonate-rich or evaporitic environment.

2.5. Uncertainties and consistency of activity data

The uncertainty of the activity concentrations is dominated by counting statistics, detection efficiency, nuclear decay data and geometry-defined true coincidence summing. For the activities measured here for ca 80 h the uncertainties are 2 – 4% where the one resulting from the cal#2 method is usually around 1% higher than the cal#1 uncertainty. The activity data are consistent if the deviation from unity does not exceed the sum of uncertainties calculated from the square root rule which is typically 4 – 5%.

3. Results

The activity data obtained from the peaks at 338 keV and 911 keV (Fig. 1A) and 46 keV (Fig. 2) are consistent. Deviations from unity that are >5% appear for 238 keV (Fig. 1A and B), 63 keV (Fig. 2), 352 keV and 609 keV (Fig. 3A) and 1460 keV (Fig. 4A). Using the higher cal#1 activity reference value for ^{232}Th as indicated by the ICP-MS result (Table 3) raises the deviation at 911 keV from ~4% to ~9%, at 338 keV from unity to ~5% and reduces the deviation at 238 keV from ~15% to ~12% (Fig. 1B). Changing the cal#1 activity reference value for ^{238}U (again according to the ICP-MS result; Table 3) brings the 352 keV and 609 keV ratios from 8% deviation to unity (Fig. 3B). Changing the cal#1 reference value for ^{40}K (again according to the ICP-MS result; Table 3) reduces the deviation from ~10% to ~3% (Fig. 4). Within each calibration method the deviations are similar for ^{238}U, but not for ^{232}Th: for the mean of 352 and 609 keV the standard deviation is 2-4% and for few samples it is 6-8% for both methods (Fig. 5A) where cal#1 tends to show smaller deviations. For ^{232}Th determined through the mean of 238, 338 and 911 keV the standard deviation of cal#1 is 6-12% and that of cal#2 is 2-6% (Fig. 5B).

4. Discussion

This empirical study looks for consistency between two efficiency calibration methods in order to infer the likelihood of data inaccuracy. Ideally, both methods deliver identical results within a given uncertainty which is typically 4 – 5% for the measurement procedure employed in this study. On the other hand, the two methods are considerably different: cal#2 accounts for nuclear parameters such as emission probability

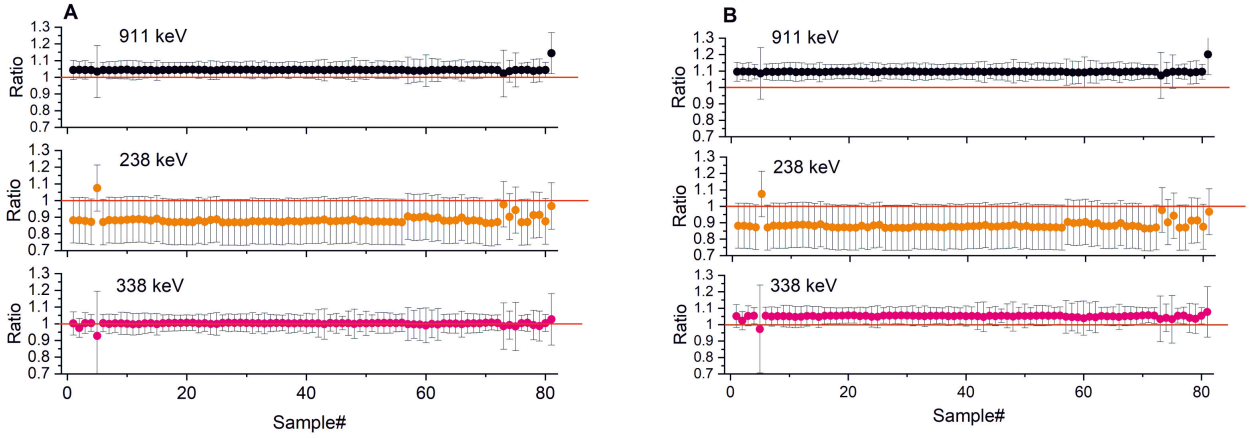

Figure 1. The ratio of activity data obtained from the cal#1 and cal#2 methods plotted versus the sample number for the three photon peaks representing ^{232}Th. Each dot represents a sample's ratio and respective uncertainty. The red line indicates unity. The cal#1 activity reference value is A - 42.2 ± 2.5 Bq kg^{-1} following De Corte et al. (2007) and B - 44.3 ± 1.5 Bq kg^{-1} following Duller (pers. com.; see Table 3). See Section 2.2 for details about the cal#1 and cal#2 methods.

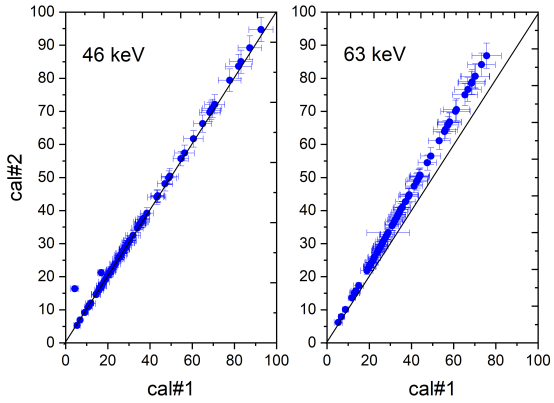

Figure 2. Comparing activity data (Bq kg^{-1}) for two radioisotopes (^{210}Pb: 46 keV, ^{234}Th: 63 keV) of the ^{238}U series derived from the cal#1 and cal#2 methods (for description see Section 2.2).

and detector-specific parameters such as full-energy peak efficiency while cal#1 assumes that these parameters are the same for internal standard and unknown sample. Differences between the results of the methods are therefore expected and these are likely energy- and, eventually, sample-dependent. However, the differences should not exceed the average uncertainty of activity data as long as each method is robust.

For ^{232}Th consistent activity values are obtained when deploying the original Volkegem activity reference value given by De Corte et al. (2007) and when using the peaks at 911 keV and 338 keV (Fig. 1A). For the peak at 238 keV the two methods are not consistent (Fig. 1). This is most probably caused by the cal#1 method as it shows significant deviations for the activities of the ^{232}Th radioisotopes (Fig. 5B). The interference with the ^{214}Pb peak at 242 keV requires manual peak and background analysis of the 238 keV peak in each spectrum, a procedure that we carried out in this study in the cal#2, but not in the cal#1 approach.

For ^{238}U consistent activity values are obtained when raising the original Volkegem activity reference value by ~9% and using the 352 keV and 609 keV energy peaks (Fig. 3A). Even for the peak at 609 keV which is subject to substantial coincidence summing the data are in agreement after raising the value. For the low-energy peaks at 46 keV and 63 keV consistency is not expected owing to the sensitivity of these energies to the sample's Z and density. The apparent consistency at 46 keV (Fig. 2) suggest the influence of external (unsupported) ^{210}Pb which seem to dominate the activities determined and, thus, both calibration methods likely deliver inaccurate ^{210}Pb activities. The same applies to the peak at 63 keV where the inconsistency is more obvious suggesting minor reliability of this energy peak for determining the parent activity. For ^{40}K consistent activity values are obtained when raising the original Volkegem activity reference value by ~9% (Fig. 4).

Thus, this comparative study confirms the original activity reference values (De Corte et al., 2007) for ^{232}Th while for ^{238}U and ^{40}K consistency is achieved when the original value is elevated by ~9%. It confirms the usage of the peaks at 352, 609, 338, 911 and 1460 keV for robustly determining parent activity and, thereby, confirms the well-known: the energy peaks least affected by disturbances (e.g., Compton scattering) are perfectly suitable for direct comparison with the Volkegem and, eventually, other non-certified materials. There is therefore no reason to hypothesise inaccurate activity data resulting from the simple comparison with the Volkegem internal standard.

Photon peaks other than the ones listed above may be used in conjunction with the Volkegem material, but the issue with the 238 keV peak exemplifies the need for comparative studies to assess each peak's suitability. The low-energy peaks at 46, 63 and 93 keV and the one at 186 keV are not suitable for routine analysis owing to their sensitivity to differential

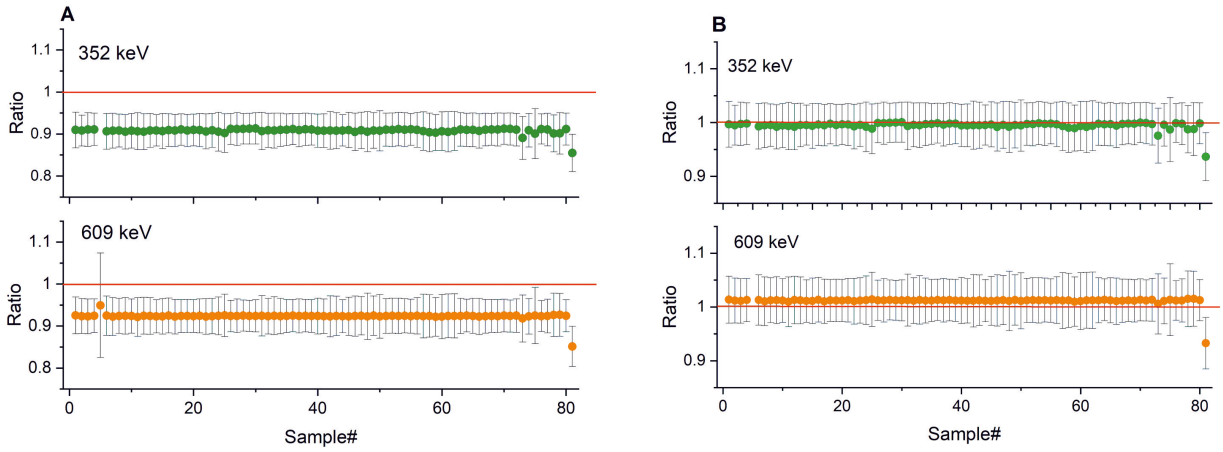

Figure 3. The ratio of activity data obtained from cal#1 and cal#2 for the two photon peaks representing ^{226}Ra and ^{238}U. The red line indicates unity. The cal#1 activity reference value is A - 34.5 ± 1.5 Bq kg^{-1} following De Corte et al. (2007) and B - 37.8 ± 0.5 Bq kg^{-1} following Duller (pers. com.; see Table 3). For description of cal#1 and cal#2 see Section 2.2

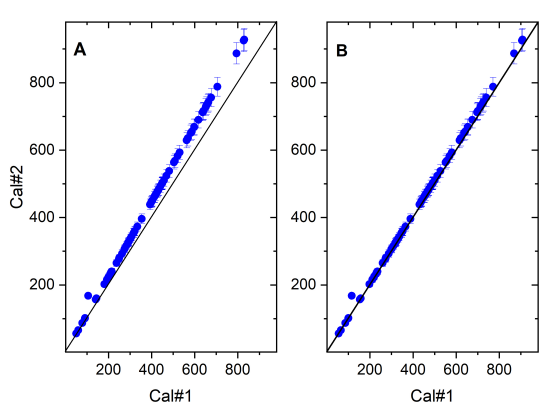

Figure 4. Comparing activity data (Bq kg^{-1}) for ^{40}K. The activity reference value for cal#1 is A - 497 ± 45 Bq kg^{-1} following De Corte et al. (2007) and B - 543 ± 6 Bq kg^{-1} following Duller (pers. com.; see Table 3).

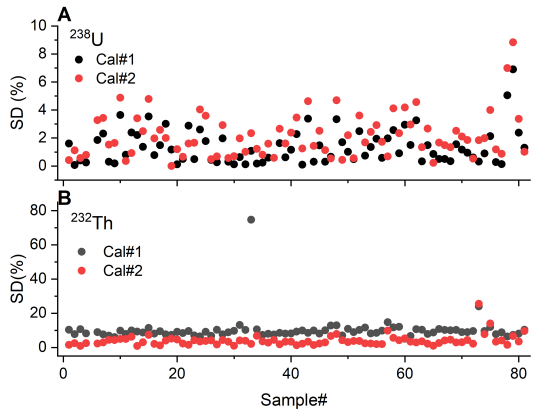

Figure 5. The relative standard deviation (SD) of the mean of the photon peak data used to determine the parent activity. A – SD of 352 keV and 609 keV; B – SD of 238, 338, 911 keV.

self-absorption between unknown sample and standard or to peak interference (Mauz et al., 2021). Nonetheless, these peaks may provide insight into the sample's characteristics and, eventually, prompt additional quantitative analysis regarding the presence of secular disequilibrium (e.g. Abdualhadi et al. 2018).

The results for the ^{232}Th photon peaks are surprising: two of these deliver consistent data straightaway suggesting that the considerable discrepancies revealed in the inter-laboratory comparison do not arise from the Volkegem or other non-certified standard material. A number of other parameters should be screened instead, especially analytical procedures such as measurement geometry, background subtraction and photon-peak selection.

5. Conclusions

We agree with Murray et al. (2015) that the inter-laboratory comparison results for ^{232}Th "*give the greatest cause of concern*" (Murray et al. 2015, p.35). We think that the ~15% difference for ^{40}K is also alarming because the corresponding photon peak is easy to analyse even in low-activity samples and regardless the detector type. Our results show that the choice of the efficiency calibration method generates minor inaccuracies only. We think therefore that the community should be committed to conducting intercomparison studies focusing on gamma-spectrometry. Initially, and for starting the process, individual laboratories may just compare data of a sample of their choice and develop best practice protocols for data analysis. This should be straightforward and may well provide hints to the origin of the discrepancies.

Acknowledgement

BM would like to express her gratitude to Paul Nolan and Peter Appleby (University of Liverpool) for discussing the analysis of a gamma spectrum. We thank David Sanderson for his knowledgeable and insightful review.

References

Abdualhadi, S. A., Mauz, B., Joss, S. D. T., and Nolan, P. *Detecting and quantifying uranium-series disequilibrium in natural samples for dosimetric dating applications*. Radiation Measurements, 114: 25–31, 2018. URL https://doi.org/10.1016/j.radmeas.2018.04.011.

De Corte, F., Vandenberghe, D., Hossain, S. M., De Wispelaere, A., Buylaert, J.-P., and Van den Haute, P. *Preparation and characterization of loess sediment for use as a reference material in the annual radiation dose determination for luminescence dating*. Journal of Radioanalytical and Nuclear Chemistry, 272: 311–319, 2007. doi: 10.1007/s10967-007-0522-5.

Debertin, K. and Schoetzig, U. *Bedeutung von Summationskorrektionen bei der Gammastrahlen-Spektrometrie mit Germaniumdetektoren*. Physikalisch Technische Bundesanstalt (PTB) Report Ra-, 24: 1–55, 1990.

Degering, D. *Test reports 2844.1 and 2844.2*. VKTA – Strahlenschutz, Analytik & Entsorgung Rossendorf e. V., (unpublished), 2017.

Eckert & Ziegler (Deutsche Akkreditierungsstelle). *Calibration certificate for Dept of Physics, Biophysics and Chemistry and Physics of the Materials*. University of Salzburg, unpublished document, 2016.

Gilmore, G. *Practical gamma spectrometry*. Wiley, West Sussex, 2008.

Mauz, B., Appleby, P. G., and Nolan, P. J. *Quantifying Uranium-series disequilibrium in natural samples for dosimetric dating, Part 1: gamma spectrometry*. Geochronology, preprint, 2021. URL https://doi.org/10.5194/gchron-2021-32.

Murray, A., Buylaert, J.-P., and Thiel, C. *A luminescence dating intercomparison based on a Danish beach-ridge sand*. Radiation Measurements, 81: 32–38, 2015. doi: http://dx.doi.org/10.1016/j.radmeas.2015.02.012.

Murray, A., Helsted, L. M., Autzen, M., Jain, M., and Buylaert, J.-P. *Measurement of natural radioactivity: Calibration and performance of a high-resolution gamma spectrometry facility*. Radiation Measurements, 120: 215–220, 2018. URL https://doi.org/10.1016/j.radmeas.2018.04.006.

Reviewer

David Sanderson

Ancient TL

Beta dose rate reduction for the built-in ^{90}Sr/ ^{90}Y sources of Risø TL/OSL automated readers

Emmanuel Osunkwor[1*] and Regina DeWitt[1]

[1] East Carolina University, Department of Physics, Greenville, NC, USA

[*]Corresponding Author: osunkwore17@students.ecu.edu

Received: October 14, 2021; in final form: November 30, 2021

Abstract

Environmental dosimetry requires measuring doses, which are often below the range accessible with the commonly used built-in β-source of Risø TL/OSL readers. Al_2O_3:C Luxel® dosimeters were used to investigate irradiation cross-talk and attenuators as means to reduce the dose rate of the source. Irradiation cross-talk was found to be highly effective in reducing the dose rate but was not reproducible and resulted in dose recovery deviations of up to 80%. Four attenuator materials (PTFE, microscope coverslip glass, wine glass, and ABS plastic) were investigated with regard to their dose reduction capabilities. All materials resulted in good dose recovery results and allow building a standard reference dose response curve. Microscope cover glass reduces the dose rate by a factor of 3 for each 1 mm thickness. The material is transparent and does not have to be removed during measurement and is therefore recommended as attenuator of choice for dose rate reduction.

Keywords: Dose rate reduction, Risø source, Al_2O_3:C, OSL, Attenuators

1. Introduction

Al_2O_3:C dosimeters have become one of the most widely used luminescence dosimeters for environmental dose-rate assessment. The appeal of this dosimeter stems from its high sensitivity to radiation and linear behavior over a wide dose range from µGy to several Gy (Akselrod et al., 1990; Yukihara & McKeever, 2008). Al_2O_3:C has been used in various studies for retrospective dosimetry (McKeever et al., 1995; Bøtter-Jensen et al., 2000; Discher et al., 2021) and measurement of β dose rates to natural sediments (Göksu et al., 1999; Burbidge & Duller, 2003; Kalchgruber et al., 2002; Kalchgruber & Wagner, 2006; Durcan et al., 2015; Smedley et al., 2020). To determine the environmental dose absorbed by the dosimeters during burial, the signal is first measured in the laboratory, followed by irradiation of dosimeters for calibration (Kalchgruber & Wagner, 2006). A common instrument for this measurement and subsequent irradiation is the Risø TL/OSL-DA reader. The reader is often equipped with a 1.48 GBq ^{90}Sr/ ^{90}Y β-source, that delivers a dose rate of the order of 100 mGy/s to a sample when the source is open. Considering that signals from Al_2O_3:C dosimeters are very bright a dose rate of this magnitude can easily saturate the photomultiplier tube (PMT) of the reader after a few seconds of irradiation. The light reaching the PMT can be reduced by using an aperture. Alternatively, on can or correct for the dead time loss that causes saturation, in which case, there is a risk, however, of damaging the PMT. Furthermore, environmental radiation is classified under low level background radiation and dose-rates are typically less than 100 µGy/s (Burbidge & Duller, 2003). In routine environmental beta dose-rate assessment, dosimeters are buried for a period of few weeks to a year (Kalchgruber & Wagner, 2006). The cumulative absorbed dose measured even after a year has been reported to be comparable to the dose obtained after a 1s irradiation from the β-source of the reader (Kalchgruber et al. (2002)). Such short irradiation times are however not recommended since the rotating nature of the irradiation unit introduces a time offset and thus adds uncertainty to the given dose (Markey et al., 1997). Although Al_2O_3:C shows a linear behavior from µGy to few Gy it is not recommended to use larger irradiation times and to extrapolate the dose response to lower doses. Extrapolation is well known to lead to large errors in dose recovery, due to the relatively large impact of

the uncertainty in the intercept fitting parameter.

To reduce the dose rate of the beta source, Burbidge & Duller (2003) used bremsstrahlung radiation that is produced by beta particles from the source in closed position. This option greatly reduced the dose rate to about (0.687 ± 0.003) μGy/s at the dosimeter position and is therefore an effective method for assessing very low doses in the range of 10 μGy to about 1 mGy. However, when the goal is to assess medium doses ~ 1 – 100 mGy, bremsstrahlung requires long exposure times under the closed source; for example, it will take 4 hours to obtain a dose of 10 mGy. Such long exposure times are often not feasible when instrument time is limited. Additionally, this leakage radiation was reported to be maximum at a position different from the position directly under the source (see Fig.1) and asymmetric due to the asymmetric scattering of radiation (Kalchgruber et al., 2002). The radiation affects more than a quarter of all positions on the turntable and additional positions are impacted are impacted by leakage radiation from the alpha source for readers which have an alpha source installed as well. Consequently, it is only practical to irradiate and analyze one or two dosimeters at a time.

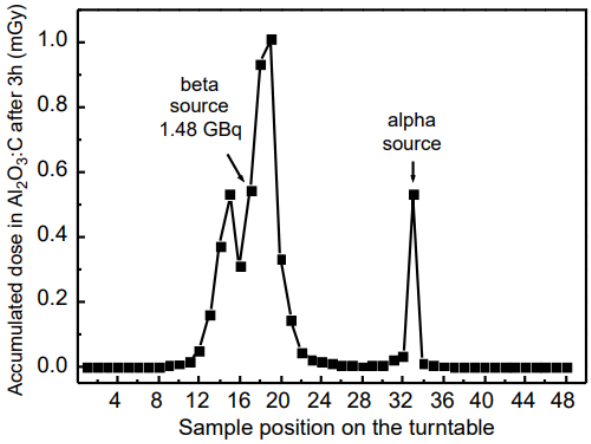

Figure 1. Accumulated dose due to leakage radiation in 3 h at various carousel positions in a Risø TL/OSL-DA-15 reader measured with Al_2O_3:C dosimeters, with both beta and alpha sources installed. The position underneath the beta source indicated on the plot is not the position of maximum dose. The position under the alpha source is also a hotspot as indicated on the plot (Fig. 4. from Kalchgruber et al. (2002))

Other options offered by the manufacturer include purchasing a second, weaker source or the reduction of dose rate by increasing source-sample distance using a separately sold dose rate kit. The kit consist of an aluminum filter, a brass ring and an aluminum spacer that can reduce the dose rate by a factor of ~ 10. However, this dose rate kit requires removing the built-in source from the irradiator for installation. The radiation safety regulations in many institutions require that a radiation safety officer perform this kind of procedure and thus might not be feasible if inserting or removing the kit is required several times a week.

A third option is the use of irradiation cross-talk. Irradiation cross-talk is defined as radiation exposure to dosimeters in the vicinity but not directly under the irradiation source, when the source is open. This effect has been investigated by various authors for quartz and Al_2O_3:C dosimeters and has been shown to be in the range of 0.006 – 0.25 % of the direct dose rate, depending on the specific reader and the irradiated sample (Bøtter-Jensen et al., 2000; Kalchgruber et al., 2002; Bray et al., 2002; Thomsen et al., 2006). Yet another option for dose rate reduction, which to our knowledge has not been investigated in detail, involves placing an attenuator directly on top of the dosimeter.

This paper investigates the latter two options of reducing the dose rate of the built-in β-source of the Risø reader: i) irradiation crosstalk and ii) attenuators. The major limitation with the absorber is the small distance between the bottom of the cup and the lid. This distance which can range from ~ 1.8 – 2.5 mm is reader specific. To this end, different materials of different thicknesses were investigated to arrive at the best option for the attenuator. The overall goal is to build a reference dose response curve that can be used for dose assessment of dosimeters buried in sediment for several weeks to a year.

2. Materials and methods

2.1. Dosimeters

The dosimeters used in this work are the Al_2O_3:C Luxel® dosimetry tapes cut into 6.0 mm diameter round pieces using a hole puncher (Fig.2). The Luxel® tapes are produced by Landauer Inc. and consist of 20 - 90 µm Al2O3:C grains sandwiched between two polyester sheets, resulting in a thickness of about 0.3 mm (Akselrod et al., 2000; Bøtter-Jensen et al., 2003). Prior to use, the dosimeters were bleached for 8-12 hours with light from a halogen lamp filtered with a Schott FSQ-GG-495 colored glass long-pass filter (thickness 3.0 mm) as recommended by Sawakuchi et al. (2008) to remove any background signal accumulated during storage and transport, if applicable. Between irradiation and measurement, the dosimeters were handled in a dark room with subdued red light for visibility and to prevent any bright light from resetting the dosimeters and placed in stainless steel cups.

2.2. Attenuators

Attenuators of different materials were investigated in this work as a way of reducing the dose rate of the β-source of the Risø reader. Four different attenuator materials were tested for their effect on the dose rate:

- a 10 mm diameter disk of clear glass, type “Libbey midtown white wine glass” produced by LIBBEY GLASS. The thickness of the disk is 1.4 mm and its density is 2.27 g/cm^3.
- two sets of round coverslips (microscope cover glass, density 2.42 g/cm^3), 12 mm diameter and 8 mm diameter respectively. Six of the 12 mm coverslips were stacked to get a thickness of 1.4 mm (including the

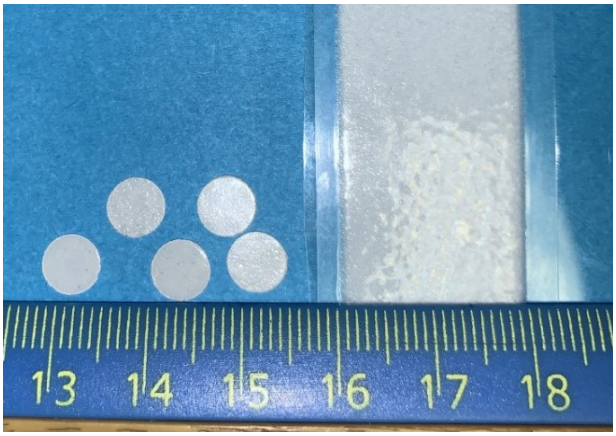

Figure 2. OSL Luxel® round punch-out and tape. The round punch-out was obtained by using a hole punch on the tape. The thickness of the dosimeter is 0.3 mm and diameter is 6.0 mm.

transparent tape used to hold the stack together). The actual thickness of the stack without the tape is 1.2 mm. Similarly, ten 8 mm coverslips were stacked to get a thickness of 1.9 mm and held together by glass glue. The use of a tape was not feasible in this case because of the smaller diameter. The coverslips are produced by BIPEE, China.

- Acrylonitrile-Butadiene-Styrene (ABS) (density: 1.17 g/cm^3) disks, 8.2 mm diameter with a recess of diameter 6.3 mm and depth 0.3 mm to hold the Luxel dosimeter (Fig. 5c). The thickness of the disk at the rim is 1.8 mm and 1.5 mm above the dosimeter in the recess. The material is produced and sold in the form of rods by US Plastic Corp®. Lima, OH.

- Teflon® (natural virgin PTFE, density 2.20 g/cm^3) disks with 8.2 mm diameter and thicknesses of 1.4 mm and 1.9 mm respectively. Teflon is produced in the form of rods by ePlastic®, San Diego, CA.

Photos of all the attenuators are shown in Fig. 4. The wine glass disk and the 12 mm diameter microscope coverslip glass stack were placed on top of the sample cup as shown in Fig. 3 (left) and 5a, leaving a small air gap of ∼0.4 mm between attenuator and dosimeter. The maximum total height of the combination is about 2.3 mm, which is the allowable distance between the bottom of the cup and the lid for this specific model of Risø reader. The 8-mm cover glass, and the ABS and Teflon disks were in direct contact with the dosimeters (Figs. 3b and 5b, c).

2.3. Irradiation and readout equipment

All measurements were performed with a Risø TL/OSL-DA-20 automated reader produced by DTU Physics, Denmark. The reader is equipped with a built-in nominal 1.48 GBq ^{90}Sr/ ^{90}Y source with a beryllium window located between the irradiator and the measurement chamber, which acts as a vacuum interface for the measurement chamber (Markey et al., 1997). The dose rate to Al_2O_3:C Luxel® in the position directly under the source is 72.7 mGy/s (±3%). Green LEDs (at 525 nm, 68 mW/cm^2) were chosen for optical stimulation of the dosimeters. Due to the high sensitivity of Al_2O_3:C, a 10 mm aperture was used in combination with 7.5 mm thick U-340 filters (transmission 340 ± 40 nm) in front of the PMT to reduce the possibility of over-saturation. The dosimeters were placed on stainless steel cups mounted on a turntable with 48 sample positions. Only every 5th position was used to prevent radiation crosstalk from affecting the dosimeters.

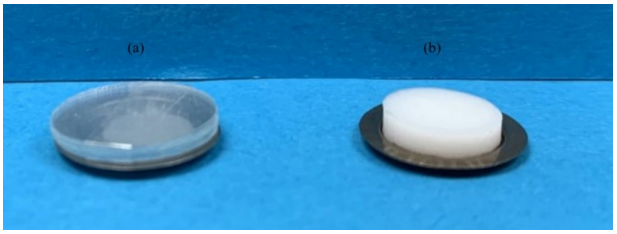

Figure 3. Absorber and sample cup combinations: (a) 12 mm diameter microscope coverslip glass stack on top of the sample cup with a dosimeter and (b) 1.9 mm PTFE disk placed inside the sample cup directly on top of the dosimeter.

2.4. General read-out procedure

The measurement procedure is as follows. Irradiation steps varied with experiment and are described in detail below.

1. Irradiation with beta source:
   (a) indirect irradiation using cross talk (see section 3.1)
   (b) direct irradiation, with or without attenuator (see section 3.2)
2. Remove attenuator, where applicable
3. OSL with green diodes for 500 s at 30°C, record one data point every 1s; signal S
4. Test dose irradiation
   (a) indirect irradiation using cross talk (see section 3.1)
   (b) direct irradiation, without attenuator (see section 3.2)
5. OSL with green diodes for 500 s at 30°C, record one data point every 1s; signal S_T

The test dose accounts for variation in parameters such as dosimeter sensitivity, dosimeter mass, and equipment sensitivity (Murray & Wintle, 2000; Yukihara et al., 2005). OSL intensity was obtained from the integrated signal of the first 10 s of stimulation, and the background from the last 10 s of stimulation. The test-dose corrected signal S/S_T and its uncertainty is calculated for each dosimeter. Each dosimeter is only used once.

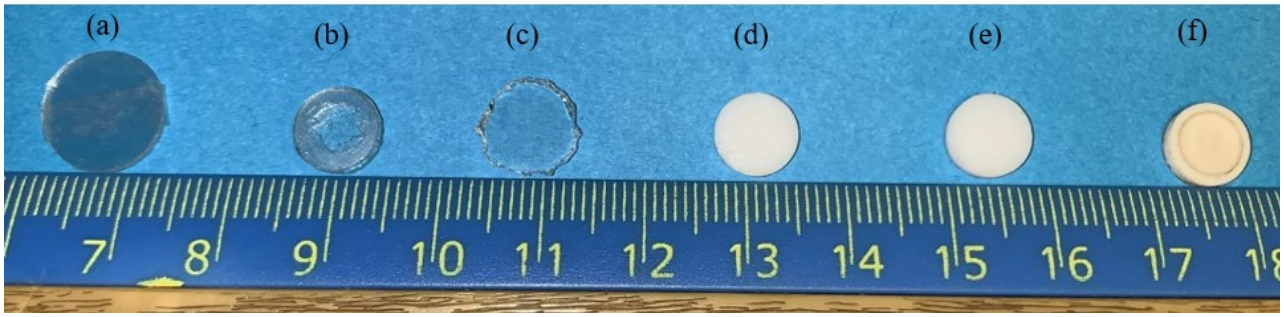

Figure 4. Absorber materials used in this study. From the left, (a) microscope coverslip glass stack (diameter = 12 mm, thickness = 1.4 mm), (b) microscope coverslip glass stack (diameter = 8 mm, thickness = 1.9 mm), (c) wine glass disk (diameter = 10 mm, thickness = 1.4 mm), (d) PTFE disk (diameter = 8.2 mm, thickness = 1.4 mm), (e) PTFE disk (diameter = 8.2 mm, thickness = 1.9 mm), and (f) ABS disk (diameter = 8.2 mm, thickness = 1.8 mm, also showing the 0.3 mm recess for the dosimeter).

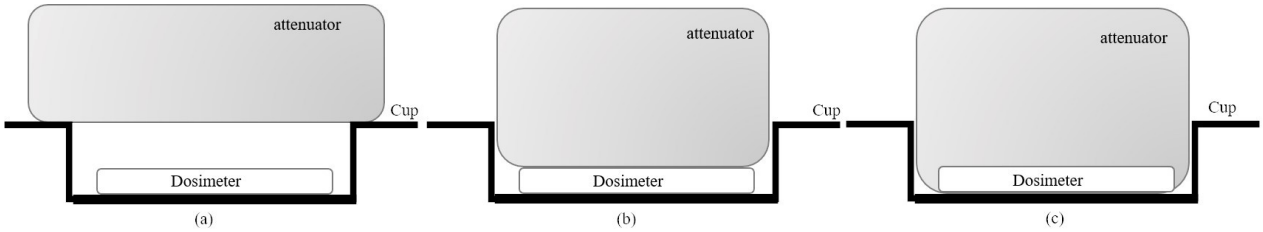

Figure 5. Three Configurations of sample cup-dosimeter-attenuator combination. Configuration (a) was used for the 12mm diameter coverslip glass stacks and the 10 mm diameter wine glass, since their diameters exceed the 8.3 mm diameter of the recess in the sample cup. Configuration (b) was used for the PTFE disks and the 8 mm diameter coverslip stack, and (c) was used for the ABS disk with recess.

3. Results

3.1. Indirect irradiation with radiation cross-talk

3.1.1 Estimation of cross-talk dose-rate

In our first set of experiments, we investigated the use of next-position irradiation ("cross-talk") as described by Kalchgruber et al. (2002), as a method of extending the range of the dose-response curve to low doses in the μGy region. No attenuators were used for this set of experiments. The position adjacent to each dosimeter was irradiated with specific doses ranging from 200 – 3000 s (3 dosimeters per dose point) and subsequently implementing the readout procedure described in section 2.4 using a test dose of 250 s, also via cross-talk. A linear fit was used to determine the resulting dose response. In a second step, 3 separate dosimeters were irradiated directly for 1 s. Their 250 s indirect test-dose corrected signal was compared to the dose response. The cross-talk irradiation time equivalent to 1 s direct irradiation was determined to be 2078 s (±8%) (see Fig. 6). In other words, the cross-talk dose rate of the Risø reader is about 0.05% that of direct irradiation.

3.1.2 Effect of dosimeter positioning on reproducibility

The purpose of dose-response curves is generally for dose recovery. For environmental dosimetry the dosimeters are irradiated during burial and the test-dose corrected signal is then compared to an established dose response curve to determine the absorbed dose. Radiation cross-talk changes considerably between adjacent positions (Fig. 1). Dosimeters buried in sediments and then placed in the reader for measurement might not all be in exact same position on the cup. There is also the possibility of random shift in the position of the dosimeter in the cup during measurement procedure. To test the impact of positioning on our results, 3 dosimeters were irradiated with cross-talk doses of 250 s, 450 s and 800 s

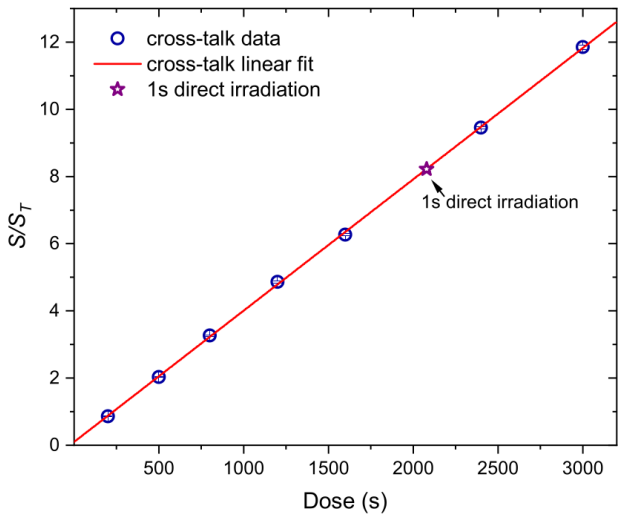

Figure 6. Reference dose–response curve of Al_2O_3:C dosimeter built up with the β-source of the Risø reader (Risø TL/OSL-DA-20) using cross-talk for indirect irradiation. The red line indicates the linear fit of the irradiation cross-talk S/S_T vs. equivalent dose data while the purple star symbol represents the 1s direct irradiation data.

Protocol	Known Dose (s)	Recovered Dose (s)	Recovery Ratio
Dosimeter "stayed in reader" between irradiation and measurement	250	254 (± 4%)	1.016
	450	455 (± 2%)	1.011
	800	802 (± 2%)	1.003
Dosimeter removed, stored for 4h between irradiation and measurement	250	107 (± 9%)	0.428
	450	585 (± 2%)	1.300
	800	1483 (± 1%)	1.854

Table 1. Accuracy of dose recovery when dosimeters remain in the reader after irradiation, versus brief removal and re-insertion of dosimeters.

respectively. The three dosimeters were read immediately without opening the reader using the readout procedure. Another set of 3 dosimeters, used to mimic external irradiation, were removed from the reader subsequent to irradiation and stored for 4 hours in a dark room to simulate transport and storage, before they were read using the readout procedure. The doses recovered from these dosimeters using the dose response curve were compared to the known doses and results are given in Table 1

Table 1 shows that the measurement procedure is suitable for recovering doses with a precision of better than 2%, and that random shifts during measurement have little impact on the results. For the dosimeters that were removed from the reader and stored for 4 hours, measured doses show large deviations up to 85%. Yukihara & McKeever (2006), reported that UV emission from Al_2O_3:C increases with the time elapsed between irradiation and measurement. In order to remove the effect of wait time, a similar test, but with an equal wait time of 5 min for all dosimeters was conducted. In this test, 10 dosimeters were irradiated with radiation cross-talk for 500 s and the signal was measured using the readout procedure, including test-dose application via cross-talk. For 5 out of the 10 dosimeters, the reader was not opened, but there was a 5 min delay between irradiation and measurement. The other set of 5 dosimeters was irradiated in the reader, removed and stored for 5 minutes, before signal measurement and test-dose correction. For each of the two sets, consisting of 5 dosimeters each, the average recovered dose and its standard error was calculated. The relative standard error for dosimeters removed from the reader is about 19% compared to 0.6% when there was no removal of the dosimeter, again showing that removal of dosimeters from the reader has a significant impact on the reproducibility and accuracy of dose recovery.

3.1.3 Summary of cross-talk results

Table 1 shows that our recovered doses differ from the known dose by about 30 – 85% when the dosimeter is removed from the reader and stored for 4 hours before measurement, compared to 2 – 4% for dosimeters that remained in reader throughout irradiation and measurement with no wait time in between. For the latter, it is impossible to isolate what part of this deviation is due to removal of the dosimeters and what part is due to increase in UV signal with time after irradiation. According to Yukihara & McKeever (2006), the UV signal increase after 4 hours is about 33%. While this can explain some of the deviation seen, it is important to mention that for the 250 s irradiation, the recovered dose was about 57% less than the known dose. This cannot be explained by the UV effect. Additionally, the test by Yukihara & McKeever (2006) that showed the increase of UV signal with measurement time after irradiation was performed with 20 Gy. We do not know if this effect also occurs for very low doses like those measured here and to what extent. Furthermore, our second test eliminated effects of wait-time, but it also showed poor reproducibility when the dosimeters were removed, further indicating that removal of the dosimeter introduces some variability to the result

3.2. Dose rate reduction using attenuators

In a second set of experiments the dose-rate of the source was reduced by placing the absorber materials described in section 2.2 between source and dosimeter. For this set of experiments direct irradiation was used as opposed to the cross-talk used above. Unless otherwise noted, the attenuators used for this investigation are the 1.9 mm PTFE disk, 1.2 mm microscope coverslip glass stack, 1.4 mm wine glass disk and the 1.8 mm ABS plastic disk.

3.2.1 Dose rate reduction factor and reproducibility

To measure the amount by which the attenuator reduces the dose rate, i.e. the "dose rate reduction factor," a dosimeter was exposed to a fixed dose of 10 s without the attenuator and then the readout procedure as described in section 2.4 was performed with a test-dose of 4 s (given without the attenuator) to obtain (S_1/S_T). In a second step, the same dosimeter was irradiated with the attenuator inserted for (S_2/S_T). The ratio $k = (S_1/S_T)/(S_2/S_T)$ corresponds to the *dose rate reduction factor* of a specific attenuator used, where S_1 represents the signal from exposure without the attenuator ma-

Attenuator description	k	$k_t(mm^{-1})$
10 mm diameter, 1.4 mm thick Wine Glass disk	4.11 ± 0.04	2.94 ± 0.04
12 mm diameter, 1.2 mm thick Microscope Coverslip stack	3.61 ± 0.03	3.02 ± 0.04
8.2 mm diameter, 1.4 mm thick PTFE disk	3.34 ± 0.04	2.39 ± 0.03
8.2 mm diameter, 1.5 mm thick ABS plastic disk	2.07 ± 0.04	1.38 ± 0.03
8.2 mm diameter, 1.9 mm thick PTFE disk	5.33 ± 0.07	2.81 ± 0.04
8 mm diameter, 1.9 mm thick Microscope Coverslip stack	5.97 ± 0.10	3.14 ± 0.06

Table 2. Dose rate reduction factors k for the absorber materials investigated. The mean was calculated from 6 dosimeters per attenuator material, the uncertainties represent the standard error. k_t is the dose reduction factor per thickness

terial, where S_1 represents the signal from exposure without the attenuator and S_2 represents the signal from exposure with the attenuator. The results for the various attenuators is presented in Table 2. For easier comparison the reduction factor per 1 mm thickness, k_t is listed as well

To test reproducibility in absorber placement, for each absorber material 10 dosimeters were irradiated for 10 s. The same absorber stack was used in each case to eliminate possible variation between stacks of the same material. The test dose corrected signals, normalized to the average value for each material are presented in Fig 7. Table 3 lists relative standard deviations for all materials, including experiments without absorber and results for an experiment with 10 different coverslip stacks.

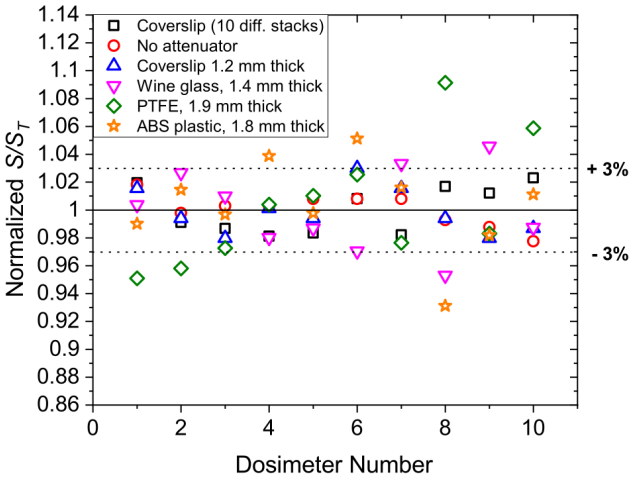

Figure 7. Absorber reproducibility. The same absorber stack was used for 10 dosimeters per material. Test dose corrected signals were normalized to the average value for each material. For comparison, data obtained without absorber and data obtained with 10 different coverslip stacks are shown as well. The normalization line (bold line) and the ±3% spread from the mean lines (dotted lines) are also indicated

Attenuator description	$\frac{\sigma}{\mu}(\%)$
PTFE, 1.9 mm	1.4
Coverslip 1.2mm thick	0.6
Wine glass, 1.4 mm	0.9
ABS plastic, 1.8 mm	1.0
No attenuator	0.4
Coverslip (10 different stacks)	0.5

Table 3. Absorber reproducibility. Relative standard deviations for 10 dosimeters per material. Data obtained without absorber and data obtained with 10 different coverslip stacks are shown as well.

3.2.2 Dose response/Calibration curve and dose recovery

The overall goal of this study is to use the built-in source of the Risø reader to build a dose response that will be used as reference curve for externally irradiated dosimeters. Dose response curves for the different attenuators were built, by exposing three dosimeters per given dose to 10 different doses in the range 1 – 100 s (with attenuators). The actual dose given to each dosimeter will depend on the attenuator used. Attenuators were removed after irradiation and before measurement, since some of the attenuators are opaque. Dose responses for uncorrected and test-dose corrected signals are shown in Fig. 8. Yukihara et al. (2005) and Akselrod et al. (2000), reported linearity only for the uncorrected dose response in this dose range. In our case, both responses are linear in this dose range. Although, the corrected dose response shows a better linearity compared to the uncorrected dose response.

The accuracy in dose determination using the dose response curves in Fig. 8 was assessed by giving known doses to 4 dosimeters each (with the attenuator in place), then measuring the dose as if the dosimeters had absorbed an unknown burial dose. Doses were recovered based on S/S_T values and also the uncorrected S values. The recovered dose is then compared to the known dose using dose recovery ratio. The dose recovery results are presented in Table 4.

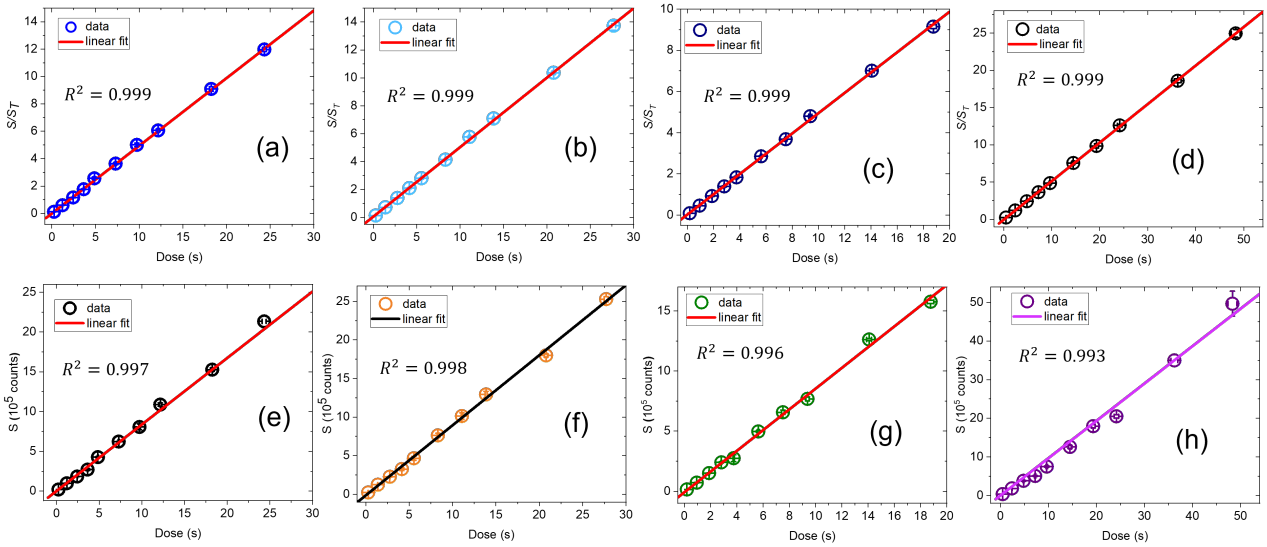

Figure 8. Test dose corrected (upper row) and uncorrected (lower row) dose responses of Al_2O_3:C irradiated with wine glass attenuator (a and e), microscope coverslip glass (b and f) PTFE (c and g) and ABS (d and h). Each data point represents the average and standard error for 3 dosimeters.The adjusted R^2 is also represented to show the goodness of the fit

Attenuator	**Known Dose (s)**	**test-dose corrected**		**uncorrected**	
		Recovered dose (s)	**Recovery Ratio**	**Recovered dose (s)**	**Recovery Ratio**
PTFE	8	8.30 ± 0.06	1.04	7.83 ± 0.10	0.98
	17	17.97 ± 0.12	1.06	17.57 ± 0.23	1.03
	43	44.84 ± 0.28	1.04	40.62 ± 0.53	0.95
	77	81.59 ± 0.51	1.06	78.07 ± 1.01	1.01
Coverslip glass	8	8.18 ± 0.05	1.02	7.50 ± 0.08	0.94
	17	17.22 ± 0.10	1.01	15.62 ± 0.16	0.92
	43	44.36 ± 0.25	1.03	44.16 ± 0.45	1.03
	77	73.81 ± 0.42	0.96	68.87 ± 0.70	0.89
ABS plastic	8	7.88 ± 0.03	0.99	7.14 ± 0.18	0.89
	17	16.90 ± 0.07	0.99	15.20 ± 0.38	0.89
	43	42.02 ± 0.16	0.98	38.88 ± 0.96	0.90
	77	76.35 ± 0.29	0.99	78.64 ± 1.95	1.02
Wine glass	8	7.65 ± 0.05	0.96	6.50 ± 0.078	0.81
	17	16.63 ± 0.10	0.98	15.64 ± 0.16	0.92
	43	42.91 ± 0.24	1.00	44.52 ± 0.46	1.04
	77	74.95 ± 0.43	0.97	67.87 ± 0.69	0.88

Table 4. Summary of dose recovery for irradiation with attenuator. Average recovery ratios for the test-dose corrected data are (1.05 ± 0.01)for PTFE, (1.01 ± 0.02) for coverslip glass, (1.01 ± 0.02) for ABS, and (0.98 ± 0.01) for wine glass.

The goal is to compare externally irradiated dosimeters with the calibration curves. It was therefore imperative to test if calibration curves built with attenuators can be used to recover doses administered without an attenuator. 12 dosimeters were irradiated without attenuator to assess if the attenuator itself influences the dose recovery. It is important to note that the test dose in the readout procedure must be the same as the test dose in the readout procedure used to build the dose response curve. Using the known dose reduction factors (see Table 2) and the test-dose corrected dose response curves (Fig. 8), measured and given doses were compared (Table 5).

Known Dose (s)	PTFE		coverslip glass		wine glass		ABS plastic	
	Recovered dose (s)	Recovery ratio	Recovered dose (s)	Recovery ratio	Recovered dose (s)	Recovery ratio	Recovered dose (s)	Recovery ratio
1	1.00 ± 0.02	1.00	0.95 ± 0.02	0.95	0.97 ± 0.02	0.97	0.97 ± 0.06	0.97
2	2.08 ± 0.04	1.04	1.98 ± 0.04	0.99	2.03 ± 0.03	1.02	2.01 ± 0.13	1.01
3	3.20 ± 0.06	1.07	3.05 ± 0.06	1.02	3.12 ± 0.05	1.04	3.1 ± 0.2	1.03
4	4.22 ± 0.07	1.06	4.02 ± 0.08	1.01	4.12 ± 0.07	1.03	4.1 ± 0.3	1.02
5	5.33 ± 0.09	1.07	5.07 ± 0.10	1.01	5.19 ± 0.08	1.04	5.15 ± 0.33	1.03
6	6.26 ± 0.11	1.04	5.96 ± 0.12	0.99	6.10 ± 0.10	1.02	6.06 ± 0.38	1.01
7	7.41 ± 0.13	1.06	7.04 ± 0.14	1.01	7.22 ± 0.12	1.03	7.17 ± 0.45	1.02
8	8.45 ± 0.15	1.06	8.03 ± 0.16	1.00	8.23 ± 0.13	1.03	8.17 ± 0.52	1.02
9	9.76 ± 0.17	1.08	9.28 ± 0.18	1.03	9.51 ± 0.15	1.06	9.44 ± 0.60	1.05
10	10.63 ± 0.19	1.06	10.11 ± 0.20	1.01	10.36 ± 0.17	1.04	10.29 ± 0.65	1.03
11	11.74 ± 0.21	1.07	11.16 ± 0.22	1.01	11.44 ± 0.18	1.04	11.35 ± 0.72	1.03
12	12.67 ± 0.22	1.06	12.05 ± 0.24	1.00	12.35 ± 0.20	1.03	12.26 ± 0.78	1.02

Table 5. Dose recovery results for dosimeters irradiated without attenuator using the dose-response curves in Fig 8, produced from the S/ST data for irradiation with attenuators. The average recovery ratios are (1.05 ± 0.01) for PTFE, (1.00 ± 0.01) for coverslip glass, (1.03 ± 0.02) for wine glass, and (1.02 ± 0.01) for ABS plastic.

4. Discussion

4.1. Dose rate reduction using irradiation cross-talk

The irradiation cross-talk on the position adjacent to the irradiated position as measured here is about 0.05% of the direct dose. This is a little higher than the 0.04% reported by Kalchgruber et al. (2002) for Al_2O_3:C dosimeters and 8 times higher than the 0.006% reported by Bray et al. (2002) for quartz discs. But it is about 3 times lower than the 0.17% reported by Bøtter-Jensen et al. (2000) for quartz coarse grain. This result confirms previous observation by Kalchgruber et al. (2002) that values of cross-talk depend on the individual reader, the sample holder and the dosimeter material used.

Dose recovery tests resulted in excellent agreement between given and measured dose, when the reader remained closed between irradiation and measurement (Table 1). However, Table 1 also illustrates that a reference dose response built with irradiation cross-talk is not suitable for externally irradiated dosimeters. When dosimeters are removed from the reader between irradiation and measurement, recovered doses deviate 50-80% from the expected values. Recovered doses were well below and also well above the expected values.

This high variability in measurement response is suspected to be partly due to the increase in UV luminescence signal with time of measurement after irradiation that was reported by Yukihara & McKeever (2006), due to the 4-hour wait period before the dosimeter was read, which was done to simulate external exposure of the dosimeters. However, even this effect doesn't fully explain the huge deviation observed as can be seen from the the 19% compared to 0.6% reproducibility observed for the case where the dosimeters were taken out of the reader before measurement compared to when they were not even when the wait time before measurement were the same. Similar variation has been reported by Vargas (2011). She reported a 9% relative standard deviation for a reproducibility test on a single dosimeter that underwent twelve 1.26 Gy irradiation/measurement cycles when the reader is opened, and the dosimeter is exposed to room light from a weak red bulb between irradiation and measurement. Our result for a similar test using 10 dosimeters yielded a reproducibility of 1%. Vargas also reported high variability for a fading test where the dosimeter was taken out of the reader and kept in a dark case for a period before measurement. She concluded that this effect is due to change in the position of the dosimeter on the cup from one irradiation-measurement cycle to another (Vargas, 2011).

It can be argued that in the case of cross-talk, where scattered radiation is used, the dose has a significant dependence on the exact position of the dosimeter in the sample holder. We therefore recommend that irradiation crosstalk, when considered as an option for dose rate reduction, should be tested for reproducibility and dose recoverability first.

4.2. Dose rate reduction using attenuators

Dose rate reduction with attenuators depends as expected on the density and thickness of the material (Table 2). The microscope coverslip glass stack provides the highest dose rate reduction per thickness at a factor of 3 per mm, followed by the wine glass, then the PTFE. The lowest dose rate reduction per thickness is that of the ABS rod which also has the lowest density among the materials investigated. The microscope coverslips and wine glass have the additional advantage of being transparent compared to the PTFE and ABS disks that are opaque. A transparent attenuator will

allow OSL measurements to be conducted without opening the reader to remove the attenuator before measurement. i.e., measurement will be automatic, requiring no user intervention until completion. Additionally, the microscope coverslip glass is the cheapest material investigated (US$10 for a pack of 100).

Reproducibility test for all attenuators presented in Fig.7. shows that 83% of the S/S_T values are within $\pm$ 3% of the mean. The overall relative standard error of the distribution is 0.5%. Yukihara et al. (2005) reported 0.7% for Luxel® dosimeters, and Burbidge & Duller (2003) reported 2.1% for Al_2O_3:C chips. This proves that the use of the attenuator doesn't introduce any substantial uncertainty to the measurement process. The relative standard error when a single coverslip stack was used for 10 dosimeters and when 10 different coverslip stacks were used are 0.6% and 0.5% respectively. The average thickness of the 10 coverslip stacks was calculated to be (1.40 $\pm$ 0.02) mm. This indicates that the coverslip stacks exhibit uniform response, even though there might be a slight nonuniformity in the glue used to bind the slips into a stack.

Attenuators allowed building a dose response for lower doses than usually accessible with the most commonly used built-in source. Dose response of Al_2O_3:C dosimeters is more linear and accurate for all attenuator materials when test-dose corrected signals were used compared to when the uncorrected signal was used, as evident from the dose recovery result in Tables 4 and 5. The results in Table 4 indicate that on average, the dose response curve based on the test-dose normalized signal S/S_T yields better dose recovery results than that based on the uncorrected signal S. On average, the dose recovery ratios of doses recovered using S/S_T data is 1.00 ± 0.01 with a maximum of 1.05 $\pm$ 0.01 (for PTFE) compared to 0.94 $\pm$ 0.02 with a maximum of 0.91 $\pm$ 0.05 (for wine glass) for the uncorrected signals. Dose responses from S/S_T data have a slightly higher adjusted R^2 value (0.999) than those of the S data (0.993 – 0.998). Additionally, the use of a test-dose for Al_2O_3:C Luxel® corrects for sensitivity variations between dosimeters, when they are punched out from the same Luxel® strip. Dose recovery from direct irradiation, yielded promising results as well. A higher deviation was generally seen for the PTFE attenuator. On average, the dose recovery ratio for the direct irradiation are 1.05 $\pm$ 0.01 for PTFE, 1.00 $\pm$ 0.01 for microscope coverslip, 1.03 $\pm$ 0.01 for wine glass, and 1.02 $\pm$ 0.01 for ABS plastic.

5. Conclusion

Irradiation crosstalk and attenuators were investigated as methods for reducing the dose rate of the built-in β-source of the Risø TL/OSL reader. For the Risø TL/OSL system used in this study, the irradiation crosstalk dose rate is about 0.05% of the value for direct irradiation. While, it was possible to extend the dose range to lower doses, dose recovery tests for dosimeters removed and re-inserted in the reader resulted in deviations of 50 – 80%. One possible explanation was attributed to an increase in UV luminescence with measurement time after irradiation. Another possible reason for the large deviations is a change in the position of the dosimeter on the cup during handling of the carousel which led to the conclusion that response to cross-talk irradiation might be sensitive to dosimeter position. However, more tests need to be performed to quantify the positional dependence of cross-talk irradiation.

The use of low-cost attenuator materials, though limited in thickness, provides a cheap and reliable alternative for dose rate reduction for the Risø TL/OSL reader. Four attenuator materials were investigated: PTFE, microscope coverslip glass, wine glass and ABS plastic. All materials resulted in good dose recovery results and allowed building a standard reference dose response. Microscope cover glass reduces the dose rate by a factor of 3 for each 1 mm thickness. The material is transparent and does not have to be removed during measurement and is therefore recommended as attenuator of choice for dose rate reduction.

Acknowledgments

The authors would like to thank Dr. Kristina Thomsen for her detailed review and for helpful suggestions that improved the clarity of the manuscript.

References

Akselrod, M., Kortov, V., Kravetsky, D., and Gotlib, V. *Highly sensitive thermoluminescent anion-defective alpha-Al203: C single crystal detectors*. Radiation Protection Dosimetry, 32(1): 15–20, 1990.

Akselrod, M., Larsen, N. A., and McKeever, S. *A procedure for the distinction between static and dynamic radiation exposures of personal radiation badges using pulsed optically stimulated luminescence*. Radiation measurements, 32(3): 215–225, 2000.

Bøtter-Jensen, L., Bulur, E., Duller, G., and Murray, A. *Advances in luminescence instrument systems*. Radiation Measurements, 32(5-6): 523–528, 2000.

Bøtter-Jensen, L., McKeever, S. W., and Wintle, A. G. *Optically stimulated luminescence dosimetry*. Elsevier, 2003.

Bray, H., Bailey, R., and Stokes, S. *Quantification of cross-irradiation and cross-illumination using a Risø TL/OSL DA-15 reader*. Radiation Measurements, 35(3): 275–280, 2002.

Burbidge, C. I. and Duller, G. *Combined gamma and beta dosimetry, using Al2O3: C, for in situ measurements on a sequence of archaeological deposits*. Radiation Measurements, 37(4-5): 285–291, 2003.

Discher, M., Woda, C., Ekendahl, D., Rojas-Palma, C., and Steinhäusler, F. *Evaluation of physical retrospective dosimetry methods in a realistic accident scenario: Results of a field test*. Radiation Measurements, 142: 106544, 2021.

Durcan, J. A., King, G. E., and Duller, G. A. *DRAC: Dose Rate and Age Calculator for trapped charge dating*. Quaternary Geochronology, 28: 54–61, 2015.

Göksu, H. Y., Bulur, E., and Wahl, W. *Beta dosimetry using thin layer a-Al2O3: C TL detectors*. Radiation protection dosimetry, 84(1-4): 451–455, 1999.

Kalchgruber, R. and Wagner, G. *Separate assessment of natural beta and gamma dose-rates with TL from α-Al2O3: C single-crystal chips*. Radiation measurements, 41(2): 154–162, 2006.

Kalchgruber, R., Göksu, H., Hochhäuser, E., and Wagner, G. *Monitoring environmental dose rate using Risø TL/OSL readers with built-in sources: recommendations for users*. Radiation measurements, 35(6): 585–590, 2002.

Markey, B., Bøtter-Jensen, L., and Duller, G. *A new flexible system for measuring thermally and optically stimulated luminescence*. Radiation Measurements, 27(2): 83–89, 1997.

McKeever, S. W., Moscovitch, M., and Townsend, P. D. *Thermoluminescence dosimetry materials: properties and uses*. 1995.

Murray, A. S. and Wintle, A. G. *Luminescence dating of quartz using an improved single-aliquot regenerative-dose protocol*. Radiation measurements, 32(1): 57–73, 2000.

Sawakuchi, G., Yukihara, E., McKeever, S., and Benton, E. *Optically stimulated luminescence fluence response of Al2O3: C dosimeters exposed to different types of radiation*. Radiation measurements, 43(2-6): 450–454, 2008.

Smedley, R., Duller, G., Rufer, D., and Utley, J. *Empirical assessment of beta dose heterogeneity in sediments: implications for luminescence dating*. Quaternary geochronology, 56: 101052, 2020.

Thomsen, K. J., Bøtter-Jensen, L., Denby, P. M., and Murray, A. *Luminescence response to irradiation using mini X-ray generators*. Nuclear Instruments and Methods in Physics Research Section B: Beam Interactions with Materials and Atoms, 252(2): 267–275, 2006.

Vargas, S. *Optically Stimulated Luminescence dosimetry using Al2O3:C micro crystals*. Technical report, UL - Université de Limoges, 2011.

Yukihara, E. and McKeever, S. *Spectroscopy and optically stimulated luminescence of Al 2 O 3: C using time-resolved measurements*. Journal of applied physics, 100(8): 083512, 2006.

Yukihara, E. and McKeever, S. *Optically stimulated luminescence (OSL) dosimetry in medicine*. Physics in Medicine & Biology, 53(20): R351, 2008.

Yukihara, E., Yoshimura, E., Lindstrom, T., Ahmad, S., Taylor, K., and Mardirossian, G. *High-precision dosimetry for radiotherapy using the optically stimulated luminescence technique and thin Al2O3: C dosimeters*. Physics in Medicine & Biology, 50(23): 5619, 2005.

Reviewer

Kristina Thomsen

Thesis Abstracts

Index

Anca Avram

Multi-method luminescence dating studies using quartz and feldspars extracted from loess deposits in Europe, Asia and Oceania

July 2021

Faculty of Environmental Science and Engineering, Babes-Bolyai University, Cluj-Napoca, Romania

Degree: Ph.D.
Supervisor: Prof. Alida Timar-Gabor

The applicability of the Single-Aliquot Regenerative-dose (SAR-OSL) protocol on quartz as well as the post infrared-infrared protocols ($pIRIR_{225}$ and $pIRIR_{290}$) on polymineral fine grains was assessed for dating loess distributed over three continents, namely Europe (Batajnica section, Serbia), Asia (XuYi profile south-eastern China) and Oceania (South Island of New Zealand).

Since it is well known that feldspars are more difficult to bleach than quartz, residual dose measurements were performed prior to age calculation. Several experiments were carried out, such as: investigating the dependency of the residual as function of the exposure time to sunlight (form 0.5 h to 30 days), or the investigation of the dependency of the residual dose on the equivalent dose magnitude, as well as on the magnitude of various large laboratory given doses (up to 800 Gy). The results showed that $pIRIR_{290}$ signal is more slowly bleached than $pIRIR_{225}$ and the residual doses measured using $pIRIR_{290}$ protocol are larger than those measured by the application of the $pIRIR_{225}$ protocol. Assuming that the measured residual originates from an unbleachable component that is not dose dependent and the values measured in young samples are actually the result of insufficient exposure to light, a time which is characteristic to all samples investigated in a sedimentary context, if the bleaching time is maintained to a fixed period during solar simulator experiments on different samples, then a linear dependency is expected between the equivalent dose of the investigated samples and the measured residual dose values. Therefore, a minimum residual dose corresponding to the unbleachable part of the signal can be determined by extrapolating measured residual dose values to an equivalent dose equal to 0 Gy (D_e = 0 Gy). In the absence of information from modern analogues, which is a common scenario in many dating contexts, this is the most reasonable value to be subtracted from the measured equivalent dose when age calculation is performed.

Since it is unanimously accepted that quartz does not suffer from any signal loss, fading measurements were carried out on polymineral fine grains extracted from loess from Serbia, China and New Zealand by comparison to quartz. Our results show that fading is insignificant for $pIRIR_{225}$ signals.

The performance of the dose recovery tests was extensively investigated for pIRIR protocols by varying both the magnitude of the given dose as well as the magnitude of the test dose. Our results indicate that the $pIRIR_{225}$ protocol can accurately (less than 10% deviation) recover known doses up to ~ 300 – 400 Gy while the application of $pIRIR_{290}$ protocols results in measuring doses that slightly overestimate the given dose for the entire dose rage (100 – 800 Gy) investigated, the overestimation ranging from 12% to 61% and being more significant for larger doses.

While the applicability of the SAR-OSL protocol on New Zealand quartz was hampered by the low luminescence sensitivity of the material, the application of the SAR-OSL protocol on quartz extracted from Serbian and Chinese loess resulted in obtaining robust chronologies for ages up to about 70 ka. Based on the comparison of the natural and laboratory dose response curves for Batajnica samples in Serbia it was concluded that fine and coarse quartz luminescence ages can be accurately measured for samples with equivalent doses up to ~ 150 Gy and ~ 250 Gy, respectively. On the other hand, for the investigated samples the datable dose range can be extended by using feldspars up to 400 Gy. However, the results obtained for equivalent doses larger than 400 Gy should be interpreted with caution in the absence of independent age control for both pIRIR protocols. Overall, our results show that pIRIR protocols can be applied successfully on polymineral fine grains extracted from loess deposits over three continents for extending the quartz datable age range.

Laura del Valle Villalonga

Pleistocene deposits of Pityusic Islands: architecture, luminescence chronology and paleoclimatic implications

July 2021

Faculty of Environmental Science and Engineering, Babes-Bolyai University, Cluj-Napoca, Romania

Degree: Ph.D.
Supervisor: Prof. Alida Timar-Gabor

Coastal areas are dynamic territories that are subjected to the confluence of many factors and agents that are caus-

ing transformations. These modifications and their causes can be identified from the geomorphological evidence. The study of the Pleistocene deposits of Pityusic islands can provide a very good source of information for gaining better knowledge on the history of the climate and environmental conditions, as well as the geomorphological processes that occurred during the Quaternary. This study deals with the sedimentological and stratigraphic description of Pleistocene coastal deposits of the Pityusic Islands that show evidence of interference between processes characteristic of alluvial, marine and aeolian environments. Optically stimulated luminescence (OSL) dating of aeolian levels indicates that deposition took place from the Lower to Upper Pleistocene. The sedimentological and chronological analysis of these deposits allows reconstructing of the coastal Pleistocene environmental history from Marine Isotopic Stage (MIS) 22 to MIS 3. Results show that the main controls on Lower to Upper Pleistocene coastal landscape evolution on Eivissa, Es Freus and Formentera are changes in the average wind direction over time, modulated by the interaction with coastal relief orientation. The main episodes of aeolian activity identified and dune formation in the Western Mediterranean can be linked to periods of low sea level. We conclude that although there were two prevailing environments such as coastal aeolian and alluvial, with different processes and resulting forms, the interaction resulted in deposits that share characteristics of both environments, as well as maintain elements inherited from each environment in terms of sedimentary supply, precipitation, runoff or aeolian transport. Our results are a useful indicator of the geomorphological processes and changes that occurred during the Pleistocene, unravelling the environmental evolution, and contributing to the growing knowledge on the Western Mediterranean aeolian or aeolian-alluvial interacting environments.

Patricia Mescolotti

Fluvial plain and eolian dune field of the middle São Francisco River: chronology of deposits and succession of geological events in the Quaternary of Brazil

December 2021

Instituto de Geociências e Ciências Exatas, Universidade Estadual Paulista - Unesp, Rio Claro, Brazil

Degree: Ph.D.

Supervisors: Mario Luis Assine and Fabiano Pupim

Large rivers, with São Francisco, are dynamic systems whose evolution depends on both internal and external forcing, particularly tectonics, sea level, and climate. The São Francisco River is the easternmost large river of South America, with its upper course in semi-humid settings, but with a watershed mostly under semi-arid conditions. As this is a river with its basin in tectonically quiescent areas and controlled by local base level, the São Francisco River's deposits are an excellent fluvial sedimentary record to shed light on how large tropical rivers responded to climatic changes of the Quaternary. Directly associated with the São Francisco River, the Xique-Xique eolian system is the largest Quaternary interior dune field in Brazil (~ 8,000 km^2). Aiming to establish the chronology of the deposits and the evolution of quaternary geological events for the Xique-Xique dune field and for the alluvial deposits of the São Francisco River, we investigated a 200-km section of the medium course of the São Francisco River in Bahia, northeast Brazil. We use a multi-method approach, using remote sensing methods and field surveys for geomorphological and sedimentological analyses combined with optically stimulated luminescence dating (OSL). Several fluvial and eolian geomorphological zones were characterized, mapped, and dated. Two zones are represented by degraded terraces, and three zones comprise the active confined aggradational plain. We recognized at least four phases of fluvial aggradation (> 90 ka; 65 to 39 ka; 18 to 9.5 ka and 380 years to recent) and three phases of incision (I1 – 85 to 65 ka; I2 – 39 to 18 ka and I3 – 9.5 to 1.0 ka). The eolian field initial developed at least since ~ 250 ka and comprises predominantly stabilized parabolic dunes (simple and compound), sand sheet and modern active parabolic dunes. We recognized two main events of eolian activity (~ 23 to 18 ka and ~ 15 to 10 ka) and two phases of dune stabilization (~ 18 to 15 ka and since 5 ka). We interpret that the two large systems studied here (fluvial and eolian) interact with each other and respond differently to climatic triggers, particularly precipitation. The incision events occurred probably due to increased fluvial discharge produced by intensification of the South Atlantic Convergence Zone, which has great influence on precipitation over the upper São Francisco River. Thus, we conclude that the aggradation-incision cycles of the São Francisco River during the last 100 ka are likely products of millennial precipitation variation. As for the eolian dynamics, the changes in precipitation in the area mainly influenced the process of stabilization of the dunes by vegetation, especially in the humid HS1 (Heinrich 1 event). However, the moments of dune activity were more conditioned by changes in the river sediment supply. Thus, eolian events are closely related to incision/fluvial deposition events in the area, providing an exceptional case of fluvial-eolian interaction in the Quaternary of Brazil. The Xique-Xique eolian system results from the conjugation of sediment carried mostly from the river, high eastern wind speeds, and a significant wind deceleration caused by mountains on the western border of the dune field.

Mariana Sontag González

Development and application of luminescence approaches to dating of Indonesian archaeological and palaeoanthropological sites

December 2021

University of Wollongong, Wollongong, NSW, Australia

Degree: Ph.D.

Supervisors: Bo Li, Richard G. Roberts

Establishing reliable chronologies for archaeological and

palaeoanthropological sites in Indonesia is important for studies of human evolution and dispersal. However, many such sites are situated in volcanic regions, whose sediments are generally difficult to date using luminescence dating methods. Here, the application of improved procedures using the post-infrared infrared stimulated luminescence (pIRIR) signal targeted to dating volcanic sediments is presented on two case studies of archaeological sites in Indonesia with an extended hominin occupation in the Pleistocene: Liang Bua and Leang Bulu Bettue.

Individual mineral grains deposited at Liang Bua, the type locality of *Homo floresiensis*, on Flores, Indonesia, that emit detectable pIRIR signals are composed of a range of feldspar varieties, quartz, clay minerals, heavy minerals and volcanic glass, rendering the isolation of individual potassium-rich feldspar grains infeasible. The luminescence behaviour of these composite mineral grains was investigated in detail, including their thermal stability, anomalous fading and dose-response characteristics. A standardised growth curve (SGC) was developed to enable more time-efficient measurements, together with a 'micro-aliquot' approach in which each hole on a disc contains approximately 8 – 10 grains. Less than 1% of grains yield detectable pIRIR signals when measured individually, so the use of micro-aliquots provides an effective means of estimating the equivalent dose (D_e) at single-grain resolution. The performance tests suggest that the pIRIR signal measured at 275 °C is suitable for estimating D_e values of these composite grains, without the need for residual dose or fading corrections. Internal dose rates were calculated incorporating information on the mineralogical compositions of individual grains that emit a pIRIR signal. Additionally, spatially-resolved beta dose rates from a Timepix pixelated detector informed on the expected scatter of luminescence signal intensities caused by beta dose rate heterogeneity. A total of 41 samples dated with these procedures, from contexts ranging from the basal sediments underlying the *H. floresiens*is-bearing deposits up to the layers with evidence of occupation by anatomically modern humans, were included in a Bayesian model yielding a refined chronostratigraphy for this important site.

Located in the Maros karst region of southwest Sulawesi, the second study site, Leang Bulu Bettue, contains evidence for human symbolic behaviour from ~ 30,000 years ago. Previous research at this site reported high fading rates for K-rich feldspar grains measured using a single-aliquot pIRIR procedure. In this study, the SGC pIRIR procedure for micro-aliquots, at effectively single-grain resolution, was used to (i) test its reliability for D_e estimation and subsequent age determination, and (ii) show that, in contrast to the high fading observed for single aliquots using IR diodes for stimulation, the micro-aliquot results obtained using an IR laser show a low fading rate. The reduced fading rate of the pIRIR signal using the new procedure is due to the selection of low-fading bright grains from a population of grains with mixed fading rates. Additionally, the presence of outlier and insufficiently bleached grains was considered in the choice of age models used for D_e determination. New pIRIR ages at single-grain resolution support the use of these methods to date dim volcanic samples with minimal fading corrections, allowing for an extension of the known chronology of hominin occupation at the site. A PDF of this thesis is available upon request (Mariana.Sontag-Gonzalez@geogr.uni-giessen.de)

Bibliography

Compiled by Sebastien Huot

From 1st June 2021 to 30th November 2021

Various geological applications

- aeolian

Chen, Y., Huang, C.C., Zhang, Y., Zhou, Y., Zha, X., Wang, N., Shang, R., Rong, X., Jia, Y.-n., Wang, H., 2021. Palaeoflood events during the last deglaciation in the Yellow River source area on the northeast Tibetan Plateau. Geological Journal 56, 4293-4309, http://doi.org/10.1002/gj.4164

Dong, G., Li, T., Zhang, S., Ren, L., Li, R., Li, G., Xiao, Y., Wang, Z., Chen, F., 2021. Precipitation in surrounding mountains instead of lowlands facilitated the prosperity of ancient civilizations in the eastern Qaidam Basin of the Tibetan Plateau. CATENA 203, 105318, http://doi.org/10.1016/j.catena.2021.105318

Han, Z., Ren, Y., Li, X., Liu, Y., Xu, W., Li, Y., Pan, R., 2022. Formation of parabolic dunes on the shore of Poyang Lake in East China. Geomorphology 397, 108023, http://doi.org/10.1016/j.geomorph.2021.108023

Lindhorst, S., Reimann, T., 2021. Residual dune ridges: Sedimentary architecture, genesis, and implications for palaeo-climate reconstructions. Earth Surface Processes and Landforms 46, 2177-2194, http://doi.org/10.1002/esp.5167

Richards, J., Burrough, S., Wiggs, G., Hills, T., Thomas, D., Moseki, M., 2021. Uneven surface moisture as a driver of dune formation on ephemeral lake beds under conditions similar to the present day: A model-based assessment from the Makgadikgadi Basin, northern Botswana. Earth Surface Processes and Landforms 46, 3078-3095, http://doi.org/10.1002/esp.5215

Yang, H., Zhao, H., Wang, X., Wang, K., Niu, Q., Zhang, J., Liu, B., 2021. Optical dating of Yardang sediments and its implications for past flood events on the border of the Badain Jaran Desert, Northern China. CATENA 207, 105614, http://doi.org/10.1016/j.catena.2021.105614

Zheng, F., Li, Z., Jin, J., Zhang, W., Li, Z., Xu, X., Cheng, Y., 2021. Luminescence geochronology and paleoenvironmental implications of coastal red dune sands of northeast Hainan Island, China. Aeolian Research 53, 100744, http://doi.org/10.1016/j.aeolia.2021.100744

- alluvial fan

Goehring, B.M., Brown, N., Moon, S., Blisniuk, K., 2021. The Transport History of Alluvial Fan Sediment Inferred From Multiple Geochronometers. Journal of Geophysical Research: Earth Surface 126, e2021JF006096, http://doi.org/10.1029/2021JF006096

- cave

Bartolomé, M., Sancho, C., Benito, G., Medialdea, A., Calle, M., Moreno, A., Leunda, M., Luetscher, M., Muñoz, A., Bastida, J., Cheng, H., Edwards, R.L., 2021. Effects of glaciation on karst hydrology and sedimentology during the Last Glacial Cycle: The case of Granito cave, Central Pyrenees (Spain). CATENA 206, 105252, http://doi.org/10.1016/j.catena.2021.105252

Kurečić, T., Bočić, N., Wacha, L., Bakrač, K., Grizelj, A., Tresić Pavičić, D., Lüthgens, C., Sironić, A., Radović, S., Redovniković, L., Fiebig, M., 2021. Changes in cave sedimentation mechanisms during the Late Quaternary: An example from the Lower Cerovačka Cave, Croatia. Frontiers in Earth Science 9, 672229, http://doi.org/10.3389/feart.2021.672229

- coastal

Alappat, L., Frechen, M., Tsukamoto, S., Anupama, K., Prasad, S., Gopakumar, P.G., Kumar, S.S., 2021. Evidences of early to mid-Holocene land–sea interactions and formation of Wetlands of Central Kerala in the south west coast of India. Regional Studies in Marine Science 48, 102009, http://doi.org/10.1016/j.rsma.2021.102009

Alexandrakis, G., Petrakis, S., Kampanis, N.A., 2021. Integrating Geomorphological Data, Geochronology and Archaeological Evidence for Coastal Landscape Reconstruction, the Case of Ammoudara Beach, Crete. Water 13, 1269, http://doi.org/10.3390/w13091269

Barboza, E.G., Dillenburg, S.R., do Nascimento Ritter, M., Angulo, R.J., da Silva, A.B., da Camara Rosa, M.L.C., Caron, F., de Souza, M.C., 2021. Holocene sea-level changes in southern Brazil based on high-resolution radar stratigraphy. Geosciences 11, 326, https://www.mdpi.com/2076-3263/11/8/326

Bhattacharya, F., 2021. Mid to Late-Holocene relative sea-level fluctuations and palaeoenvironment: Evidences from the southern Saurashtra coast, western India. Quaternary International 599-600, 62-71, http://doi.org/10.1016/j.quaint.2020.08.047

Bogo, M., Nascimento, M.G.d., Souza, M.C.d., Angulo, R.J., Guedes, C.C.F., Rosa, M.L.C.d.C., Barboza, E.G., 2021. Spit-Inlet migration and storm-driven stacking at Praia de Leste Holocene barrier, southern Brazil. Marine Geology 442, 106637, http://doi.org/10.1016/j.margeo.2021.106637

Chamberlain, E.L., Shen, Z., Kim, W., McKinley, S., Anderson, S., Törnqvist, T.E., 2021. Does Load-Induced Shallow Subsidence Inhibit Delta Growth? Journal of Geophysical Research: Earth Surface 126, e2021JF006153, http://doi.org/10.1029/2021JF006153

del Valle, L., Timar-Gabor, A., Fornós, J.J., Pons, G.X., 2020. Lower to Upper Pleistocene coastal deposits from the Ses Salines, Es Freus Islets and Cala Sabina (Pityusic Islands, Western Mediterranean): chronology and evolution. Journal of Coastal Research 95, 448-452, http://doi.org/10.2112/SI95-087.1

Delong, K.L., Gonzalez, S., Obelcz, J.B., Truong, J.T., Bentley Sr, S.J., Xu, K., Reese, C.A., Harley, G.L., Caporaso, A., Shen, Z., Middleton, B.A., 2021. Late Pleistocene baldcypress (Taxodium distichum) forest deposit on the continental shelf of the northern Gulf of Mexico. Boreas 50, 871-892, http://doi.org/10.1111/bor.12524

Erginal, A.E., Polymeris, G.S., Erenoğlu, O., Giannoulatou, V., Meriç, E., Karataş, A., Şahiner, E., Selim, H.H., 2021. New record of calcarenite in Hatay, Turkey: an evidence of the Late Pleistocene Eastern Mediterranean–Red Sea connection. Arabian Journal of Geosciences 14, 2104, http://doi.org/10.1007/s12517-021-08521-1

Fakolade, R.O., Ikhane, P.R., Zhao, Q., Hao, Q., Alexanderson, H., Guo, Z., 2021. Luminescence dating of holocene siliciclastic sediments in eastern Dahomey Basin, southwestern Nigeria. Quaternary International 598, 90-96, http://doi.org/10.1016/j.quaint.2021.05.024

Figueiredo, M.S., Brill, D., Rocha, T.B.d., Fernandez, G.B., 2021. Late Holocene evolution of São Tomé cape (Rio de Janeiro, Brazil): Insights from geomorphological, geophysical and geochronological data. Quaternary International 602, 15-29, http://doi.org/10.1016/j.quaint.2021.04.001

Fisher, T.G., DeVries-Zimmerman, S.J., Hansen, E.C., Wolin, J.A., Lepper, K., Spanbauer, T., 2021. Drought coincident with aeolian activity in a Great Lakes coastal dune setting during the Algoma Phase (3.1–2.4 ka), southwest Michigan. Journal of Great Lakes Research 47, 1468-1484, http://doi.org/10.1016/j.jglr.2021.04.017

Lopes, R.P., Pereira, J.C., Kinoshita, A., Mollemberg, M., Barbosa, F., Baffa, O., 2020. Geological and taphonomic significance of electron spin resonance (ESR) ages of Middle-Late Pleistocene marine shells from barrier-lagoon systems of Southern Brazil. Journal of South American Earth Sciences 101, 102605, http://doi.org/10.1016/j.jsames.2020.102605

Lopes, R.P., Silva de Souza, M., Pereira, J.C., Raupp, S.V., Tatumi, S.H., Yee, M., Dillenburg, S.R., 2021. Late Pleistocene-Holocene diatomites from the coastal plain of southern Brazil: Paleoenvironmental implications. Quaternary International 598, 38-55, http://doi.org/10.1016/j.quaint.2021.04.041

Micallef, A., Marchis, R., Saadatkhah, N., Pondthai, P., Everett, M.E., Avram, A., Timar-Gabor, A., Cohen, D., Preca Trapani, R., Weymer, B.A., Wernette, P., 2021. Groundwater erosion of coastal gullies along the Canterbury coast (New Zealand): a rapid and episodic process controlled by rainfall intensity and substrate variability. Earth Surface Dynamics 9, 1-18, http://doi.org/10.5194/esurf-9-1-2021

Shawler, J.L., Hein, C.J., Obara, C.A., Robbins, M.G., Huot, S., Fenster, M.S., 2021. The effect of coastal landform development on decadal-to millennial-scale longshore sediment fluxes: Evidence from the Holocene evolution of the central mid-Atlantic coast, USA. Quaternary Science Reviews 267, 107096, http://doi.org/10.1016/j.quascirev.2021.107096

Souza, P.E., Sohbati, R., Murray, A.S., Clemmensen, L.B., Kroon, A., Nielsen, L., 2021. Optical dating of cobble surfaces determines the chronology of Holocene beach ridges in Greenland. Boreas 50, 606-618, http://doi.org/10.1111/bor.12507

Strobel, P., Bliedtner, M., Carr, A.S., Frenzel, P., Klaes, B., Salazar, G., Struck, J., Szidat, S., Zech, R., Haberzettl, T., 2021. Holocene sea level and environmental change at the southern Cape – an 8.5 kyr multi-proxy paleoclimate record from Lake Voëlvlei, South Africa. Climate of the Past 17, 1567-1586, http://doi.org/10.5194/cp-17-1567-2021

Zheng, F., Li, Z., Jin, J., Zhang, W., Li, Z., Xu, X., Cheng, Y., 2021. Luminescence geochronology and paleoenvironmental implications of coastal red dune sands of northeast Hainan Island, China. Aeolian Research 53, 100744, http://doi.org/10.1016/j.aeolia.2021.100744

- colluvial

Persico, L.P., McFadden, L.D., McAuliffe, J.R., Rittenour, T.M., Stahlecker, T.E., Dunn, S.B., Brody, S.A.T., 2021. Late Quaternary geochronologic record of soil formation and erosion: Effects of climate change on Mojave Desert hillslopes (Nevada, USA). Geology 50, 54-59, http://doi.org/10.1130/G49270.1

- earthquake (and fault related)

Castillo, B.A., McGill, S.F., Scharer, K.M., Yule, D., McPhillips, D., McNeil, J., Saha, S., Brown, N.D., Moon, S., 2021. Prehistoric earthquakes on the Banning strand of the San Andreas fault, North Palm Springs, California. Geosphere 17, 685-710, http://doi.org/10.1130/GES02237.1

DuRoss, C.B., Zellman, M.S., Thackray, G.D., Briggs, R.W., Gold, R.D., Mahan, S.A., 2020. Holocene paleoseismology of the Steamboat Mountain site: Evidence for full-length rupture of the Teton fault, Wyoming. Bulletin of the Seismological Society of America 111, 439-465, http://doi.org/10.1785/0120200212

Jain, S., Bhu, H., Kothyari, G.C., 2021. Quaternary deformation in south-western Luni-Sukri basin, Rajasthan, India. Arabian Journal of Geosciences 14, 1468, http://doi.org/10.1007/s12517-021-07710-2

King, T.R., Quigley, M., Clark, D., Zondervan, A., May, J.-H., Alimanovic, A., 2021. Paleoseismology of the 2016 MW 6.1 Petermann earthquake source: Implications for intraplate earthquake behaviour and the geomorphic longevity of bedrock fault scarps in a low strain-rate cratonic region. Earth Surface Processes and Landforms 46, 1238-1256, http://doi.org/10.1002/esp.5090

Kothyari, G.C., Kandregula, R.S., Kotlia, B.S., Lakhote, A., Swamy, K.V., Pathak, V., Chauhan, G., Thakkar, M.G., 2021. Palaeoseismic investigations along the Kachchh Mainland Fault: A comprehensive review and new insights of the past earthquakes in the Kachchh basin, western India. Quaternary International 599-600, 184-209, http://doi.org/10.1016/j.quaint.2020.08.042

Lee, C.H., Seong, Y.B., Oh, J.S., 2021. Determining the Slip Rate and Earthquake Recurrence Interval on the Tip of a Foreberg in the Gobi-Altai, Mongolia. Russian Geology and Geophysics 62, 1296-1307, http://doi.org/10.2113/RGG20194145

McCalpin, J.P., Jones, L.C.A., 2021. The Stillwater scarp, central Nevada, USA; coseismic gravitational failure on a 1.200-M-high range-front escarpment. Environmental and Engineering Geoscience 27, 377-393, http://doi.org/10.2113/EEG-D-21-00007

McCalpin, J.P., Pavlis, T.L., Jones, L.C.A., Green, D., Hurtado, J.M., 2021. Tectonic geomorphology and paleoseismology of the northern East Franklin Mountains fault, El Paso, Texas, USA. Quaternary International 598, 110-122, http://doi.org/10.1016/j.quaint.2021.04.040

McGill, S.F., Owen, L.A., Weldon, R.J., Kendrick, K.J., Burgette, R.J., 2021. Latest Quaternary slip rates of the San Bernardino strand of the San Andreas fault, southern California, from Cajon Creek to Badger Canyon. Geosphere 17, 1354-1381, http://doi.org/10.1130/GES02231.1

McGregor, I.S., Onderdonk, N.W., 2021. Late Pleistocene rates of rock uplift and faulting at the boundary between the southern Coast Ranges and the western Transverse Ranges in California from reconstruction and luminescence dating of the Orcutt Formation. Geosphere 17, 932-956, http://doi.org/10.1130/GES02274.1

Moreno, D., Gutiérrez, F., Val, M.d., Carbonel, D., Jiménez, F., Jesús Alonso, M., Martínez-Pillado, V., Guzmán, O., López, G.I., Martínez, D., 2021. A multi-method dating approach to reassess the geochronology of faulted Quaternary deposits in the central sector of the Iberian Chain (NE Spain). Quaternary Geochronology 65, 101185, http://doi.org/10.1016/j.quageo.2021.101185

Patyniak, M., Landgraf, A., Dzhumabaeva, A., Baikulov, S., Williams, A.M., Weiss, J.R., Hilley, G.E., Preusser, F., Abdrakhmatov, K.E., Arrowsmith, R.J., Strecker, M.R., 2021. The Pamir Frontal Thrust Fault: Holocene Full-Segment Ruptures and Implications for Complex Segment Interactions in a Continental Collision Zone. Journal of Geophysical Research: Solid Earth 126, e2021JB022405, http://doi.org/10.1029/2021JB022405

Pazzaglia, F.J., Malenda, H.F., McGavick, M.L., Raup, C., Carter, M.W., Berti, C., Mahan, S., Nelson, M., Rittenour, T.M., Counts, R., Willenbring, J., Germanoski, D., Peters, S.C., Holt, W.D., 2021. River Terrace Evidence of Tectonic Processes in the Eastern North American Plate Interior, South Anna River, Virginia. The Journal of Geology 129, 595-624, http://doi.org/10.1086/712636

Sun, C., Li, D., Li, L., 2021. The paleoearthquakes of the Langshan Piedmont fault, North China since late Pleistocene. Natural Hazards Research 1, 48-62, http://doi.org/10.1016/j.nhres.2021.06.005

Van Balen, R.T., Kasse, C., Wallinga, J., Woolderink, H.A.G., 2021. Middle to Late Pleistocene faulting history of the Heerlerheide fault, Roer Valley Rift System, influenced by glacio-isostasy and mining-induced displacement. Quaternary Science Reviews 268, 107111, http://doi.org/10.1016/j.quascirev.2021.107111

Zhang, H., He, Z., Xu, H., Li, L., Wang, J., Jiang, X., Zhao, Q., Yang, H., 2021. Kinematic Characteristics of the Jiangsu Segment of the Anqiu–Juxian Fault in the Tanlu Fault Zone, Eastern China. Lithosphere 2021, 6691692, http://doi.org/10.2113/2021/6691692

- fluvial

Avşin, N., Erturaç, M.K., Şahiner, E., Demir, T., 2021. The Quaternary climatic and tectonic development of the Murat River valley (Muş Basin, Eastern Turkey) as recorded by fluvial deposits dated by optically stimulated luminescence. Quaternary 4, 29, http://doi.org/10.3390/quat4030029

Breda, C., do Nascimento Pupim, F., Sawakuchi, A.O., Mineli, T.D., 2021. The role of bedrock and climate for the Late Quaternary erosive-depositional behavior of an intraplate tropical river: The Tietê River case, southeastern Brazil. Geomorphology 389, 107834, http://doi.org/10.1016/j.geomorph.2021.107834

Chaudhri, A.R., Chopra, S., Kumar, P., Ranga, R., Singh, Y., Rajput, S., Sharma, V., Verma, V.K., Sharma, R., 2021. Saraswati River in northern India (Haryana) and its role in populating the Harappan civilization sites—A study based on remote sensing, sedimentology, and strata chronology. Archaeological Prospection 28, 565-582, http://doi.org/10.1002/arp.1829

Cheliz, P.M., Bernardes Ladeira, F.S., Rodrigues, J.A., Fonseca Giannini, P.C., Do Nascimento Pupim, F., Desiree Mineli, T., Rodrigues, R.A., 2021. Landscape evolution and unusual geomorphological-pedological-chronological relations in an alluvial plain associated with early Amerindian settlement in southeastern Brazil. Quaternary International 601, 1-14, http://doi.org/10.1016/j.quaint.2021.06.016

Chen, Y., Huang, C.C., Zhang, Y., Zhou, Y., Zha, X., Wang, N., Shang, R., Rong, X., Jia, Y.-n., Wang, H., 2021. Palaeoflood events during the last deglaciation in the Yellow River source area on the northeast Tibetan Plateau. Geological Journal 56, 4293-4309, http://doi.org/10.1002/gj.4164

Colton, D., Whitfield, E., Plater, A.J., Duller, G.A.T., Jain, M., Barham, L., 2021. New geomorphological and archaeological evidence for drainage evolution in the Luangwa Valley (Zambia) during the Late Pleistocene. Geomorphology 392, 107923, http://doi.org/10.1016/j.geomorph.2021.107923

Gouveia, M.P., Cunha, P.P., Falguères, C., Voinchet, P., Martins, A.A., Bahain, J.-J., Pereira, A., 2020. Electron spin resonance dating of the culminant allostratigraphic unit of the Mondego and Lower Tejo Cenozoic basins (W Iberia), which predates fluvial incision into the basin-fill sediments. Global and Planetary Change 184, 103081, http://doi.org/10.1016/j.gloplacha.2019.103081

Ishii, Y., Takahashi, T., Ito, K., 2022. Luminescence dating of cobbles from Pleistocene fluvial terrace deposits of the Ara River, Japan. Quaternary Geochronology 67, 101228, http://doi.org/10.1016/j.quageo.2021.101228

Last, G.V., Rittenour, T.M., 2021. Chronology of Missoula flood deposits at the Coyote Canyon Mammoth Site, Washington State, USA. Quaternary 4, 20, http://doi.org/10.3390/quat4030020

Lewis, S.G., Ashton, N., Davis, R., Hatch, M., Hoare, P.G., Voinchet, P., Bahain, J.-J., 2021. A revised terrace stratigraphy and chronology for the early Middle Pleistocene Bytham River in the Breckland of East Anglia, UK. Quaternary Science Reviews 269, 107113, http://doi.org/10.1016/j.quascirev.2021.107113

Liu, Y., Wang, X., Su, Q., Yi, S., Miao, X., Li, Y., Lu, H., 2021. Late Quaternary terrace formation from knickpoint propagation in the headwaters of the Yellow River, NE Tibetan Plateau. Earth Surface Processes and Landforms 46, 2788-2806, http://doi.org/10.1002/esp.5208

Marcotte, A.L., Neudorf, C.M., Langston, A.L., 2021. Lateral bedrock erosion and valley formation in a heterogeneously layered landscape, Northeast Kansas. Earth Surface Processes and Landforms 46, 2248-2263, http://doi.org/10.1002/esp.5172

Mescolotti, P.C., Pupim, F.d.N., Ladeira, F.S.B., Sawakuchi, A.O., Santa Catharina, A., Assine, M.L., 2021. Fluvial aggradation and incision in the Brazilian tropical semi-arid: Climate-controlled landscape evolution of the São Francisco River. Quaternary Science Reviews 263, 106977, http://doi.org/10.1016/j.quascirev.2021.106977

Niyonzima, P., Sawakuchi, A.O., Bertassoli, D.J., Pupim, F.N., Porat, N., Freire, M.P., Góes, A.M., Rodrigues, F.C.G., 2022. Luminescence dating of quartz from ironstones of the Xingu River, Eastern Amazonia. Quaternary Geochronology 67, 101241, http://doi.org/10.1016/j.quageo.2021.101241

Parés, J.M., Duval, M., Soria-Jáuregui, A., González-Amuchástegui, M.J., 2021. First chronological constraints for the high terraces of the Upper Ebro Catchment. Quaternary 4, 25, https://www.mdpi.com/2571-550X/4/3/25

Passos, M.S., Soares, E.A.A., Tatumi, S.H., Yee, M., Mittani, J.C.R., Hayakawa, E.H., Salazar, C.A., 2020. Pleistocene-Holocene sedimentary deposits of the Solimões-Amazonas fluvial system, Western Amazonia. Journal of South American Earth Sciences 98, 102455, http://doi.org/10.1016/j.jsames.2019.102455

Pazzaglia, F.J., Malenda, H.F., McGavick, M.L., Raup, C., Carter, M.W., Berti, C., Mahan, S., Nelson, M., Rittenour, T.M., Counts, R., Willenbring, J., Germanoski, D., Peters, S.C., Holt, W.D., 2021. River Terrace Evidence of Tectonic Processes in the Eastern North American Plate Interior, South Anna River, Virginia. The Journal of Geology 129, 595-624, http://doi.org/10.1086/712636

Perez Filho, A., Moreira, V.B., Lämmle, L., Torres, B.A., Valezio, É.V., Rubira, F.G., Aderaldo, P.I.C., Souza, A.O., 2021. Depositional rates obtained from absolute dating on surficial covers in the paulista peripheral depression, SE-Brazil. Journal of South American Earth Sciences 111, 103491, http://doi.org/10.1016/j.jsames.2021.103491

Skirrow, G.K., Smedley, R.K., Chiverrell, R.C., Hooke, J.M., 2021. Planform change of the Río Chubut (~42°S, ~70°W, Argentina) in response to climate drivers in the southern Andes. Geomorphology 393, 107924, http://doi.org/10.1016/j.geomorph.2021.107924

Wu, C., Long, H., Cheng, T., Liu, L., Qian, P., Wang, H., Ren, S., Zhou, L., Zheng, X., 2021. Quantitative estimations of iron oxide minerals in the Late Pleistocene paleosol of the Yangtze River Delta: Implications for the chemical weathering, sedimentary environment, and burial conditions. CATENA 207, 105662, http://doi.org/10.1016/j.catena.2021.105662

Xu, Y., Tian, T., Shen, Q., Luo, L., Lai, Z., 2021. Late Quaternary aggradation of the Datong Basin in northern China revealed by OSL dating of core sediments and implications for groundwater arsenic pollution. CATENA 207, 105650, http://doi.org/10.1016/j.catena.2021.105650

- glacial and periglacial

Bartolomé, M., Sancho, C., Benito, G., Medialdea, A., Calle, M., Moreno, A., Leunda, M., Luetscher, M., Muñoz, A., Bastida, J., Cheng, H., Edwards, R.L., 2021. Effects of glaciation on karst hydrology and sedimentology during the Last Glacial Cycle: The case of Granito cave, Central Pyrenees (Spain). CATENA 206, 105252, http://doi.org/10.1016/j.catena.2021.105252

Benetti, S., Chiverrell, R.C., Cofaigh, C.Ó., Burke, M., Medialdea, A., Small, D., Ballantyne, C., Bateman, M.D., Callard, S.L., Wilson, P., Fabel, D., Clark, C.D., Arosio, R., Bradley, S., Dunlop, P., Ely, J.C., Gales, J., Livingstone, S.J., Moreton, S.G., Purcell, C., Saher, M., Schiele, K., Van Landeghem, K., Weilbach, K., 2021. Exploring controls of the early and stepped deglaciation on the western margin of the British Irish Ice Sheet. Journal of Quaternary Science 36, 833-870, http://doi.org/10.1002/jqs.3315

Bisht, P., Rawat, A., 2021. Timing of late quaternary glaciations in the Yankti Kuti valley of the upper Kali Ganga catchment, Northern India. Quaternary Science Reviews 273, 107246, http://doi.org/10.1016/j.quascirev.2021.107246

Bradwell, T., Fabel, D., Clark, C.D., Chiverrell, R.C., Small, D., Smedley, R.K., Saher, M.H., Moreton, S.G., Dove, D., Callard, S.L., Duller, G.A.T., Medialdea, A., Bateman, M.D., Burke, M.J., McDonald, N., Gilgannon, S., Morgan, S., Roberts, D.H., Cofaigh, C.ó., 2021. Pattern, style and timing of British–Irish Ice Sheet advance and retreat over the last 45 000 years: evidence from NW Scotland and the adjacent continental shelf. Journal of Quaternary Science 36, 871-933, http://doi.org/10.1002/jqs.3296

Chiverrell, R.C., Thomas, G.S.P., Burke, M., Medialdea, A., Smedley, R., Bateman, M., Clark, C., Duller, G.A.T., Fabel, D., Jenkins, G., Ou, X., Roberts, H.M., Scourse, J., 2021. The evolution of the terrestrial-terminating Irish Sea glacier during the last glaciation. Journal of Quaternary Science 36, 752-779, http://doi.org/10.1002/jqs.3229

Evans, D.J.A., Roberts, D.H., Bateman, M.D., Clark, C.D., Medialdea, A., Callard, L., Grimoldi, E., Chiverrell, R.C., Ely, J., Dove, D., Ó Cofaigh, C., Saher, M., Bradwell, T., Moreton, S.G., Fabel, D., Bradley, S.L., 2021. Retreat dynamics of the eastern sector of the British–Irish Ice Sheet during the last glaciation. Journal of Quaternary Science 36, 723-751, http://doi.org/10.1002/jqs.3275

Fairburn, W.A., Bateman, M.D., 2021. Possible new evidence for Mid-Pleistocene glaciation in the Vale of Pickering, North Yorkshire, UK. Proceedings of the Yorkshire Geological Society 63, pygs2020-2019, http://doi.org/10.1144/pygs2020-019

Hickin, A.S., Lian, O.B., Telka, A., Levson, V.M., Geertsema, M., 2021. Geomorphic and ecological age constraints for paraglacial to non-glacial transition in northeastern British Columbia, Canada. Quaternary Science Reviews 268, 107002, http://doi.org/10.1016/j.quascirev.2021.107002

Kleman, J., Hättestrand, M., Borgström, I., Preusser, F., Fabel, D., 2020. The Idre marginal moraine – An anchorpoint for Middle and Late Weichselian ice sheet chronology. Quaternary Science Advances 2, 100010, http://doi.org/10.1016/j.qsa.2020.100010

Kumar, V., Mehta, M., Shukla, A., Kumar, A., Garg, S., 2021. Late Quaternary glacial advances and equilibrium-line altitude changes in a semi-arid region, Suru Basin, western Himalaya. Quaternary Science Reviews 267, 107100, http://doi.org/10.1016/j.quascirev.2021.107100

Lüthgens, C., Hardt, J., Böse, M., 2020. Proposing a new conceptual model for the reconstruction of ice dynamics in the SW sector of the Scandinavian Ice Sheet (SIS) based on the reinterpretation of published data and new evidence from optically stimulated luminescence (OSL) dating. E&G Quaternary Science Journal 69, 201-223, http://doi.org/10.5194/egqsj-69-201-2020

Preusser, F., Büschelberger, M., Kemna, H.A., Miocic, J., Mueller, D., May, J.-H., 2021. Exploring possible links between Quaternary aggradation in the Upper Rhine Graben and the glaciation history of northern Switzerland. International Journal of Earth Sciences 110, 1827-1846, http://doi.org/10.1007/s00531-021-02043-7

Scourse, J.D., Chiverrell, R.C., Smedley, R.K., Small, D., Burke, M.J., Saher, M., Van Landeghem, K.J.J., Duller, G.A.T., Cofaigh, C.Ó., Bateman, M.D., Benetti, S., Bradley, S., Callard, L., Evans, D.J.A., Fabel, D., Jenkins, G.T.H., McCarron, S., Medialdea, A., Moreton, S., Ou, X., Praeg, D., Roberts, D.H., Roberts, H.M., Clark, C.D., 2021. Maximum extent and readvance dynamics of the Irish Sea Ice Stream and Irish Sea Glacier since the Last Glacial Maximum. Journal of Quaternary Science 36, 780-804, http://doi.org/10.1002/jqs.3313

Serra, E., Valla, P.G., Gribenski, N., Guedes Magrani, F., Carcaillet, J., Delaloye, R., Grobéty, B., Braillard, L., 2021. Geomorphic response to the Lateglacial–Holocene transition in high Alpine regions (Sanetsch Pass, Swiss Alps). Boreas 50, 242-261, http://doi.org/10.1111/bor.12480

Simms, A.R., Bentley, M.J., Simkins, L.M., Zurbuchen, J., Reynolds, L.C., DeWitt, R., Thomas, E.R., 2021. Evidence for a "Little Ice Age" glacial advance within the Antarctic Peninsula – Examples from glacially-overrun raised beaches. Quaternary Science Reviews 271, 107195, http://doi.org/10.1016/j.quascirev.2021.107195

West, G., Alexanderson, H., Jakobsson, M., O'Regan, M., 2021. Optically stimulated luminescence dating supports pre-Eemian age for glacial ice on the Lomonosov Ridge off the East Siberian continental shelf. Quaternary Science Reviews 267, 107082, http://doi.org/10.1016/j.quascirev.2021.107082

Woźniak, P.P., Belzyt, S., Pisarska-Jamroży, M., Woronko, B., Lamsters, K., Nartišs, M., Bitinas, A., 2021. Liquefaction and re-liquefaction of sediments induced by uneven loading and glacigenic earthquakes: Implications of results from the Latvian Baltic Sea coast. Sedimentary Geology 421, 105944, http://doi.org/10.1016/j.sedgeo.2021.105944

- lacustrine

An, F., Chen, T., Li, X., Liu, X., Wang, Y., Chen, Z., Chongyi, E., 2021. Formation, mechanism and significance of alluvial-dammed lakes in Golmud River catchment, north-eastern Qinghai-Tibetan Plateau. Earth Surface Processes and Landforms 46, 2421-2436, http://doi.org/10.1002/esp.5186

Bayer Altın, T., Kayseri-Özer, M.S., Altın, B.N., 2021. The Holocene terraces of the desiccated Bor Lake and Neolithic occupation in Bor Plain, Central Anatolia, Turkey. Environmental Earth Sciences 80, 525, http://doi.org/10.1007/s12665-021-09835-9

Belzyt, S., Pisarska-Jamroży, M., Bitinas, A., Woronko, B., Phillips, E.R., Piotrowski, J.A., Jusienė, A., 2021. Repetitive Late Pleistocene soft-sediment deformation by seismicity-induced liquefaction in north-western Lithuania. Sedimentology 68, 3033-3056, http://doi.org/10.1111/sed.12883

Hein, M., Urban, B., Tanner, D.C., Buness, A.H., Tucci, M., Hoelzmann, P., Dietel, S., Kaniecki, M., Schultz, J., Kasper, T., von Suchodoletz, H., Schwalb, A., Weiss, M., Lauer, T., 2021. Eemian landscape response to climatic shifts and evidence for northerly Neanderthal occupation at a palaeolake margin in northern Germany. Earth Surface Processes and Landforms 46, 2884-2901, http://doi.org/10.1002/esp.5219

Ma, X., Yin, G., Wei, C., Qiang, X., Ma, Y., Liu, C., Zhao, Z., Gong, L., Wang, L., Ji, H., Bai, M., Mao, J., Li, G., 2022. High-resolution late Pliocene-quaternary magnetostratigraphy of the Yinchuan Basin, NE Tibetan Plateau. Quaternary International 607, 120-127, http://doi.org/10.1016/j.quaint.2021.09.009

Wang, X., Chun, X., Zhou, H., Zhang, Y., Wan, Z., Dan, D., 2021. Application of standardised growth curves in quartz OSL dating of lacustrine sediments on the Mongolian Plateau. Quaternary International 592, 51-59, http://doi.org/10.1016/j.quaint.2021.04.018

Xu, Y., Tian, T., Shen, Q., Luo, L., Lai, Z., 2021. Late Quaternary aggradation of the Datong Basin in northern China revealed by OSL dating of core sediments and implications for groundwater arsenic pollution. CATENA 207, 105650, http://doi.org/10.1016/j.catena.2021.105650

Zeeden, C., Hambach, U., Klasen, N., Fischer, P., Schulte, P., Nett, J.J., Veres, D., Obreht, I., Chu, W., Papadopoulou, M., Viehberg, F., SchÄBitz, F., Gavrilov, M.B., MarkoviĆ, S.B., VÖTt, A., Lehmkuhl, F., 2021. Sedimentology of a Late Quaternary lacustrine record from the south-eastern Carpathian Basin. Journal of Quaternary Science 36, 1414-1425, http://doi.org/10.1002/jqs.3297

- loess

Avram, A., Constantin, D., Hao, Q., Timar-Gabor, A., 2022. Optically stimulated luminescence dating of loess in South-Eastern China using quartz and polymineral fine grains. Quaternary Geochronology 67, 101226, http://doi.org/10.1016/j.quageo.2021.101226

Fitzsimmons, K.E., Perić, Z., Nowatzki, M., Lindauer, S., Vinnepand, M., Prud'homme, C., Dave, A.K., Vött, A., Fischer, P., 2022. Luminescence Sensitivity of Rhine Valley Loess: Indicators of Source Variability? Quaternary 5, http://doi.org/10.3390/quat5010001

Jia, Y.-n., Zhang, Y., Huang, C.C., Wang, N., Qiu, H., Wang, H., Xiao, Q., Chen, D., Lin, X., Zhu, Y., Fu, L., Gu, K., Patton, N.R., 2022. Late Pleistocene-Holocene aeolian loess-paleosol sections in the Yellow River source area on the northeast Tibetan Plateau: chronostratigraphy, sediment provenance, and implications for paleoclimate reconstruction. CATENA 208, 105777, http://doi.org/10.1016/j.catena.2021.105777

Liu, L., Yang, S., Cheng, T., Liu, X., Luo, Y., Liu, N., Chen, H., Chen, Z., Li, P., Liu, W., 2021. Chronology and dust mass accumulation history of the Wenchuan loess on eastern Tibetan Plateau since the last glacial. Aeolian Research 53, 100748, http://doi.org/10.1016/j.aeolia.2021.100748

Miao, X., Chongyi, E., Xu, S., Wang, Q., Hanson, P.R., Chen, H., Shi, Y., 2022. Age and source of coastal loess in Shandong Peninsula, Bohai Sea, China: Implications for dust aggradation in respond to sea-level change. Aeolian Research 54, 100767, http://doi.org/10.1016/j.aeolia.2021.100767

Moine, O., Antoine, P., Coutard, S., Guérin, G., Hatté, C., Paris, C., Saulnier-Copard, S., 2021. Intra-interstadial environmental changes in Last Glacial loess revealed by molluscan assemblages from the Upper Palaeolithic site of Amiens-Renancourt 1 (Somme, France). Journal of Quaternary Science 36, 1322-1340, http://doi.org/10.1002/jqs.3312

Panin, P.G., Filippova, K.G., Bukhonov, A.V., Karpukhina, N.V., Kalinin, P.I., Ruchkin, M.V., 2021. High-resolution analysis of the Likhvin loess-paleosol sequence (the central part of the East European Plain, Russia). CATENA 205, 105445, http://doi.org/10.1016/j.catena.2021.105445

Perić, Z.M., Marković, S.B., Filyó, D., Thiel, C., Murray, A.S., Gavrilov, M.B., Nett, J.J., Sipos, G., 2021. Quartz OSL and polymineral post IR–IRSL dating of the Požarevac loess–palaeosol sequence in north–eastern Serbia. Quaternary Geochronology 66, 101216, http://doi.org/10.1016/j.quageo.2021.101216

Schmidt, C., Zeeden, C., Krauß, L., Lehmkuhl, F., Zöller, L., 2021. A chronological and palaeoenvironmental re-evaluation of two loess-palaeosol records in the northern Harz foreland, Germany, based on innovative modelling tools. Boreas 50, 746-763, http://doi.org/10.1111/bor.12510

Tian, S., Sun, J., Zhang, Z., Abdulov, S., Cao, M., Gadoev, M., Oimahmadov, I., 2021. Loess deposits in the Tajik Basin, Central Asia: chronology, provenance and palaeoclimatic implications since the Last Glacial. Boreas 50, 147-166, http://doi.org/10.1111/bor.12467

Van Balen, R.T., Kasse, C., Wallinga, J., Woolderink, H.A.G., 2021. Middle to Late Pleistocene faulting history of the Heerlerheide fault, Roer Valley Rift System, influenced by glacio-isostasy and mining-induced displacement. Quaternary Science Reviews 268, 107111, http://doi.org/10.1016/j.quascirev.2021.107111

Waroszewski, J., Pietranik, A., Sprafke, T., Kabała, C., Frechen, M., Jary, Z., Kot, A., Tsukamoto, S., Meyer-Heintze, S., Krawczyk, M., Łabaz, B., Schultz, B., Erban Kochergina, Y.V., 2021. Provenance and paleoenvironmental context of the Late Pleistocene thin aeolian silt mantles in southwestern Poland – A widespread parent material for soils. CATENA 204, 105377, http://doi.org/10.1016/j.catena.2021.105377

Wu, D., Zhang, C., Wang, T., Liu, L., Zhang, X., Yuan, Z., Yang, S., Chen, F., 2021. East-west asymmetry in the distribution of rainfall in the Chinese Loess Plateau during the Holocene. CATENA 207, 105626, http://doi.org/10.1016/j.catena.2021.105626

Yang, J., Xia, D., Gao, F., Wang, S., Li, D., Fan, Y., Chen, Z., Tian, W., Liu, X., Sun, X., Wang, Z., Wang, F., 2021. Holocene moisture evolution and its response to atmospheric circulation recorded by aeolian deposits in the southern Tibetan Plateau. Quaternary Science Reviews 270, 107169, http://doi.org/10.1016/j.quascirev.2021.107169

- marine

West, G., Alexanderson, H., Jakobsson, M., O'Regan, M., 2021. Optically stimulated luminescence dating supports pre-Eemian age for glacial ice on the Lomonosov Ridge off the East Siberian continental shelf. Quaternary Science Reviews 267, 107082, http://doi.org/10.1016/j.quascirev.2021.107082

- soil

Persico, L.P., McFadden, L.D., McAuliffe, J.R., Rittenour, T.M., Stahlecker, T.E., Dunn, S.B., Brody, S.A.T., 2021. Late Quaternary geochronologic record of soil formation and erosion: Effects of climate change on Mojave Desert hillslopes (Nevada, USA). Geology 50, 54-59, http://doi.org/10.1130/G49270.1

Plata, J.M., Rodríguez, R., Preusser, F., Boixadera, J., Balasch, J.C., Antúnez, M., Poch, R.M., 2021. Red soils in loess deposits of the Eastern Ebro Valley. CATENA 204, 105430, http://doi.org/10.1016/j.catena.2021.105430

Yeo, E.-Y., Choi, J.-H., Ahn, U.S., Cheong, A.C.-s., 2019. Quartz OSL dating of palaeosols intercalated with basaltic lava flows and scoria deposits from monogenetic volcanoes in northeastern Jeju Island, Korea. Geosciences Journal 23, 881-894, http://doi.org/10.1007/s12303-019-0010-2

- surface exposure dating

Ageby, L., Angelucci, D.E., Brill, D., Carrer, F., Rades, E.F., Rethemeyer, J., Brückner, H., Klasen, N., 2021. Rock surface IRSL dating of buried cobbles from an alpine dry-stone structure in Val di Sole, Italy. Quaternary Geochronology 66, 101212, http://doi.org/10.1016/j.quageo.2021.101212

Gliganic, L.A., Meyer, M.C., May, J.-H., Aldenderfer, M.S., Tropper, P., 2021. Direct dating of lithic surface artifacts using luminescence. Science Advances 7, eabb3424, http://doi.org/10.1126/sciadv.abb3424

Ishii, Y., Takahashi, T., Ito, K., 2022. Luminescence dating of cobbles from Pleistocene fluvial terrace deposits of the Ara River, Japan. Quaternary Geochronology 67, 101228, http://doi.org/10.1016/j.quageo.2021.101228

Sellwood, E.L., Kook, M., Jain, M., 2022. Rapid in situ assessment of luminescence-bleaching depths for deriving burial and exposure chronologies of rock surfaces. Quaternary Geochronology 67, 101227, http://doi.org/10.1016/j.quageo.2021.101227

Smedley, R.K., Small, D., Jones, R.S., Brough, S., Bradley, J., Jenkins, G.T.H., 2021. Erosion rates in a wet, temperate climate derived from rock luminescence techniques. Geochronology 3, 525-543, http://doi.org/10.5194/gchron-3-525-2021

Souza, P.E., Sohbati, R., Murray, A.S., Clemmensen, L.B., Kroon, A., Nielsen, L., 2021. Optical dating of cobble surfaces determines the chronology of Holocene beach ridges in Greenland. Boreas 50, 606-618, http://doi.org/10.1111/bor.12507

- tephra (and volcanic related)

Engel, M., Dotterweich, M., Fülling, A., Brill, D., Broisch-Höhner, M., Totschnig, R., Seren, S., Kehl, M., 2021. Syn- and post-eruptive gully formation near the Laacher See volcano. Earth Surface Processes and Landforms 46, 1783-1796, http://doi.org/10.1002/esp.5119

Sontag-González, M., Li, B., O'Gorman, K., Sutikna, T., Jatmiko, Jacobs, Z., Roberts, R.G., 2021. Establishing a pIRIR procedure for De determination of composite mineral grains from volcanic terranes: A case study of sediments from Liang Bua, Indonesia. Quaternary Geochronology 65, 101181, http://doi.org/10.1016/j.quageo.2021.101181

- thermochronology

Bouscary, C., King, G.E., 2022. Luminescence thermochronometry of feldspar minerals: Optimisation of measurement conditions for the derivation of thermal kinetic parameters using isothermal holding experiments. Quaternary Geochronology 67, 101240, http://doi.org/10.1016/j.quageo.2021.101240

Archaeology applications

Ageby, L., Angelucci, D.E., Brill, D., Carrer, F., Rades, E.F., Rethemeyer, J., Brückner, H., Klasen, N., 2021. Rock surface IRSL dating of buried cobbles from an alpine dry-stone structure in Val di Sole, Italy. Quaternary Geochronology 66, 101212, http://doi.org/10.1016/j.quageo.2021.101212

Avni, Y., Oron, M., Cohen-Sasson, E., Porat, N., Barzilai, O., 2021. Chrono-sequences of alluvial terraces and fossilized water bodies as a predictive model for detecting Lower and Middle Palaeolithic sites in the Negev desert, Israel. Quaternary Science Reviews 268, 107114, http://doi.org/10.1016/j.quascirev.2021.107114

Bahain, J.-J., Mercier, N., Valladas, H., Falguères, C., Masaoudi, H., Joron, J.-L., Froget, L., Moigne, A.-M., Combier, J., Moncel, M.-H., 2022. Reappraisal of the chronology of Orgnac 3 Lower-to-Middle Paleolithic site (Ardèche, France), a regional key sequence for the Middle Pleistocene of southern France. Journal of Human Evolution 162, 103092, http://doi.org/10.1016/j.jhevol.2021.103092

Cheng, T., Zhang, D., Smith, G.M., Jöris, O., Wang, J., Yang, S., Xia, H., Shen, X., Li, Q., Chen, X., Lin, D., Han, Y., Liu, Y., Qiang, M., Li, B., Chen, F., 2021. Hominin occupation of the Tibetan Plateau during the Last Interglacial Complex. Quaternary Science Reviews 265, 107047, http://doi.org/10.1016/j.quascirev.2021.107047

Chu, W., Pötter, S., Doboș, A., Albert, T., Klasen, N., Ciornei, A., Bösken, J.J., Schulte, P., 2019. Geoarchaeology and geochronology of the Upper Palaeolithic site of Temerești Dealu Vinii, Banat, Romania: Site formation processes and human activity of an open-air locality. Quartär 66, 111-134, http://doi.org/10.7485/QU66_5

Colton, D., Whitfield, E., Plater, A.J., Duller, G.A.T., Jain, M., Barham, L., 2021. New geomorphological and archaeological evidence for drainage evolution in the Luangwa Valley (Zambia) during the Late Pleistocene. Geomorphology 392, 107923, http://doi.org/10.1016/j.geomorph.2021.107923

Daura, J., Sanz, M., Demuro, M., Arnold, L.J., Costa, A.M., Moreno, J., da Conceição Freitas, M., Lopes, V., Égüez, N., Hoffmann, D.L., Benson, A., Cabanes, D., García-Targa, J., Fullola, J.M., 2021. A new chronological framework and site formation history for Cova del Gegant (Barcelona): Implications for Neanderthal and Anatomically Modern Human occupation of NE Iberian Peninsula. Quaternary Science Reviews 270, 107141, http://doi.org/10.1016/j.quascirev.2021.107141

Eren, M.I., Meltzer, D.J., Andrews, B.N., 2021. Clovis Technology is not Unique to Clovis. PaleoAmerica 7, 226-241, http://doi.org/10.1080/20555563.2021.1890402

Gliganic, L.A., Meyer, M.C., May, J.-H., Aldenderfer, M.S., Tropper, P., 2021. Direct dating of lithic surface artifacts using luminescence. Science Advances 7, eabb3424, http://doi.org/10.1126/sciadv.abb3424

Hein, M., Urban, B., Tanner, D.C., Buness, A.H., Tucci, M., Hoelzmann, P., Dietel, S., Kaniecki, M., Schultz, J., Kasper, T., von Suchodoletz, H., Schwalb, A., Weiss, M., Lauer, T., 2021. Eemian landscape response to climatic shifts and evidence for northerly Neanderthal occupation at a palaeolake margin in northern Germany. Earth Surface Processes and Landforms 46, 2884-2901, http://doi.org/10.1002/esp.5219

Jin, J., Cai, X., Huang, Y., Zuo, X., Ling, Z., Dai, J., Ren, Y., Zhang, W., Li, S., 2021. New luminescence dating evidence reveals the timing of Neolithic human activities in Fuzhou Basin, South China. CATENA 207, 105590, http://doi.org/10.1016/j.catena.2021.105590

Jin, J.-h., Wang, X.-y., Zhou, Z.-y., Huang, Y.-m., Fan, X.-c., Zuo, X.-x., Li, Z.-z., Ling, Z.-y., Ren, Y.-q., Li, S.-t., 2021. OSL chronology of a Palaeolithic site in a humid subtropical mountainous area of southeast China. Journal of Mountain Science 18, 2012-2023, http://doi.org/10.1007/s11629-021-6701-y

Knabb, K.A., 2019. Human and environmental impacts of ancient copper metallurgy: A case study from southern Jordan. Current Anthropology 60, 840-848, http://doi.org/10.1086/706543

Kreutzer, S., Valladas, H., Texier, P.-J., Moineau, V., Mologni, C., Mercier, N., 2021. The Mousterian loess sequence La Combette (France) and its chronological framework: A re-investigation. Comptes Rendus Palevol 20, 225-252, http://doi.org/10.5852/cr-palevol2021v20a14

Lisá, L., Mohammadi, S., Goláňová, P., Hajnalová, M., Bajer, A., Moska, P., Rohovec, J., Král, P., Kysela, J., Kočárová, R., 2022. Detection of occupational surface remnants at a heavily eroded site; case study of archaeological soils from La Terrasse, Bibracte oppidum. CATENA 210, 105911, http://doi.org/10.1016/j.catena.2021.105911

Marsh, E.J., Korpisaari, A., Puerto Mundt, S., Gasco, A., Durán, V., 2021. Radiocarbon vs. Luminescence dating of archaeological ceramics in the southern andes: A review of paired dates, bayesian models, and a pilot study. Radiocarbon 63, 1471-1501, http://doi.org/10.1017/RDC.2021.82

Michalec, G., Cendrowska, M., Andrieux, E., Armitage, S.J., Ehlert, M., Kim, J.Y., Sohn, Y.K., Krupa-Kurzynowska, J., Moska, P., Szmit, M., Masojć, M., 2021. A Window into the Early–Middle Stone Age Transition in Northeastern Africa—A Marine Isotope Stage 7a/6 Late Acheulean Horizon from the EDAR 135 Site, Eastern Sahara (Sudan). Journal of Field Archaeology 46, 513-533, http://doi.org/10.1080/00934690.2021.1993618

Nett, J.J., Chu, W., Fischer, P., Hambach, U., Klasen, N., Zeeden, C., Obreht, I., Obrocki, L., Pötter, S., Gavrilov, M.B., Vött, A., Mihailović, D., Marković, S.B., Lehmkuhl, F., 2021. The Early Upper Paleolithic Site Crvenka-At, Serbia–The First Aurignacian Lowland Occupation Site in the Southern Carpathian Basin. Frontiers in Earth Science 9, http://doi.org/10.3389/feart.2021.599986

Osypiński, P., Burrough, S., Skinner, A., Standzikowski, K., 2021. Re-examining the age of the Affad MSA deposits in the Middle Nile Valley. Archaeometry 63, 1405-1420, http://doi.org/10.1111/arcm.12670

Price, G.J., Fitzsimmons, K.E., Nguyen, A.D., Zhao, J.-x., Feng, Y.-x., Sobbe, I.H., Godthelp, H., Archer, M., Hand, S.J., 2021. New ages of the world's largest-ever marsupial: Diprotodon optatum from Pleistocene Australia. Quaternary International 603, 64-73, http://doi.org/10.1016/j.quaint.2021.06.013

Richard, M., Pons-Branchu, E., Genuite, K., Jaillet, S., Joannes-Boyau, R., Wang, N., Genty, D., Cheng, H., Price, G.J., Pierre, M., Dapoigny, A., Falguères, C., Tombret, O., Voinchet, P., Bahain, J.-J., Moncel, M.-H., 2021. Timing of Neanderthal occupations in the southeastern margins of the Massif Central (France): A multi-method approach. Quaternary Science Reviews 273, 107241, http://doi.org/10.1016/j.quascirev.2021.107241

Val, A., de la Peña, P., Duval, M., Bansal, S., Colino, F., Culey, J., Hodgskiss, T., Morrissey, P., Murray, A., Murungi, M., Neumann, F.H., Shadrach, K., Thomsen, K.J., van der Ryst, M., Witelson, D.M., Zhao, J.X., Stratford, D., 2021. The place beyond the trees: renewed excavations of the Middle Stone Age deposits at Olieboomspoort in the Waterberg Mountains of the South African Savanna Biome. Archaeological and Anthropological Sciences 13, 116, http://doi.org/10.1007/s12520-021-01302-7

Wang, F., Guo, Y., Xian, Q., Li, M., Rui, X., Xie, F., 2021. Luminescence chronology for the Paleolithic site of Xinmiaozhuang Locality 1 (XMZ1) in the Nihewan Basin, northern China, and its paleoenvironmental and archaeological implications. Journal of Human Evolution 157, 103033, http://doi.org/10.1016/j.jhevol.2021.103033

Zaidner, Y., Centi, L., Prévost, M., Mercier, N., Falguères, C., Guérin, G., Valladas, H., Richard, M., Galy, A., Pécheyran, C., Tombret, O., Pons-Branchu, E., Porat, N., Shahack-Gross, R., Friesem, D.E., Yeshurun, R., Turgeman-Yaffe, Z., Frumkin, A., Herzlinger, G., Ekshtain, R., Shemer, M., Varoner, O., Sarig, R., May, H., Hershkovitz, I., 2021. Middle Pleistocene Homo behavior and culture at 140,000 to 120,000 years ago and interactions with Homo sapiens. Science 372, 1429-1433, http://doi.org/10.1126/science.abh3020

Zhao, X., Sheisha, H., Thomas, I., Salem, A., Sun, Q., Liu, Y., Mashaly, H., Nian, X., Chen, J., Finlayson, B., Chen, Z., 2021. Climate-driven early agricultural origins and development in the Nile Delta, Egypt. Journal of Archaeological Science 136, 105498, http://doi.org/10.1016/j.jas.2021.105498

Zilhão, J., Angelucci, D.E., Arnold, L.J., d'Errico, F., Dayet, L., Demuro, M., Deschamps, M., Fewlass, H., Gomes, L., Linscott, B., Matias, H., Pike, A.W.G., Steier, P., Talamo, S., Wild, E.M., 2021. Revisiting the Middle and Upper Palaeolithic archaeology of Gruta do Caldeirão (Tomar, Portugal). PLOS ONE 16, e0259089, http://doi.org/10.1371/journal.pone.0259089

Various ESR applications

Bahain, J.-J., Mercier, N., Valladas, H., Falguères, C., Masaoudi, H., Joron, J.-L., Froget, L., Moigne, A.-M., Combier, J., Moncel, M.-H., 2022. Reappraisal of the chronology of Orgnac 3 Lower-to-Middle Paleolithic site (Ardèche, France), a regional key sequence for the Middle Pleistocene of southern France. Journal of Human Evolution 162, 103092, http://doi.org/10.1016/j.jhevol.2021.103092

Costa Ribeiro, R.d., Kinoshita, A., Araújo-Júnior, H.I.d., Figueiredo, A.M.G., Souza Carvalho, I.d., Baffa, O., 2021. ESR dating of Toxodon teeth from Baixa Grande, Bahia, Brazil. Journal of South American Earth Sciences 112, 103616, http://doi.org/10.1016/j.jsames.2021.103616

Gobindlal, K., Zujovic, Z., Yadav, P., Sperry, J., Weber, C.C., 2021. The Mechanism of Surface-Radical Generation and Amorphization of Crystalline Quartz Sand upon Mechanochemical Grinding. The Journal of Physical Chemistry C 125, 20877-20886, http://doi.org/10.1021/acs.jpcc.1c06069

Gouveia, M.P., Cunha, P.P., Falguères, C., Voinchet, P., Martins, A.A., Bahain, J.-J., Pereira, A., 2020. Electron spin resonance dating of the culminant allostratigraphic unit of the Mondego and Lower Tejo Cenozoic basins (W Iberia), which predates fluvial incision into the basin-fill sediments. Global and Planetary Change 184, 103081, http://doi.org/10.1016/j.gloplacha.2019.103081

Lewis, S.G., Ashton, N., Davis, R., Hatch, M., Hoare, P.G., Voinchet, P., Bahain, J.-J., 2021. A revised terrace stratigraphy and chronology for the early Middle Pleistocene Bytham River in the Breckland of East Anglia, UK. Quaternary Science Reviews 269, 107113, http://doi.org/10.1016/j.quascirev.2021.107113

Lopes, R.P., Pereira, J.C., Kinoshita, A., Mollemberg, M., Barbosa, F., Baffa, O., 2020. Geological and taphonomic significance of electron spin resonance (ESR) ages of Middle-Late Pleistocene marine shells from barrier-lagoon systems of Southern Brazil. Journal of South American Earth Sciences 101, 102605, http://doi.org/10.1016/j.jsames.2020.102605

Ma, X., Yin, G., Wei, C., Qiang, X., Ma, Y., Liu, C., Zhao, Z., Gong, L., Wang, L., Ji, H., Bai, M., Mao, J., Li, G., 2022. High-resolution late Pliocene-quaternary magnetostratigraphy of the Yinchuan Basin, NE Tibetan Plateau. Quaternary International 607, 120-127, http://doi.org/10.1016/j.quaint.2021.09.009

Monti, A.M., Buryi, M., Fasoli, M., Martini, M., 2021. Anomalous thermal stability of the [GeO4]- Electron Paramagnetic Resonance signal and the 110 °C Thermally Stimulated Luminescence peak in natural and synthetic quartz. Journal of Luminescence 238, 118263, http://doi.org/10.1016/j.jlumin.2021.118263

Monti, A.M., Buryi, M., Fasoli, M., Martini, M., 2021. EPR characterization in natural quartz samples of a newly discovered hydrogen related defect and already known germanium related defects. Radiation Measurements 145, 106604, http://doi.org/10.1016/j.radmeas.2021.106604

Moreno, D., Gutiérrez, F., Val, M.d., Carbonel, D., Jiménez, F., Jesús Alonso, M., Martínez-Pillado, V., Guzmán, O., López, G.I., Martínez, D., 2021. A multi-method dating approach to reassess the geochronology of faulted Quaternary deposits in the central sector of the Iberian Chain (NE Spain). Quaternary Geochronology 65, 101185, http://doi.org/10.1016/j.quageo.2021.101185

Osypiński, P., Burrough, S., Skinner, A., Standzikowski, K., 2021. Re-examining the age of the Affad MSA deposits in the Middle Nile Valley. Archaeometry 63, 1405-1420, http://doi.org/10.1111/arcm.12670

Parés, J.M., Duval, M., Soria-Jáuregui, A., González-Amuchástegui, M.J., 2021. First chronological constraints for the high terraces of the Upper Ebro Catchment. Quaternary 4, 25, https://www.mdpi.com/2571-550X/4/3/25

Rashad, A.M., Helal, A.E.I., Ahmed, G., Kassem, S., Fahim, R., Salem, S., Mohamed, S.E.-D., Gamal, A., 2020. Spectroscopic analysis of irradiated natural quartz and ESR dating aspects. Arab Journal of Nuclear Sciences and Applications 53, 197-209, http://doi.org/10.21608/ajnsa.2020.22502.1321

Richard, M., Pons-Branchu, E., Genuite, K., Jaillet, S., Joannes-Boyau, R., Wang, N., Genty, D., Cheng, H., Price, G.J., Pierre, M., Dapoigny, A., Falguères, C., Tombret, O., Voinchet, P., Bahain, J.-J., Moncel, M.-H., 2021. Timing of Neanderthal occupations in the southeastern margins of the Massif Central (France): A multi-method approach. Quaternary Science Reviews 273, 107241, http://doi.org/10.1016/j.quascirev.2021.107241

Tsukamoto, S., Oppermann, F., Autzen, M., Richter, M., Bailey, M., Ankjærgaard, C., Jain, M., 2021. Response of the Ti and Al electron spin resonance signals in quartz to X-ray irradiation. Radiation Measurements 149, 106676, http://doi.org/10.1016/j.radmeas.2021.106676

Val, A., de la Peña, P., Duval, M., Bansal, S., Colino, F., Culey, J., Hodgskiss, T., Morrissey, P., Murray, A., Murungi, M., Neumann, F.H., Shadrach, K., Thomsen, K.J., van der Ryst, M., Witelson, D.M., Zhao, J.X., Stratford, D., 2021. The place beyond the trees: renewed excavations of the Middle Stone Age deposits at Olieboomspoort in the Waterberg Mountains of the South African Savanna Biome. Archaeological and Anthropological Sciences 13, 116, http://doi.org/10.1007/s12520-021-01302-7

Zaidner, Y., Centi, L., Prévost, M., Mercier, N., Falguères, C., Guérin, G., Valladas, H., Richard, M., Galy, A., Pécheyran, C., Tombret, O., Pons-Branchu, E., Porat, N., Shahack-Gross, R., Friesem, D.E., Yeshurun, R., Turgeman-Yaffe, Z., Frumkin, A., Herzlinger, G., Ekshtain, R., Shemer, M., Varoner, O., Sarig, R., May, H., Hershkovitz, I., 2021. Middle Pleistocene Homo behavior and culture at 140,000 to 120,000 years ago and interactions with Homo sapiens. Science 372, 1429-1433, http://doi.org/10.1126/science.abh3020

Basic research

Alharshan, G.A., 2021. Thermoluminescence sensitivity assessment of the natural schist rock through pre-dose effect technique. Arabian Journal of Geosciences 14, 1917, http://doi.org/10.1007/s12517-021-07091-6

Autzen, M., Guérin, G., Murray, A.S., Jain, M., Buylaert, J.P., 2021. Comparing natural and laboratory irradiations: A simulation approach. Journal of Luminescence 238, 118272, http://doi.org/10.1016/j.jlumin.2021.118272

Bailiff, I.K., Bridgland, D., Cunha, P.P., 2021. Extending the range of optically stimulated luminescence dating using vein-quartz and quartzite sedimentary pebbles. Quaternary Geochronology 65, 101180, http://doi.org/10.1016/j.quageo.2021.101180

Clark-Balzan, L., May, V.R., Preusser, F., 2021. Luminescence characteristics of intraplate-derived olivines. Geochronometria 48, 73-94, http://doi.org/10.2478/geochr-2021-0006

Fitzsimmons, K.E., Perić, Z., Nowatzki, M., Lindauer, S., Vinnepand, M., Prud'homme, C., Dave, A.K., Vött, A., Fischer, P., 2022. Luminescence Sensitivity of Rhine Valley Loess: Indicators of Source Variability? Quaternary 5, http://doi.org/10.3390/quat5010001

Folley, D.E., Chithambo, M.L., 2021. Analysis of thermoluminescence and phosphorescence related to phototransfer in natural quartz. Journal of Luminescence 238, 118217, http://doi.org/10.1016/j.jlumin.2021.118217

Gobindlal, K., Zujovic, Z., Yadav, P., Sperry, J., Weber, C.C., 2021. The Mechanism of Surface-Radical Generation and Amorphization of Crystalline Quartz Sand upon Mechanochemical Grinding. The Journal of Physical Chemistry C 125, 20877-20886, http://doi.org/10.1021/acs.jpcc.1c06069

Konstantinidis, P., Kioumourtzoglou, S., Polymeris, G.S., Kitis, G., 2021. Stimulated luminescence; Analysis of complex signals and fitting of dose response curves using analytical expressions based on the Lambert W function implemented in a commercial spreadsheet. Applied Radiation and Isotopes 176, 109870, http://doi.org/10.1016/j.apradiso.2021.109870

Lawless, J.L., Chen, R., Pagonis, V., 2021. A model explaining the inability of exciting thermoluminescence (TL) peaks in certain low temperature ranges. Radiation Measurements 145, 106610, http://doi.org/10.1016/j.radmeas.2021.106610

Li, B., Jacobs, Z., Roberts, R.G., 2022. Bayesian analysis of De distributions in optical dating: Towards a robust method for dealing with outliers. Quaternary Geochronology 67, 101230, http://doi.org/10.1016/j.quageo.2021.101230

Madden, L., Lukas, E., Santos, A., Ganija, M., Veitch, P., Rosenfeld, A., Li, E., 2021. Deconvolution analysis improves real-time OSL of BeO ceramic. Radiation Measurements 149, 106680, http://doi.org/10.1016/j.radmeas.2021.106680

Mauz, B., Martin, L., Discher, M., Tribolo, C., Kreutzer, S., Bahl, C., Lang, A., Mercier, N., 2021. Technical note: On the reliability of laboratory beta-source calibration for luminescence dating. Geochronology 3, 371-381, http://doi.org/10.5194/gchron-3-371-2021

Monti, A.M., Buryi, M., Fasoli, M., Martini, M., 2021. Anomalous thermal stability of the [GeO4]- Electron Paramagnetic Resonance signal and the 110 °C Thermally Stimulated Luminescence peak in natural and synthetic quartz. Journal of Luminescence 238, 118263, http://doi.org/10.1016/j.jlumin.2021.118263

Monti, A.M., Buryi, M., Fasoli, M., Martini, M., 2021. EPR characterization in natural quartz samples of a newly discovered hydrogen related defect and already known germanium related defects. Radiation Measurements 145, 106604, http://doi.org/10.1016/j.radmeas.2021.106604

Mueller, D., Preusser, F., 2022. Investigating the applicability of a standardised growth curve approach on Middle Pleistocene sediments from northern Switzerland. Quaternary Geochronology 67, 101238, http://doi.org/10.1016/j.quageo.2021.101238

Peng, J., Sadek, A.M., Kitis, G., 2021. New analytical expressions derived from the localized transition model for luminescence stimulation modes of TL and LM-OSL and their applications in computerized curve deconvolution. Nuclear Instruments and Methods in Physics Research Section B: Beam Interactions with Materials and Atoms 507, 46-57, http://doi.org/10.1016/j.nimb.2021.09.012

Peng, J., Wang, X., Adamiec, G., 2022. The build-up of the laboratory-generated dose-response curve and underestimation of equivalent dose for quartz OSL in the high dose region: A critical modelling study. Quaternary Geochronology 67, 101231, http://doi.org/10.1016/j.quageo.2021.101231

Rahimzadeh, N., Tsukamoto, S., Zhang, J., Long, H., 2021. Natural and laboratory dose response curves of quartz violet stimulated luminescence (VSL): Exploring the multiple aliquot regenerative dose (MAR) protocol. Quaternary Geochronology 65, 101194, http://doi.org/10.1016/j.quageo.2021.101194

Riedesel, S., Kumar, R., Duller, G.A.T., Roberts, H.M., Bell, A.M.T., Jain, M., 2021. Site-selective characterisation of electron trapping centres in relation to chemistry, structural state and mineral phases present in single crystal alkali feldspars. Journal of Physics D: Applied Physics 54, 385107, http://doi.org/10.1088/1361-6463/ac10d7

Sabry, M., Alazab, H.A., Gad, A., El-Faramawy, N., 2021. Thermoluminescence properties of natural Egyptian calcite. Journal of Luminescence 238, 118273, http://doi.org/10.1016/j.jlumin.2021.118273

Sipos, G., Schmidt, C., Bartyik, T., Filyó, D., Magyar, G., Havasi, V., Kukovecz, Á., 2021. Cross-calibration of an α-source used for luminescence dating by applying different samples and procedures. Geochronometria 48, 61-72, http://doi.org/10.2478/geochr-2021-0003

Tsukamoto, S., Oppermann, F., Autzen, M., Richter, M., Bailey, M., Ankjærgaard, C., Jain, M., 2021. Response of the Ti and Al electron spin resonance signals in quartz to X-ray irradiation. Radiation Measurements 149, 106676, http://doi.org/10.1016/j.radmeas.2021.106676

Beyond quartz and K-feldspar: non-traditional minerals

- Calcite

Sabry, M., Alazab, H.A., Gad, A., El-Faramawy, N., 2021. Thermoluminescence properties of natural Egyptian calcite. Journal of Luminescence 238, 118273, http://doi.org/10.1016/j.jlumin.2021.118273

- Flint

Zaidner, Y., Centi, L., Prévost, M., Mercier, N., Falguères, C., Guérin, G., Valladas, H., Richard, M., Galy, A., Pécheyran, C., Tombret, O., Pons-Branchu, E., Porat, N., Shahack-Gross, R., Friesem, D.E., Yeshurun, R., Turgeman-Yaffe, Z., Frumkin, A., Herzlinger, G., Ekshtain, R., Shemer, M., Varoner, O., Sarig, R.,

May, H., Hershkovitz, I., 2021. Middle Pleistocene Homo behavior and culture at 140,000 to 120,000 years ago and interactions with Homo sapiens. Science 372, 1429-1433, http://doi.org/10.1126/science.abh3020

- Meteorite

Rosén, Å.V., Hofmann, B.A., Preusser, F., Gnos, E., Eggenberger, U., Schumann, M., Szidat, S., 2021. Meteorite terrestrial ages in Oman based on gamma spectrometry and sediment dating, focusing on the Ramlat Fasad dense collection area. Meteoritics & Planetary Science 56, 2017-2034, http://doi.org/10.1111/maps.13758

- Olivine

Clark-Balzan, L., May, V.R., Preusser, F., 2021. Luminescence characteristics of intraplate-derived olivines. Geochronometria 48, 73-94, http://doi.org/10.2478/geochr-2021-0006

Dose rate issues

Marques, R., Prudêncio, M.I., Russo, D., Cardoso, G., Dias, M.I., Rodrigues, A.L., Reis, M., Santos, M., Rocha, F., 2021. Evaluation of naturally occurring radionuclides (K, Th and U) in volcanic soils from Fogo Island, Cape Verde. Journal of Radioanalytical and Nuclear Chemistry 330, 347-355, http://doi.org/10.1007/s10967-021-07959-7

Tudyka, K., Poręba, G., Szymak, A., Rocznik, J., Pluta, J., Schüler, T., Kolb, T., Murray, A., 2021. Systematic error in 238U decay chain radionuclides measurements due to 222Rn emanation from reference materials. Measurement 184, 109893, http://doi.org/10.1016/j.measurement.2021.109893

Dosimetry

Discher, M., Eakins, J., Woda, C., Tanner, R., 2021. Translation of the absorbed dose in the mobile phone to organ doses of an ICRP voxel phantom using MCNPX simulation of an Ir-192 point source. Radiation Measurements 146, 106603, http://doi.org/10.1016/j.radmeas.2021.106603

Kalita, J.M., Kaya-Keleş, Ş., Çakal, G.Ö., Meriç, N., Polymeris, G.S., 2022. Thermoluminescence and optically stimulated luminescence of colemanite-rich borate mineral. Journal of Luminescence 242, 118580, http://doi.org/10.1016/j.jlumin.2021.118580

Kim, H., Discher, M., Kim, M.C., Woda, C., Lee, J., 2021. Thermally assisted optically stimulated luminescence protocol of mobile phone substrate glasses for accident dosimetry. Radiation Measurements 146, 106625, http://doi.org/10.1016/j.radmeas.2021.106625

Knežević, Ž., Majer, M., Baranowska, Z., Bjelac, O.C., Iurlaro, G., Kržanović, N., Mariotti, F., Nodilo, M., Neumaier, S., Wołoszczuk, K., Živanović, M., 2021. Investigations into the basic properties of different passive dosimetry systems used in environmental radiation monitoring in the aftermath of a nuclear or radiological event. Radiation Measurements 146, 106615, http://doi.org/10.1016/j.radmeas.2021.106615

Madden, L., Lukas, E., Santos, A., Ganija, M., Veitch, P., Rosenfeld, A., Li, E., 2021. Deconvolution analysis improves real-time OSL of BeO ceramic. Radiation Measurements 149, 106680, http://doi.org/10.1016/j.radmeas.2021.106680

Malletzidou, L., Polymeris, G.S., Sfampa, I.K., Stoulos, S., Paraskevopoulos, K.M., Kitis, G., 2021. Methodological aspects and practical limitations for luminescence dating applications in calcium sulfate samples implied by dose response and dose recovery measurements. Microchemical Journal 168, 106382, http://doi.org/10.1016/j.microc.2021.106382

Pagonis, V., Woda, C., Discher, M., 2021. Quantitative analysis of thermoluminescence signals of glass displays from mobile phones. Radiation Measurements 146, 106614, http://doi.org/10.1016/j.radmeas.2021.106614

Sholom, S., McKeever, S.W.S., 2021. A non-destructive, high-sensitivity, emergency dosimetry method using OSL from protective back-glasses from smartphones. Radiation Measurements 147, 106646, http://doi.org/10.1016/j.radmeas.2021.106646

Tchakoua Tchouaso, M., Coon, N., Hayes, R.B., 2021. An effectively nondestructive method for dose assessment from accidental exposure using PCBs from electronic watches. Radiation Measurements 148, 106648, http://doi.org/10.1016/j.radmeas.2021.106648

Yasmin, S., Khandaker, M.U., Nawi, S.N.M., Sani, S.F.A., Bradley, D.A., Islam, M.A., 2021. The potential of decorative building materials (marble) for retrospective thermoluminescence dosimetry. Applied Radiation and Isotopes 175, 109782, http://doi.org/10.1016/j.apradiso.2021.109782

Portable instruments

Serra, E., Valla, P.G., Gribenski, N., Guedes Magrani, F., Carcaillet, J., Delaloye, R., Grobéty, B., Braillard, L., 2021. Geomorphic response to the Lateglacial–Holocene transition in high Alpine regions (Sanetsch Pass, Swiss Alps). Boreas 50, 242-261, http://doi.org/10.1111/bor.12480

Computer coding

Konstantinidis, P., Kioumourtzoglou, S., Polymeris, G.S., Kitis, G., 2021. Stimulated luminescence; Analysis of complex signals and fitting of dose response curves using analytical expressions based on the Lambert W function implemented in a commercial spreadsheet. Applied Radiation and Isotopes 176, 109870, http://doi.org/10.1016/j.apradiso.2021.109870

Review

Liritzis, I., Laskaris, N., A., V., I., K., Volonakis, P., Papageorgopoulou, C., Bratitsi, M., 2020. Archaeometry: an overview. Scientific Culture 6, 49-98, http://doi.org/10.5281/zenodo.3625220

Marin, L.C., Forman, S.L., Todd, V.T., Mayhack, C., Gonzalez, A., Liang, P., 2021. Isolation of quartz grains for optically stimulated luminescence (OSL) dating of Quaternary sediments for paleoenvironmental research. Journal of Visualized Experiments, e62706, http://doi.org/10.3791/62706

Murray, A., Arnold, L.J., Buylaert, J.-P., Guérin, G., Qin, J., Singhvi, A.K., Smedley, R., Thomsen, K.J., 2021. Optically stimulated luminescence dating using quartz. Nature Reviews Methods Primers 1, 72, http://doi.org/10.1038/s43586-021-00068-5

Stone, A., Fenn, K., 2020. Dating Aeolian Deposits, Reference Module in Earth Systems and Environmental Sciences. Elsevier, http://doi.org/10.1016/B978-0-12-818234-5.00016-X

Townsend, P.D., Wang, Y., McKeever, S.W.S., 2021. Spectral evidence for defect clustering: Relevance to radiation dosimetry materials. Radiation Measurements 147, 106634, http://doi.org/10.1016/j.radmeas.2021.106634

Conference Announcements:
14th New World Luminescence Dating & Dosimetry Workshop

Obituary: Dr. Bonnie Anne Blickstein Blackwell (1955 – 2021)

Dr. Bonnie Anne Blickstein Blackwell
1955 – 2021

Bonnie Blackwell, geoarchaeologist extraordinare, died in New York, September 8, 2021, aged 66. She was born April 8, 1955, in the small town of Paris, Ontario. In an interview a few years ago she noted that her first four years of school were in a one-room schoolhouse! At the age of 11, she saw a program on Louis Leakey and decided to be an archaeologist. The many people who knew Bonnie will not be surprised that she never wavered from this goal. She received her B.A. in anthropology from McMaster University in 1978 and her M.Sc. in geology in 1980, studying U-Series dating under Prof. Henry Schwarcz. Henry tells the story of meeting her:

> "When Bonnie Blackwell was a junior in anthropology at McMaster University in Hamilton, Ontario, Canada, I gave a talk in one of her classes on the use of uranium series dating in archaeology. Something clicked in Bonnie's head and she came to visit me in the Dept of Geology to see if she could do a bachelor's thesis on this topic. I had never supervised an undergrad before and especially one with so little background in science. But she jumped on the project of dating archaeological sites in Israel using samples I had collected, learned the techniques of U series dating and soon was a proficient and careful analyst. We wrote our first paper together in 1979 and she submitted a B.A. thesis about 150 pages long covering every historical aspect of the topic!"

Her Ph.D. from the University of Alberta in 1987 dealt with amino acid racemization. She then returned to McMaster for post-doctoral work with Henry, at which time she began her research using electron spin resonance (ESR) as a dating technique. We met at a conference in 1993 and began to collaborate two years later.

Almost all of her professional work, including roughly 150 contributions to journals and books, many, many conference presentations, and several technical manuals, relates to ESR dating. Within that one must note that she studied a wide variety of materials and sites, and answered many different questions, not just "How old?". Her projects came from every continent except Antarctica. For most of them, she was both excavator and analyst. A complete description of all of them is beyond the scope of this memorial. They can be grouped in four major categories.

First are her studies in human evolution. These included early hominins in the South African Cradle of Humanity, and the Acheulian in India. She also looked at questions relevant to the "Out of Africa"hypothesis, showing the possibility that humans could have crossed what is now the desert because water was available, if not plentiful, in every period, both glacial and interglacial. A study of kangaroo teeth was relevant to the settling of Australia. Recently she was concentrating on the presence of Neanderthals in Europe. Her interest there began with the finding of a bone flute at Divje Babe in Slovenia which she dated to at least 60 ka. Other areas included Uzbekistan, where she showed that only ESR could explain the stratigraphy of a site with Neanderthal remains, and Russian caves. At the time of her death, she was

Bonnie and Joel with one of their student groups at Williams

involved in a long-term study of Serbian and other Balkan caves, many of which have evidence of human habitation.

Bonnie's geological training led to studies such as tectonic uplift in Turkey, where she identified a previously unknown fault, and sea level changes. The latter proved useful in numerous dating studies of corals, where the dating range comprised several MIS stages.

Not all dating studies revolve around paleoanthropology, or areas with evidence of human habitation; some relate more to paleontology. Bonnie looked at multiple sites predating any hominin presence. For example, she studied the Miocene in China, and the Villefranchian in Europe. By identifying species present she also provided insights into paleoclimate and climate change.

Bonnie's contributions to the theoretical underpinning of ESR dating provide the fourth major category. While most ESR studies use mammal teeth or mollusc shells, she asked whether other materials were suitable. For some of these, such as shark and crocodile teeth, the answer was a decisive "no". Bone also provided more problems than solutions. Others were more promising, such as barnacles and stalagmites. Then she spent many hours investigating uranium uptake and leaching in teeth, factors that have a major impact on ESR dating. She promoted the use of isochrons for difficult sites and difficult samples. Another problem for ESR dating is 'lumpy' or complex sites; here she developed techniques for quantifying and including sometimes as many as nine different sedimentary factors into an environmental dose rate.

Most of her professional life was as a public high school science teacher in New York City. No account of her contributions would be complete without noting her work mentoring high school students. For over 20 years she sought out promising students and gave them serious, publishable, projects. Many were from low-income, minority and immigrant backgrounds. In 1999, with my assistance, she became a research associate with the Williams College Chemistry Department. She then set up the RFK Science Institute to formalize this structure. Her students gave presentations not just at science fairs, but at professional meetings. As well as science fair awards, several students won recognition from the Westinghouse (later Siemens-Westinghouse, and then Intel) contest. Roughly a dozen were state finalists or national semi-finalists, and one was a national finalist. As well as teaching all of the 100+ students the basics of first-class scientific research, Bonnie counselled them on college applications, encouraging them (often successfully) to 'reach'. For years afterwards she would keep in contact and be available for advice.

Bonnie was a Fellow of both the Geological Society of America and the Geological Society of Canada. Over the years she was principal investigator or co-PI on NSF grants totaling roughly $600,000. As well as her publications, she was sought after as a reviewer for professional journals.

Dr. Joel Blickstein, Bonnie's husband, was a partner and colleague in this work. When RFK students came to Williams, for example, Joel would help them run the ESR spectrometer, while Bonnie supervised calculations of results. Tragically, Joel died a week after Bonnie. Bonnie and Joel are survived by Joel's children, Jason and Tina, and their families.

Bonnie's energy and enthusiasm led to a significant body of work around issues of paleoanthropology, paleontology, and geology. It is clear that we have lost a voice that still had much to contribute to our understanding of the past.

Anne Skinner

Ancient TL

ISSN 2693-0935

Aims and Scope

Ancient TL is a journal devoted to Luminescence dating, Electron Spin Resonance (ESR) dating, and related techniques. It aims to publish papers dealing with experimental and theoretical results in this field, with a minimum of delay between submission and publication. Ancient TL also publishes a current bibliography, thesis abstracts, letters, and miscellaneous information, e.g., announcements for meetings.

Frequency

Two issues per annum in June and December

Submission of articles to Ancient TL

Ancient TL has a reviewing system in which direct dialogue is encouraged between reviewers and authors. For instructions to authors and information on how to submit to Ancient TL, please visit the website at:
http://ancienttl.org/TOC1.htm

Journal Enquiries

For enquiries please contact the editor:
Regina DeWitt, Department of Physics, East Carolina University, Howell Science Complex, 1000 E. 5th Street, Greenville, NC 27858, USA; Tel: +252-328-4980; Fax: +252-328-0753 (dewittr@ecu.edu)

Subscriptions to Ancient TL

Ancient TL Vol. 32 No.2 December 2014 was the last issue to be published in print. Past and current issues are available for download free of charge from the Ancient TL website:
http://ancienttl.org/TOC4.htm